

Air Force Institute of Technology

AFIT Scholar

Theses and Dissertations

Student Graduate Works

12-1995

Sub-Optimal Control of Rigid Spacecraft Reorientation Using Three Momentum Wheels

Gregory W. Schultz

Follow this and additional works at: <https://scholar.afit.edu/etd>



Part of the [Space Vehicles Commons](#)

Recommended Citation

Schultz, Gregory W., "Sub-Optimal Control of Rigid Spacecraft Reorientation Using Three Momentum Wheels" (1995). *Theses and Dissertations*. 6121.
<https://scholar.afit.edu/etd/6121>

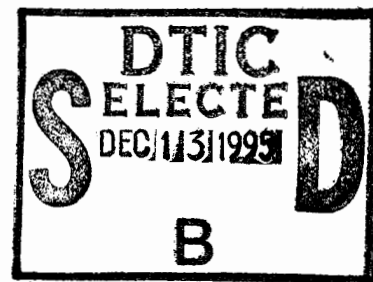
This Thesis is brought to you for free and open access by the Student Graduate Works at AFIT Scholar. It has been accepted for inclusion in Theses and Dissertations by an authorized administrator of AFIT Scholar. For more information, please contact AFIT.ENWL.Repository@us.af.mil.

AFIT/GA/ENY/95D-04

SUB-OPTIMAL CONTROL
OF
RIGID SPACECRAFT REORIENTATION
USING
THREE MOMENTUM WHEELS

THESIS
Gregory W. Schultz
Captain, USAF

AFIT/GA/ENY/95D-04



19951211 065

Approved for public release; distribution unlimited

DTIC QUALITY INSPECTED 1

The views expressed in this thesis are those of the author and do not reflect the official policy or position of the Department of Defense or the U. S. Government.

Accession For	
NTIS GRA&I	<input checked="" type="checkbox"/>
DTIC TAB	<input type="checkbox"/>
Unannounced	<input type="checkbox"/>
Justification	
By _____	
Distribution/	
Availability Codes	
Dist	Avail and/or Special
A-1	

AFIT/GA/ENY/95D-04

**SUB-OPTIMAL CONTROL
OF
RIGID SPACECRAFT REORIENTATION
USING
THREE MOMENTUM WHEELS**

THESIS

Presented to the Faculty of the Graduate School of Engineering
of the Air Force Institute of Technology
Air University
In Partial Fulfillment of the
Requirements for the Degree of
Master of Science in Astronautical Engineering

Gregory W. Schultz, B.S., M.B.A.
Captain, USAF

December, 1995

Approved for public release; distribution unlimited

Acknowledgements

First and foremost, I would like to thank my thesis advisor, Dr. Chris Hall, for his help, guidance, and patience during both my AFIT course work and my thesis research.

I would also like to thank my wife, Ruthe, for her support, understanding, and patience watching the kids over the past 18 months of short weekends and late nights, as well as for her encouragement to come to AFIT in the first place.

I also greatly appreciate the significant technical support from the Lockheed simulation engineers at Falcon AFB, CO (most notably Mr. Mark Kostelic), in locating and providing GPS Block IIR design and orbital parameters to improve the realism of my simulations.

Last, but certainly not least, I offer my sincerest regret to the forests of the world for the number of innocent trees that gave their lives to produce this document.

Gregory W. Schultz

Table of Contents

	Page
Acknowledgements	ii
List of Figures	vi
List of Tables	x
List of Symbols	xi
Abstract	xiii
I. Introduction	1-1
1.1 Background	1-1
1.2 Goals of This Thesis	1-3
1.3 Methodology	1-3
II. Equations of Motion	2-1
2.1 Rotational Equations of Motion	2-1
2.2 Non-dimensionalization	2-5
2.3 Perturbative Force Modeling	2-9
2.3.1 Gravity Gradient Torques	2-11
2.3.2 Solar Pressure Torques	2-13
2.4 Attitude Equations	2-19
2.5 Equations Summary	2-22
III. Wheel Torque Control Law Derivation	3-1
3.1 Stationary Platform Condition	3-1
3.2 Unachievable Regions on the Wheel Momenta Ellipsoid	3-9
3.3 Allowable Torque Magnitudes	3-14

	Page
3.4 Direct Rest-to-rest Trajectories	3-16
3.5 Sub-optimal Trajectories on the Wheel Momenta Ellipsoid	3-19
IV. Unperturbed Maneuvers	4-1
4.1 GPS Block IIR Examples	4-2
4.2 Hubble Space Telescope Examples	4-12
4.3 Summary of Results	4-27
V. Perturbed Stationary Platform Maneuvers	5-1
5.1 Example Using GPS Blk IIR	5-3
5.2 Example Using Hubble Space Telescope	5-6
5.3 Summary of Results	5-9
VI. Conclusions and Recommendations	6-1
6.1 Conclusions	6-1
6.2 Recommendations for Further Study	6-2
Appendix A. Constants and Unit Conversions	A-1
Appendix B. Global Positioning System (GPS) Block IIR Modeling Data	B-1
B.1 Mass and Inertia Properties Calculations	B-1
B.2 Material Properties	B-3
B.3 Momentum Wheel Assembly Properties Calculations	B-3
B.4 Orbital Parameters	B-4
Appendix C. Hubble Space Telescope Modeling Data	C-1
C.1 Mass and Inertia Properties Calculations	C-1
C.2 Material Properties	C-3
C.3 Momentum Wheel Assembly Properties Calculations	C-4
C.4 Orbital Parameters	C-5

	Page
Appendix D. MATLAB Code Listings	D-1
D.1 GPS Block IIR Data Definition File	D-2
D.2 Hubble Space Telescope Data Definition File	D-6
D.3 Main Simulation Program	D-11
D.4 Unperturbed Direct Control Law Equations	D-23
D.5 Unperturbed Sub-optimal Control Law Equations	D-24
D.6 Perturbed Sub-optimal Control Law Equations	D-25
D.7 Wheel Momenta Ellipsoid Plotting Function (point by point)	D-28
D.8 Wheel Momenta Ellipsoid Plotting Function (parameterized)	D-30
D.9 "1" Axis Rotation Matrix Function	D-32
D.10 "3" Axis Rotation Matrix Function	D-33
D.11 Quaternion to Rotation Matrix Conversion Function	D-33
D.12 Vector Cross Prodcut Function	D-34
D.13 Degrees to Radians Conversion Function	D-34
D.14 Radians to Degrees Conversion Function	D-34
D.15 3-D Line Plotting Function	D-34
 Bibliography	 BIB-1
 Vita	 VITA-1

List of Figures

Figure	Page
2.1. <i>Rigid Spacecraft with Multiple Momentum Wheels</i>	2-1
2.2. <i>GPS Block IIR Gravity Gradient Model</i>	2-13
2.3. <i>GPS Block IIR Idealization for Solar Pressure Modeling</i>	2-17
2.4. <i>Hubble Space Telescope Idealization for Solar Pressure Modeling</i>	2-18
3.1. <i>Spacecraft Total Momentum Sphere</i>	3-3
3.2. <i>Orthogonal Wheels</i>	3-4
3.3. <i>Wheel Momenta Ellipsoid (Orthogonal Wheels)</i>	3-4
3.4. <i>Pyramidal Wheels</i>	3-5
3.5. <i>Wheel Momenta Ellipsoid (Pyramidal Wheels)</i>	3-5
3.6. <i>Nearly Co-planar Wheels</i>	3-5
3.7. <i>Wheel Momentum Ellipsoid (Nearly Co-planar Wheels)</i>	3-5
3.8. <i>Nearly Co-linear Wheels</i>	3-6
3.9. <i>Wheel Momentum Ellipsoid (Nearly Co-linear Wheels)</i>	3-6
3.10. <i>Example 1 - Achievable Regions on Wheel Momenta Ellipsoid</i>	3-10
3.11. <i>Example 2 - Achievable Regions on Wheel Momenta Ellipsoid</i>	3-11
3.12. <i>Achievable Regions on Wheel Momenta Ellipsoid (Non-orthogonal Wheels)</i>	3-12
3.13. <i>Direct Trajectory on Wheel Momenta Ellipsoid</i>	3-16
3.14. <i>Direct Trajectory - Small Torque Parameter ϵ vs. \tilde{t}_f for varying \tilde{h}_o</i>	3-18
3.15. <i>Sub-optimal Trajectory on Wheel Momenta Ellipsoid</i>	3-21
3.16. <i>Sub-optimal Trajectory - Small Torque Parameter ϵ vs. \tilde{t}_f for varying \tilde{h}_o</i>	3-25
3.17. <i>Case 1 - Comparison of ϵ vs. \tilde{t}_f for Direct and Sub-optimal Trajectories</i>	3-26
3.18. <i>Case 2 - Comparison of ϵ vs. \tilde{t}_f for Direct and Sub-optimal Trajectories</i>	3-26
4.1. <i>GPS Example 1 - (Direct) Torque Trajectory on Wheel Momenta Ellipsoid</i>	4-5

Figure	Page
4.2. <i>GPS Example 1 - (Sub-opt) Torque Trajectory on Wheel Momenta Ellipsoid</i>	4-5
4.3. <i>GPS Example 1 - (Direct) Torque Trajectory on Total Momentum Sphere</i>	4-5
4.4. <i>GPS Example 1 - (Sub-opt) Torque Trajectory on Total Momentum Sphere</i>	4-5
4.5. <i>GPS Example 1 - (Direct) Wheel Angular Velocities</i>	4-6
4.6. <i>GPS Example 1 - (Sub-opt) Wheel Angular Velocities</i>	4-6
4.7. <i>GPS Example 1 - (Direct) Vehicle Angular Velocities</i>	4-6
4.8. <i>GPS Example 1 - (Sub-opt) Vehicle Angular Velocities</i>	4-6
4.9. <i>GPS Example 1 - Initial Attitude</i>	4-7
4.10. <i>GPS Example 1 - Desired Final Attitude</i>	4-7
4.11. <i>GPS Example 1 - (Direct) Final Attitude</i>	4-7
4.12. <i>GPS Example 1 - (Sub-opt) Final Attitude</i>	4-7
4.13. <i>GPS Example 2 - (Sub-opt) Torque Trajectory on Wheel Momenta Ellipsoid</i>	4-9
4.14. <i>GPS Example 2 - (Sub-opt) Torque Trajectory on Total Momentum Sphere</i>	4-9
4.15. <i>GPS Example 2 - (Sub-opt) Wheel Angular Velocities</i>	4-9
4.16. <i>GPS Example 2 - (Sub-opt) Vehicle Angular Velocities</i>	4-9
4.17. <i>GPS Example 3 - (Sub-opt) Torque Trajectory on Wheel Momenta Ellipsoid</i>	4-11
4.18. <i>GPS Example 3 - (Sub-opt) Torque Trajectory on Total Momentum Sphere</i>	4-11
4.19. <i>GPS Example 3 - (Sub-opt) Wheel Angular Velocities</i>	4-11
4.20. <i>GPS Example 3 - (Sub-opt) Vehicle Angular Velocities</i>	4-11
4.21. <i>Hubble Example 1 - (Sub-opt) Torque Trajectory on Wheel Momenta Ellipsoid</i>	4-15
4.22. <i>Hubble Example 1 - (Sub-opt) Torque Trajectory on Total Momentum Sphere</i>	4-15
4.23. <i>Hubble Example 1 - (Sub-opt) Wheel Angular Velocities</i>	4-15
4.24. <i>Hubble Example 1 - (Sub-opt) Vehicle Angular Velocities</i>	4-15

Figure	Page
4.25. <i>Hubble Example 1 - Desired Final Attitude</i>	4-16
4.26. <i>Hubble Example 1 - (Sub-opt) Final Attitude</i>	4-16
4.27. <i>Hubble Example 2 - (Sub-opt) Torque Trajectory on Wheel Momenta Ellipsoid</i>	4-18
4.28. <i>Hubble Example 2 - (Sub-opt) Torque Trajectory on Total Momentum Sphere</i>	4-18
4.29. <i>Hubble Example 2 - (Sub-opt) Wheel Angular Velocities</i>	4-18
4.30. <i>Hubble Example 2 - (Sub-opt) Vehicle Angular Velocities</i>	4-18
4.31. <i>Hubble Example 2 - Desired Final Attitude</i>	4-19
4.32. <i>Hubble Example 2 - (Sub-opt) Final Attitude</i>	4-19
4.33. <i>Hubble Example 3 - (Sub-opt) Torque Trajectory on Wheel Momenta Ellipsoid</i>	4-21
4.34. <i>Hubble Example 3 - (Direct) Torque Trajectory on Wheel Momenta Ellipsoid</i>	4-21
4.35. <i>Hubble Example 3 - (Sub-opt) Torque Trajectory on Total Momentum Sphere</i>	4-21
4.36. <i>Hubble Example 3 - (Direct) Torque Trajectory on Total Momentum Sphere</i>	4-21
4.37. <i>Hubble Example 3 - (Sub-opt) Wheel Angular Velocities</i>	4-22
4.38. <i>Hubble Example 3 - (Direct) Wheel Angular Velocities</i>	4-22
4.39. <i>Hubble Example 3 - (Sub-opt) Vehicle Angular Velocities</i>	4-22
4.40. <i>Hubble Example 3 - (Direct) Vehicle Angular Velocities</i>	4-22
4.41. <i>Hubble Example 3 - Initial Attitude</i>	4-23
4.42. <i>Hubble Example 3 - Desired Final Attitude</i>	4-23
4.43. <i>Hubble Example 3 - (Sub-opt) Final Attitude</i>	4-23
4.44. <i>Hubble Example 3 - (Direct) Final Attitude</i>	4-23
4.45. <i>Hubble Example 4 - (Sub-opt) Torque Trajectory on Wheel Momenta Ellipsoid</i>	4-25
4.46. <i>Hubble Example 4 - (Sub-opt) Torque Trajectory on Total Momentum Sphere</i>	4-25

Figure	Page
4.47. <i>Hubble Example 4 - (Sub-opt) Wheel Angular Velocities</i>	4-25
4.48. <i>Hubble Example 4 - (Sub-opt) Vehicle Angular Velocities</i>	4-25
4.49. <i>Hubble Example 4 - (Sub-opt) Desired Final Attitude</i>	4-26
4.50. <i>Hubble Example 4 - (Sub-opt) Final Attitude</i>	4-26
5.1. <i>GPS Example 4 - (Sub-opt) Perturbed Torque Trajectory on Total Mo- mentum Sphere</i>	5-4
5.2. <i>GPS Example 4 - (Sub-opt) Perturbed Total Angular Momentum Magni- tude</i>	5-4
5.3. <i>GPS Example 4 - (Sub-opt) Perturbed Wheel Angular Velocities</i>	5-4
5.4. <i>GPS Example 4 - (Sub-opt) Perturbed Vehicle Angular Velocities</i>	5-4
5.5. <i>GPS Example 4 - Desired Final Attitude</i>	5-5
5.6. <i>GPS Example 4 - (Sub-opt) Perturbed Final Attitude</i>	5-5
5.7. <i>Hubble Example 5 - (Sub-opt) Perturbed Torque Trajectory on Total Mo- mentum Sphere</i>	5-7
5.8. <i>Hubble Example 5 - (Sub-opt) Perturbed Total Angular Momentum Mag- nitude</i>	5-7
5.9. <i>Hubble Example 5 - (Sub-opt) Perturbed Wheel Angular Velocities</i>	5-7
5.10. <i>Hubble Example 5 - (Sub-opt) Perturbed Vehicle Angular Velocities</i>	5-7
5.11. <i>Hubble Example 5 - Desired Final Attitude</i>	5-8
5.12. <i>GPS Example 5 - (Sub-opt) Perturbed Final Attitude</i>	5-8
B.1. <i>GPS Block IIR Estimated Dimensions (Front and Side)</i>	B-2
B.2. <i>GPS Block IIR Wheel Orientations</i>	B-3
C.1. <i>Hubble Space Telescope Estimated Dimensions</i>	C-2
C.2. <i>Hubble Space Telescope Assumed Wheel Orientations</i>	C-4
D.1. <i>Simulation Program Functional Flow Diagram</i>	D-1

List of Tables

Table	Page
4.1. GPS Example 1 - Direct vs. Sub-optimal Simulation Parameters . . .	4-4
4.2. GPS Example 1 - Direct vs. Sub-optimal Simulation Results	4-4
4.3. GPS Example 2 - Sub-optimal Simulation Parameters	4-8
4.4. GPS Example 2 - Sub-optimal Simulation Results	4-8
4.5. GPS Example 3 - Sub-optimal Simulation Parameters	4-10
4.6. GPS Example 3 - Sub-optimal Simulation Results	4-10
4.7. Hubble Example 1 - Sub-optimal Simulation Parameters	4-14
4.8. Hubble Example 1 - Sub-optimal Simulation Results	4-14
4.9. Hubble Example 2 - Sub-optimal Simulation Parameters	4-17
4.10. Hubble Example 2 - Sub-optimal Simulation Results	4-17
4.11. Hubble example 3 - Direct vs. Sub-optimal Simulation Parameters . .	4-20
4.12. Hubble example 3 - Direct vs. Sub-optimal Simulation Results	4-20
4.13. Hubble Example 4 - Sub-optimal Simulation Parameters	4-24
4.14. Hubble Example 4 - Sub-optimal Simulation Results	4-24
5.1. GPS example 4 - Perturbed Sub-optimal Simulation Parameters	5-3
5.2. GPS example 4 - Perturbed Sub-optimal Simulation Results	5-3
5.3. Hubble Example 5 - Perturbed Sub-optimal Simulation Parameters . .	5-6
5.4. Hubble Example 5 - Perturbed Sub-optimal Simulation Results	5-6

List of Symbols

The following is a list of the most important and frequently used symbols in this document. It is by no means complete but should aid the reader in better understanding the text.

\mathcal{F}_i	=	inertially fixed reference frame (origin at Earth center)
$\hat{\mathbf{e}}_1, \hat{\mathbf{e}}_2, \hat{\mathbf{e}}_3$	=	orthonormal basis for \mathcal{F}_i
\mathcal{F}_b	=	spacecraft body fixed reference frame (origin at center of mass)
$\hat{\mathbf{b}}_1, \hat{\mathbf{b}}_2, \hat{\mathbf{b}}_3$	=	orthonormal basis for \mathcal{F}_b
\mathcal{F}_μ	=	reference frame in wheel relative momenta 'μ space'
$\hat{\boldsymbol{\mu}}_1, \hat{\boldsymbol{\mu}}_2, \hat{\boldsymbol{\mu}}_3$	=	orthonormal basis for \mathcal{F}_μ
\mathcal{R}	=	spacecraft rigid platform
\mathcal{W}_j	=	individual momentum wheel j
$\hat{\mathbf{a}}_j$	=	axis of relative rotation of \mathcal{W}_j , fixed in \mathcal{F}_b
\mathbf{x}	=	3×1 matrix of total spacecraft angular momentum
$\boldsymbol{\mu}$	=	$n \times 1$ matrix of wheel relative momenta in \mathcal{F}_μ
$\boldsymbol{\omega}$	=	3×1 matrix of angular velocity components of \mathcal{F}_b relative to \mathcal{F}_i
$\tilde{\boldsymbol{\omega}}_s$	=	$n \times 1$ matrix of wheel angular velocities relative to \mathcal{F}_b
$\tilde{\mathbf{I}}$	=	Inertia matrix for spacecraft, about center of mass
$\tilde{\mathbf{I}}_s$	=	diagonal $n \times n$ matrix of axial moments of inertia of wheels
\mathcal{I}	=	the identity matrix
$\boldsymbol{\epsilon}$	=	3×1 matrix of axial torques applied by \mathcal{R} to \mathcal{W}_n about $\hat{\mathbf{a}}_n$
ϵ	=	a small scalar torque parameter
$\tilde{\mathbf{M}}_s$	=	3×1 matrix of solar pressure induced moments on spacecraft
$\tilde{\mathbf{M}}_g$	=	3×1 matrix of gravity gradient induced moments on spacecraft
\mathbf{M}	=	3×1 matrix of total external moment acting on spacecraft
$\hat{\mathbf{S}}$	=	unit Sun vector
$\tilde{\mathbf{R}}$	=	vector from Earth center to spacecraft center of mass
$\tilde{\mathbf{V}}$	=	velocity vector of spacecraft center of mass
$\tilde{\mathbf{r}}_j$	=	vector from spacecraft center of mass to component j center
$\hat{\mathbf{n}}_j$	=	unit normal vector from center of pressure of component i
\mathbf{q}	=	4×1 matrix of quaternion parameters

General note 1:

Vectors and dyadics, which are independent of reference frame, are denoted by a bold character and an arrow (e.g. $\vec{\mathbf{h}}$ and $\vec{\mathbf{I}}$). Unit vectors are similarly denoted by bold characters and hats (e.g. $\hat{\mathbf{b}}_1$). Matrices representing vectors and dyadics in a particular reference frame are denoted by the *same* bold character without the arrow or hat. The particular associated reference frame will be stated in the accompanying text or implied.

General note 2:

A tilde superscript on a vector or a matrix representing a vector (eg. $\tilde{\mathbf{M}}$) indicates that it is the dimensional form. Accordingly, vectors and matrices representing vectors *without* tilde superscripts can be assumed to be non-dimensionalized unless specifically indicated.

Abstract

Attitude maneuvering of three axis stabilized spacecraft is typically accomplished using a combination of expendable propellant thrusters, magnetic coils, momentum storage mechanisms such as momentum wheels, reaction wheels, or control moment gyros, or passive methods such as gravity gradient stabilization.

With a few exceptions (most notably the Hubble Space Telescope), most three axis stabilized spacecraft in service today still rely heavily upon expendable propellant thrusters for primary attitude control, using momentum storage devices only to offset small perturbative torques.

While thrusters allow rapid changes in attitude, their reliance on limited propellant supplies can result in shortened useful lifetimes for spacecraft employing them exclusively. Passive attitude control methods such as gravity gradient stabilization or utilization of solar pressure on solar arrays tend to be slow and are dependent upon interaction with uncontrollable forces. Maneuvering using magnetic coils is likewise somewhat slow and becomes less effective with altitude.

Momentum transfer devices, on the other hand, rely upon a reusable energy source - electrical power - provided by solar arrays and rechargeable batteries, and can be used to effect large angle reorientations relatively quickly. However, due to the inherent gyroscopic coupling for a rigid body with embedded momentum wheels and limited control authority in terms of allowable torques on the wheels and maximum allowable wheel speeds, implementation of "optimal" control laws for these devices can be somewhat complicated. Calculation of wheel torques for large angle maneuvers based on eigen-axis rotations or other currently used control laws are beyond the on-board processing capability of most current satellites. This results in the vehicles being dependent on the ground segment computers and ground commanding for such maneuvers.

This thesis addresses sub-optimal employment of 3 momentum wheels for large angle reorientation of rigid spacecraft with minimal induced spacecraft motion during maneuvers.

In addition to development of general theory for 3 wheel vehicles, simulation results for a vehicle using momentum wheels for secondary attitude control (GPS Block IIR) are compared to results for a vehicle using them for primary attitude control (the Hubble Space Telescope), to demonstrate practical applications and limitations.

While the control laws were developed assuming no external perturbing torques on the vehicle, reorientation scenarios were run both in a torque free environment as well as an environment with simulated gravity gradient and solar pressure torques. The goal was primarily to show the growth of vehicle angular velocities and again demonstrate limitations of the derived control laws.

The results indicate that for real spacecraft with limited wheel momentum storage capacities, there is a significant trade-off between maneuver times and required wheel torques, and that final state errors (angular velocities) increase with increasing wheel torques. Nonetheless, the simulations demonstrated that large angle maneuvers *can* be performed for both GPS Block IIR and Hubble Space Telescope in reasonable times and with small angular velocities using the sub-optimal control law. However, gravity gradient and solar pressure torques tended to cause larger fluctuations in total angular momentum, angular velocities, and final state errors for the Hubble Space Telescope.

Hopefully the results of this report can be used as a basis for future analysis of this or similar sub-optimal control approaches. Recommendations for follow-on research include comparison of this approach to optimal control formulations, as well as consideration of vehicle kinematics in the control law formulation to reduce final attitude errors. This can, in turn, be used in the development of closed loop controllers that will minimize deviations from the sub-optimal control trajectories in the presence of external perturbations.

**SUB-OPTIMAL CONTROL
OF
RIGID SPACECRAFT REORIENTATION
USING
THREE MOMENTUM WHEELS**

I. Introduction

1.1 Background

Spacecraft attitude dynamics, stability, and control has obviously been an area of avid research since the launch of the first artificial satellites in the late 1950's. Although early satellites had no need for accurate attitude control, the rapid advancement in space-based communications and remote sensing applications has resulted in the need for robust and efficient attitude control systems in modern spacecraft.

Most communications and remote sensing spacecraft in operation and in development today employ three-axis stabilization due to mission mandated pointing accuracy requirements and the associated need to minimize vibrations in large flexible appendages. With a few notable exceptions (e.g. Hubble Space Telescope), three-axis stabilization schemes typically utilize momentum storage devices such as reaction wheels, momentum wheels, or control moment gyros only to offset the long term effects of small external perturbing forces, and accomplish large angle reorientations using expendable propellant thrusters. While certainly efficient in terms of controllability and time required to complete maneuvers, the use of thrusters limits the effective life of satellites, results in high maneuver costs, can induce undesirable motion in spacecraft appendages, and can in some cases adversely affect the operation of sensitive on-board systems (like optical telescopes in the case of Hubble). It is thus in general cost effective and in some cases mission critical to use momentum storage devices not only for fine attitude control but also for primary attitude maneuvering whenever practical.

Many of the analytic solutions to spacecraft attitude control problems to date have focused on the relatively simple case of the *gyrostat*, which is typically used to refer to “dual-spin” spacecraft composed of an inertially fixed segment (platform) and a spinning segment (rotor) which provides gyroscopic stiffness. Several textbooks (most notably Hughes [11]) journal papers (including Hall [8],[9], Hall and Rand [10]), and AFIT theses (Kinney [14], Kowall [15], and Tsui [22]) have addressed exact or approximate analytic solutions and related stability for both single and two rotor gyrostats. Many researchers have also addressed developing control laws for multiple momentum wheels from an optimal control perspective (a significant contribution is provided by Junkins and Turner [12]). Unfortunately, the resulting calculations can be computationally intense, and thus relegated to ground segment computers for practical application. This increases satellite dependence on the ground segment, limits their autonomy (and thus survivability and flexibility), and increases operations costs for these vehicles.

However, Hall [8] did provide the framework for development of a class of sub-optimal maneuvers based on his analysis of single and two rotor gyrostats. This *stationary platform* maneuver is a rest-to-rest maneuver (inertially fixed at beginning and end) during which angular velocities of the platform are kept small throughout the maneuver. This has the advantage of limiting induced vibrations in flexible appendages, and is also easily calculable. Thus, such a control law could easily be incorporated into the attitude control logic of future spacecraft and calculated on-board, thereby increasing autonomy of these vehicles as well as the mission life by using momentum wheels for large angle maneuvers instead of thrusters.

1.2 Goals of This Thesis

The primary objectives of this report are three-fold: To extend Hall's research by developing a "simple" sub-optimal control law for spacecraft using three momentum wheels, to assess the utility and limitations of this control law for "real" spacecraft in a torque free environment, and finally to qualitatively address the additional limitations of the control law imposed by the addition of external perturbing torques such as gravity gradient and solar pressure.

This work will thus hopefully serve as a foundation for future research using this or similar control approaches by identifying the strengths and weaknesses as currently implemented and providing specific recommendations for improvement.

1.3 Methodology

A computer simulation program was developed by the author for use in this research effort. The code is included in Appendix D. This program calculates the physical properties for the GPS Block IIR and Hubble Space Telescope vehicles, sets initial orbital and simulation parameters, numerically integrates the equations of motion for the vehicle (perturbed or unperturbed), and provides both textual and graphical output of the results. Data from the simulation runs are the main subject of analysis in this report.

Chapter 2 of this report focuses on the derivation of the equations of motion of an Earth orbiting rigid spacecraft with fixed momentum wheels, in the presence of gravity gradient and solar pressure torques. It is these equations which are integrated by the aforementioned simulation program. While mainly a compilation of results from previous research, the chapter provides a coherent and logical summary of the pertinent equations, thereby reducing the need for the reader to refer to outside sources.

In Chapter 3, Hall's development of sub-optimal control laws for a spacecraft using two momentum wheels is extended to a spacecraft using 3 (or more) wheels, resulting in a wheel torque control law that results in "smooth" large angle reorientations from one inertially fixed state to another with only small induced body angular velocities.

Chapter 4 compares this sub-optimal control law to constant wheel torque maneuvers for actual vehicles (GPS Block IIR and Hubble Space Telescope). Limitations of the sub-optimal control are explored with several computer simulations varying the magnitudes of the control torques used.

Chapter 5 then introduces gravity gradient and solar pressure torques, and the resulting deviations from the torque free case are discussed by comparing computer simulations for both unperturbed and perturbed models.

The overall results are presented and discussed in Chapter 6, along with recommendations for further research.

II. Equations of Motion

In this chapter we derive the rotational and attitude equations of motion for a rigid spacecraft \mathcal{R} with n embedded axisymmetric momentum wheels \mathcal{W}_n operating in an environment with external perturbing torques (solar pressure and gravity gradient). Both dimensional and non-dimensional forms of the equations are developed. The notation used is primarily that of Hughes [11] and Hall [8].

2.1 Rotational Equations of Motion

Figure 2.1 depicts a spacecraft composed of a platform \mathcal{R} and momentum wheels $\mathcal{W}_1 \dots \mathcal{W}_n$.

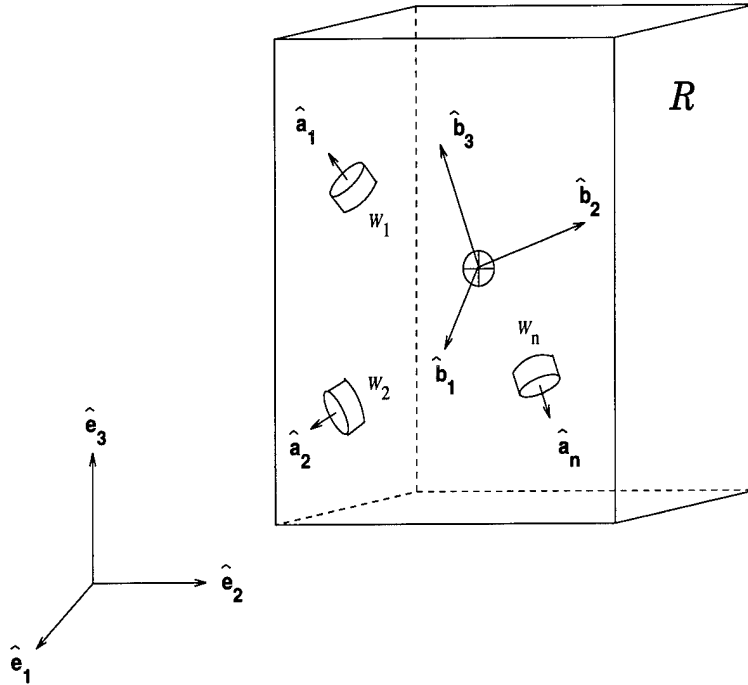


Figure 2.1 *Rigid Spacecraft with Multiple Momentum Wheels*

The platform is rigid, has constant mass, is not necessarily symmetric, and the body fixed reference frame \mathcal{F}_b with basis $(\hat{\mathbf{b}}_1 \hat{\mathbf{b}}_2 \hat{\mathbf{b}}_3)$ is centroidal but not necessarily principal. The body fixed frame translates and rotates relative to the inertially fixed reference frame \mathcal{F}_i with basis $(\hat{\mathbf{e}}_1 \hat{\mathbf{e}}_2 \hat{\mathbf{e}}_3)$. The spin axes of the momentum wheels are assumed to be fixed within the spacecraft. The wheels are assumed to be perfectly balanced

and axisymmetric, spinning about their individual axes of symmetry $\hat{\mathbf{a}}_1 \dots \hat{\mathbf{a}}_n$. Before proceeding with derivation of the equations of motion, a few definitions are necessary.

We define the matrix \mathbf{A} such that the columns are the column matrices \mathbf{a}_j ($j = 1 \dots n$) specifying the orientation of the wheels $\mathcal{W}_1 \dots \mathcal{W}_n$ within the vehicle in \mathcal{F}_b .

$$\mathbf{A} = \begin{pmatrix} \vdots & \vdots & \cdots & \vdots \\ \mathbf{a}_1 & \mathbf{a}_2 & \cdots & \mathbf{a}_n \\ \vdots & \vdots & \cdots & \vdots \end{pmatrix} \quad (2.1)$$

The moments of inertia matrix for the entire spacecraft (including wheels) is assumed constant as a result of the constant mass and rigidity assumptions.

$$\tilde{\mathbf{I}} = \begin{pmatrix} \tilde{I}_{11} & \tilde{I}_{12} & \tilde{I}_{13} \\ \tilde{I}_{21} & \tilde{I}_{22} & \tilde{I}_{23} \\ \tilde{I}_{31} & \tilde{I}_{32} & \tilde{I}_{33} \end{pmatrix} \quad (2.2)$$

Finally, $\tilde{\mathbf{I}}_s$ is a diagonal matrix composed of the axial moments of inertia of the wheels $\mathcal{W}_1 \dots \mathcal{W}_n$.

$$\tilde{\mathbf{I}}_s = \begin{pmatrix} \tilde{I}_{s1} & 0 & \cdots & \cdots & 0 \\ 0 & \tilde{I}_{s2} & 0 & \cdots & 0 \\ \vdots & 0 & \ddots & & \vdots \\ \vdots & \vdots & & \ddots & \vdots \\ 0 & 0 & 0 & \cdots & \tilde{I}_{sn} \end{pmatrix} \quad (2.3)$$

We will now derive the equations of motion for a rigid spacecraft with embedded momentum wheels for the general case in an environment with external perturbing torques.

Following Hughes [11:159], the total angular momentum of a rigid platform with embedded momentum wheels can be expressed in the form

$$\tilde{\mathbf{h}} = \tilde{\mathbf{I}}\tilde{\boldsymbol{\omega}} + \mathbf{A}\tilde{\mathbf{h}}_s \quad (2.4)$$

where the axial angular momenta of the wheels about their spin axes in \mathcal{F}_b are

$$\tilde{\mathbf{h}}_s = \tilde{\mathbf{I}}_s \tilde{\omega}_s \quad (2.5)$$

The absolute time derivative of angular momentum (in \mathcal{F}_i) can be written as the relative time derivative of angular momentum (in \mathcal{F}_b) plus the cross product of the angular rates of \mathcal{F}_b relative to \mathcal{F}_i and the angular momentum

$$\left[\dot{\tilde{\mathbf{h}}} \right]_{\mathcal{F}_i} = \left[\dot{\tilde{\mathbf{h}}} \right]_{\mathcal{F}_b} + \tilde{\omega}^\times \tilde{\mathbf{h}}$$

where

$$\tilde{\omega}^\times = \begin{pmatrix} 0 & -\tilde{\omega}_3 & \tilde{\omega}_2 \\ \tilde{\omega}_3 & 0 & -\tilde{\omega}_1 \\ -\tilde{\omega}_2 & \tilde{\omega}_1 & 0 \end{pmatrix} \quad (2.6)$$

In an environment *free of external torques*, the absolute time derivative of angular momentum (in \mathcal{F}_i) is zero ($\left[\dot{\tilde{\mathbf{h}}} \right]_{\mathcal{F}_i} = 0$), so that this equation may be rearranged and written as

$$\left[\dot{\tilde{\mathbf{h}}} \right]_{\mathcal{F}_b} = -\tilde{\omega}^\times \tilde{\mathbf{h}} = \tilde{\mathbf{h}}^\times \tilde{\omega} \quad (2.7)$$

On the other hand, if external perturbing torques are present, the absolute time derivative of angular momentum (in \mathcal{F}_i) is equal to the sum of the external torques ($\left[\dot{\tilde{\mathbf{h}}} \right]_{\mathcal{F}_i} = \tilde{\mathbf{M}}$), so that the equivalent and more general equation, after some rearranging, is

$$\left[\dot{\tilde{\mathbf{h}}} \right]_{\mathcal{F}_b} = \tilde{\mathbf{M}} - \tilde{\omega}^\times \tilde{\mathbf{h}} = \tilde{\mathbf{M}} + \tilde{\mathbf{h}}^\times \tilde{\omega} \quad (2.8)$$

Hughes [11] also shows that the total angular momenta of the wheels is given by

$$\tilde{\mathbf{h}}_a = \tilde{\mathbf{I}}_s \mathbf{A}^T \tilde{\omega} + \tilde{\mathbf{h}}_s \quad (2.9)$$

so that the time derivative of the total angular momenta of the wheels can be expressed as

$$\dot{\tilde{\mathbf{h}}}_a = \frac{d\tilde{\mathbf{h}}_a}{dt} = \tilde{\mathbf{g}}_a \quad (2.10)$$

where $\tilde{\mathbf{g}}_a$ are the torques applied by the platform to the wheels about their spin axes.

Now, dropping the reference frame notation (thereby assuming all future equations are expressed in \mathcal{F}_b), the rotational equations of motion for a spacecraft composed of a rigid platform \mathcal{R} and n embedded rigid momentum wheels \mathcal{W}_j ($j = 1 \dots n$) can be summarized as

$$\dot{\tilde{\mathbf{h}}} = \frac{d\tilde{\mathbf{h}}}{d\tilde{t}} = \tilde{\mathbf{h}}^\times \tilde{\boldsymbol{\omega}} + \tilde{\mathbf{M}} \quad (2.11)$$

$$\dot{\tilde{\mathbf{h}}}_a = \frac{d\tilde{\mathbf{h}}_a}{d\tilde{t}} = \tilde{\mathbf{g}}_a \quad (2.12)$$

where

$$\tilde{\mathbf{h}} = \tilde{\mathbf{I}}\tilde{\boldsymbol{\omega}} + \mathbf{A}\tilde{\mathbf{h}}_s = \text{total angular momentum of } \mathcal{R} + \mathcal{W}_j \quad (2.13)$$

$$\tilde{\mathbf{h}}_a = \tilde{\mathbf{I}}_s \mathbf{A}^T \tilde{\boldsymbol{\omega}} + \tilde{\mathbf{h}}_s = \text{total angular momenta of } \mathcal{W}_j \quad (2.14)$$

$$\tilde{\mathbf{h}}_s = \tilde{\mathbf{I}}_s \tilde{\boldsymbol{\omega}}_s = \text{axial angular momenta of } \mathcal{W}_j \text{ about } \hat{\mathbf{a}}_j \quad (2.15)$$

$$\tilde{\mathbf{M}} = \text{external torques acting on the vehicle} \quad (2.16)$$

$$\tilde{\mathbf{g}}_a = \text{axial torques applied by } \mathcal{R} \text{ to } \mathcal{W}_j \text{ about } \hat{\mathbf{a}}_j$$

$$\tilde{t} = \text{time} \quad (2.17)$$

$$j = 1 \dots n$$

2.2 Non-dimensionalization

In order to more easily derive the stationary platform condition and visualize torque trajectories that satisfy this condition, it will be useful to non-dimensionalize the rotational and wheel torque differential equations (2.11) and (2.12). This has the added advantage of generalizing the solution to a variety of applications. The following sequence of steps is basically an expansion of the non-dimensionalization developed by Hall [8], with the addition of external torques.

Solving Eq. (2.14) for $\tilde{\mathbf{h}}_s$ and substituting into Eq. (2.13) yields

$$\tilde{\mathbf{h}}_s = \tilde{\mathbf{h}}_a - \tilde{\mathbf{I}}_s \mathbf{A}^T \tilde{\omega} \quad (2.18)$$

$$\tilde{\mathbf{h}} = \tilde{\mathbf{I}} \tilde{\omega} + \mathbf{A} (\tilde{\mathbf{h}}_a - \tilde{\mathbf{I}}_s \mathbf{A}^T \tilde{\omega}) = (\tilde{\mathbf{I}} - \mathbf{A} \tilde{\mathbf{I}}_s \mathbf{A}^T) \tilde{\omega} + \mathbf{A} \tilde{\mathbf{h}}_a \quad (2.19)$$

Now define

$$\tilde{\mathbf{J}} = \tilde{\mathbf{I}} - \mathbf{A} \tilde{\mathbf{I}}_s \mathbf{A}^T \quad (2.20)$$

so that Eq. (2.19) becomes

$$\tilde{\mathbf{h}} = \tilde{\mathbf{J}} \tilde{\omega} + \mathbf{A} \tilde{\mathbf{h}}_a \quad (2.21)$$

Solving for $\tilde{\omega}$ results in

$$\tilde{\omega} = \tilde{\mathbf{J}}^{-1} (\tilde{\mathbf{h}} - \mathbf{A} \tilde{\mathbf{h}}_a) \quad (2.22)$$

Substituting $\tilde{\omega}$ into Eq. (2.11) yields

$$\dot{\tilde{\mathbf{h}}} = \tilde{\mathbf{h}}^\times [\tilde{\mathbf{J}}^{-1} (\tilde{\mathbf{h}} - \mathbf{A} \tilde{\mathbf{h}}_a)] + \tilde{\mathbf{M}}$$

Now, we introduce the following transformations to non-dimensionalize:

$$\mathbf{x} = \frac{\tilde{\mathbf{h}}}{\tilde{h}_o} \quad (2.23)$$

$$\boldsymbol{\mu} = \frac{\tilde{\mathbf{h}}_a}{\tilde{h}_o} \quad (2.24)$$

$$\mathbf{M} = \frac{\tilde{\mathbf{M}} \tilde{I}_c}{\tilde{h}_o^2} \quad (2.25)$$

$$\epsilon = \frac{\tilde{\mathbf{g}}_a \tilde{I}_c}{\tilde{h}_o^2} \quad (2.26)$$

$$t = \frac{\tilde{t} \tilde{h}_o}{\tilde{I}_c} \quad (2.27)$$

where $\tilde{I}_c = \text{trace}(\tilde{\mathbf{I}})$ is a characteristic inertia and \tilde{h}_o is the magnitude of the total angular momentum. Note that for the external torque-free case, $\tilde{h} = \text{constant}$, so the magnitude at any time can be used. However, in the case with external torques present, the magnitude of total angular momentum can vary. Thus, it is best to select a known value such as the initial total angular momentum, \tilde{h}_o , which is valid in both cases.

Since all moments of inertia (including $\tilde{\mathbf{J}}$) are non-dimensionalized by dividing by \tilde{I}_c , we can replace $\tilde{\mathbf{J}}$ with $\mathbf{J}\tilde{I}_c$ in Eq. (2.21) to obtain

$$\tilde{\mathbf{h}} = \mathbf{J}\tilde{I}_c\tilde{\omega} + \mathbf{A}\tilde{\mathbf{h}}_a \quad (2.28)$$

Dividing both sides of this equation by \tilde{h}_o and noting the relationships given in Eq. (2.23) and Eq. (2.24), this becomes

$$\mathbf{x} = \frac{\mathbf{J}\tilde{I}_c}{\tilde{h}_o}\tilde{\omega} + \mathbf{A}\boldsymbol{\mu} \quad (2.29)$$

Solving this equation for $\tilde{\omega}$ yields

$$\tilde{\omega} = \frac{\tilde{h}_o}{\tilde{I}_c}\mathbf{J}^{-1}(\mathbf{x} - \mathbf{A}\boldsymbol{\mu}) \quad (2.30)$$

This is essentially another derived non-dimensionalization transformation relating $\tilde{\omega}$ and ω where

$$\omega = \mathbf{J}^{-1}(\mathbf{x} - \mathbf{A}\boldsymbol{\mu}) \quad (2.31)$$

We can thus substitute Eq. (2.30) into Eq. (2.11) to obtain

$$\frac{d\tilde{\mathbf{h}}}{d\tilde{t}} = \tilde{\mathbf{h}} \times \left[\left(\frac{\tilde{h}_o}{\tilde{I}_c} \right) \mathbf{J}^{-1}(\mathbf{x} - \mathbf{A}\boldsymbol{\mu}) \right] + \tilde{\mathbf{M}} \quad (2.32)$$

From the non-dimensionalization transformation for \tilde{t} in Eq. (2.27) we obtain

$$d\tilde{t} = dt \left(\frac{\tilde{I}_c}{\tilde{h}_o} \right) \quad (2.33)$$

Substituting this into Eq. (2.32) yields

$$\frac{d\tilde{\mathbf{h}}}{dt} \left(\frac{\tilde{h}_o}{\tilde{I}_c} \right) = \tilde{\mathbf{h}}^\times \left[\left(\frac{\tilde{h}_o}{\tilde{I}_c} \right) \mathbf{J}^{-1} (\mathbf{x} - \mathbf{A}\boldsymbol{\mu}) \right] + \tilde{\mathbf{M}} \quad (2.34)$$

Multiplying through by $(\tilde{I}_c/\tilde{h}_o^2)$, and regrouping slightly results in

$$\frac{1}{\tilde{h}_o} \frac{d\tilde{\mathbf{h}}}{dt} = \left(\frac{\tilde{\mathbf{h}}}{\tilde{h}_o} \right)^\times \mathbf{J}^{-1} (\mathbf{x} - \mathbf{A}\boldsymbol{\mu}) + \frac{\tilde{\mathbf{M}}\tilde{I}_c}{\tilde{h}_o^2} \quad (2.35)$$

Recognizing from Eqs. (2.23) and (2.25) that $\tilde{\mathbf{h}}/\tilde{h}_o = \mathbf{x}$, $d\tilde{\mathbf{h}}/\tilde{h}_o = d\mathbf{x}$, and $\tilde{\mathbf{M}}\tilde{I}_c/\tilde{h}_o^2 = \mathbf{M}$, this equation reduces to

$$\frac{d\mathbf{x}}{dt} = \mathbf{x}^\times [\mathbf{J}^{-1} (\mathbf{x} - \mathbf{A}\boldsymbol{\mu})] + \mathbf{M} \quad (2.36)$$

which results in the dimensionless rotational equations of motion

$$\dot{\mathbf{x}} = \mathbf{x}^\times [\mathbf{J}^{-1} (\mathbf{x} - \mathbf{A}\boldsymbol{\mu})] + \mathbf{M} \quad (2.37)$$

or, noting from Eq. (2.31) that $\boldsymbol{\omega} = \mathbf{J}^{-1} (\mathbf{x} - \mathbf{A}\boldsymbol{\mu})$:

$$\dot{\mathbf{x}} = \mathbf{x}^\times \boldsymbol{\omega} + \mathbf{M} \quad (2.38)$$

Similarly, by making the substitution from Eq. (2.33) for $d\tilde{t}$ in the dimensional wheel torque relationship, Eq. (2.12) becomes

$$\frac{d\tilde{\mathbf{h}}_a}{dt} \left(\frac{\tilde{h}_o}{\tilde{I}_c} \right) = \tilde{\mathbf{g}}_a \quad (2.39)$$

Dividing both sides by \tilde{h}_o and recognizing from Eq. (2.24) that $d\tilde{\mathbf{h}}_a/\tilde{h}_o = d\boldsymbol{\mu}$ results in

$$\frac{d\boldsymbol{\mu}}{dt} \left(\frac{\tilde{h}_o}{\tilde{I}_c} \right) = \frac{\tilde{\mathbf{g}}_a}{\tilde{h}_o} \quad (2.40)$$

which can be rewritten as

$$\dot{\boldsymbol{\mu}} = \left(\frac{\tilde{I}_c}{\tilde{h}_o^2} \right) \tilde{\mathbf{g}}_a \quad (2.41)$$

Comparing this to the non-dimensionalization transformation relationship for $\boldsymbol{\epsilon}$ given by Eq. (2.26), we obtain the non-dimensional wheel torque equation

$$\dot{\boldsymbol{\mu}} = \boldsymbol{\epsilon} \quad (2.42)$$

2.3 Perturbative Force Modeling

In the previous sections, we derived the rotational and attitude equations of motion for a spacecraft, without specifying the external moments (\mathbf{M}). In real applications, this quantity is a composite of dozens of external moments acting on the vehicle. It is our desire to model the most significant of these. In Chapter IV, we will see the effects these moments have on the attitude dynamics of the vehicle during maneuvers.

The external moments acting on a spacecraft in orbit about the Earth vary in magnitude (depending on altitude and spacecraft configuration) from large effects such as aerodynamic drag in low earth orbit, to smaller effects such as gravitational interactions between the vehicle and the Sun, Moon, and other planets.

Gravity gradient and solar pressure effects are perhaps the most significant from an attitude control perspective. Deviations from a pure two-body problem (e.g. Earth oblateness and third body effects from the Sun, Moon, and other planets) primarily affect the satellite's orbit. These effects are certainly important for accurate orbit estimation. However, even though the inclusion of gravity gradient and solar pressure torques couples the orbital and rotational equations of motion, the assumption of an inertially fixed orbit with perfectly known orbital elements is sufficient for preliminary analysis.

Accordingly, we make the assumptions in the following derivations that the spacecraft's *translational* motion is that of a point mass in orbit about a perfectly spherical Earth of uniform mass distribution, with no interaction with the atmosphere or other celestial bodies. Orbital parameters for the GPS Block IIR and Hubble Space Telescope are listed in Appendices B and C. Both vehicles have *nearly* circular orbits with altitudes of 20,182 km and 615 km, respectively, and inclinations of 54° and 45°. For ease of simulation, the right ascension of the node (Ω) was assumed to be zero and the argument of perigee (ω) was assumed to be $\pi/2$ for both vehicles. While ω is not defined for exactly circular orbits, the simulation was left as general as possible to allow application to elliptical orbits. Such assumptions allowed easy calculation of initial velocity components in the inertial frame. Ω and ω were also assumed constant, which is reasonable if the vehicles are kept on station

(either automatically or via ground commands) or if simulation times are limited to only a few orbital periods.

The two-body equations of motion are well known and can be expressed in many forms. However, in our inertially fixed Earth-centered frame \mathcal{F}_i , they can be expressed as a set of six first order differential equations (in matrix form) as

$$\dot{\tilde{\mathbf{R}}} = \tilde{\mathbf{V}} \quad (2.43)$$

$$\dot{\tilde{\mathbf{V}}} = -\frac{\mu_{\oplus}}{|\tilde{\mathbf{R}}|^3}\tilde{\mathbf{R}} \quad (2.44)$$

where

μ_{\oplus} = Earth gravitational parameter

$\tilde{\mathbf{R}}$ = components of position vector from Earth center to spacecraft center of mass

$\tilde{\mathbf{V}}$ = components of velocity vector of spacecraft center of mass

2.3.1 Gravity Gradient Torques. Gravity gradient torques arise due to asymmetries in the vehicle's mass distribution and the resulting inequity of gravitational attraction between the central attractive body (e.g. Earth) and spacecraft mass elements for certain vehicle orientations. If the vehicle were perfectly spherical and of uniform mass distribution, the sum of gravitational forces on the differential elements of mass comprising the vehicle would offset each other resulting in no net torque on the vehicle regardless of orientation. However, as is the case with most modern spacecraft (including GPS Block IIR and the Hubble Space Telescope), mission requirements result in asymmetry in mass distribution.

Following Kaplan [13:200] and Hughes [11:235], the net gravity gradient torque ($\tilde{\mathbf{M}}_g$) acting on a body \mathcal{B} can be expressed as

$$\tilde{\mathbf{M}}_g = \int_{\mathcal{B}} \tilde{\mathbf{r}} \times \left[\frac{-\mu_{\oplus} (\tilde{\mathbf{R}} + \tilde{\mathbf{r}}) d\tilde{m}}{|\tilde{\mathbf{R}} + \tilde{\mathbf{r}}|^3} \right] \quad (2.45)$$

where $\tilde{\mathbf{R}}$ = vector from attracting body center of mass to \mathcal{B} center of mass
 $\tilde{\mathbf{r}}$ = vector from \mathcal{B} center of mass to differential mass element dm

It is the dependency of $\tilde{\mathbf{M}}_g$ on $\tilde{\mathbf{R}}$ which couples the orbital equations of motion (Eq. (2.44)) and the rotational equations of motion (Eq. (2.11)) since the gravity gradient torque is one component of the overall external moment $\tilde{\mathbf{M}}$. Thus, as the orbital equations are integrated, the resulting position data are used to calculate gravitational torques which are in turn used in the integration of the rotational equations of motion.

Summaries of the mass properties of the GPS Block IIR and Hubble Space Telescope vehicles are included in Appendices B and C. While detailed mass data for every vehicle subsystem and location were available for GPS Block IIR [17], only total mass was available for the Hubble Space Telescope [2:1].

The most accurate yet easily calculable approach to determining the resultant torques is to use a series expansion for $\left| \tilde{\mathbf{R}} + \tilde{\mathbf{r}} \right|^3$, recognizing that $\left| \tilde{\mathbf{r}} \right| / \left| \tilde{\mathbf{R}} \right| \ll 1$. After dropping squared and higher terms, and some manipulation (see Hughes [11:235-237]), the expression for total gravity gradient torque (in matrix form in \mathcal{F}_b) becomes

$$\tilde{\mathbf{M}}_g = \frac{3\mu_\oplus}{\left| \tilde{\mathbf{R}} \right|^3} \mathbf{c}_3^\times \tilde{\mathbf{I}} \mathbf{c}_3 \quad (2.46)$$

where $\mathbf{c}_3 = [c_{13} \ c_{23} \ c_{33}]^T$ and c_{i3} , ($i = 1 \dots 3$) are the direction cosines found by calculating $\hat{\mathbf{b}}_i \cdot \left(\tilde{\mathbf{R}} / \left| \tilde{\mathbf{R}} \right| \right)$.

Analysis of the above expression reveals that for an asymmetric vehicle (principle moments of inertia unequal), the net gravity gradient torque on the vehicle is zero when any of the principal axes are aligned with the local vertical $\left(\tilde{\mathbf{R}} / \left| \tilde{\mathbf{R}} \right| \right)$. Stability analysis of these equilibria shows that the only stable orientation for a vehicle in a circular orbit is such that the minor axis is aligned with the local vertical [11],[5],[13].

Figure 2.2 shows the relationship between the body frame and inertial frame for the GPS Block IIR spacecraft in orbit. The relationship for Hubble Space Telescope is similar (see Appendix C for body frame orientation).

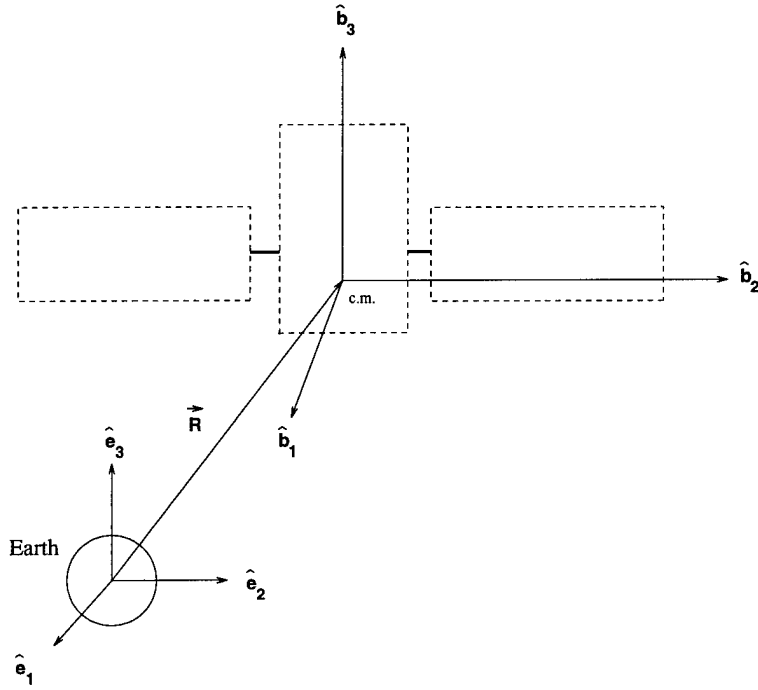


Figure 2.2 GPS Block IIR Gravity Gradient Model

2.3.2 Solar Pressure Torques. Small torques on a spacecraft can also occur as a result of uneven absorption and reflection of electro-magnetic radiation (photons) by the spacecraft surfaces. The primary source of high energy radiation for an Earth-orbiting satellite is obviously the Sun, and the effects are clearly greater for large asymmetric vehicles than for smaller, more symmetric ones. Since both the GPS Block IIR and Hubble Space Telescope vehicles have large appendages (solar arrays) and the main bodies are asymmetric, the effects of solar pressure induced torques on a maneuvering vehicle are of interest.

As is more fully derived in Agrawal [1:133-135], the net solar pressure induced torque on a surface \mathcal{S} with uniform material properties, discounting shadowing effects, is given by:

$$\vec{\tilde{M}}_s = \int_{\mathcal{S}} -(\hat{\mathbf{n}} \cdot \hat{\mathbf{S}}) \vec{\mathbf{r}} \times \left[(\rho_a + \rho_d) \hat{\mathbf{S}} + \left(2\rho_s + \frac{2\rho_d}{3} \right) \hat{\mathbf{n}} \right] P_{sun} dA \quad (2.47)$$

or, since $\rho_a + \rho_d + \rho_s = 1$:

$$\vec{\tilde{M}}_s = \int_{\mathcal{S}} -(\hat{\mathbf{n}} \cdot \hat{\mathbf{S}}) \vec{\mathbf{r}} \times \left[(1 - \rho_s) \hat{\mathbf{S}} + 2 \left(\rho_s + \frac{\rho_d}{3} \right) \hat{\mathbf{n}} \right] P_{sun} dA \quad (2.48)$$

where:

- $\hat{\mathbf{S}}$ = unit vector from Sun to differential area dA
- $\hat{\mathbf{n}}$ = externally oriented unit normal vector of dA
- $\tilde{\mathbf{r}}$ = vector from vehicle center of mass to the center of pressure of dA
- P_{sun} = solar radiation pressure
- ρ_a = fraction of radiation absorbed by dA
- ρ_d = fraction of radiation diffusely reflected by dA
- ρ_s = fraction of radiation specularly reflected by dA

It is important to restate that these equations do not take into account shadowing effects of one surface on another (e.g. solar array shadowing main body or “back” face of spacecraft entirely in shadow). For a three-dimensional surface such as the main body of the GPS Block IIR and the Hubble Space Telescope, if no provision is made to exclude the side not facing the Sun from the equations, the resulting torques calculated will in effect assume that the photons have traveled *through* the front face and are impinging on the rear faces as well.

Unfortunately, the main body surfaces cannot reasonably be ignored for either GPS Block IIR or the Hubble Space Telescope, since the moment arms (from vehicle mass center to surface center of pressure) of the solar pressure torques about the $\hat{\mathbf{b}}_1$ and $\hat{\mathbf{b}}_2$ axes are much greater than those of the solar arrays, and the assumption of symmetry of the two solar arrays with respect to the $\hat{\mathbf{b}}_1 - \hat{\mathbf{b}}_3$ plane negates any torques about the $\hat{\mathbf{b}}_3$ axis from the arrays.

For a spacecraft with discrete components, the solar pressure torque calculation is reduced to a sum of the contribution from each of the component surfaces, recognizing that any main body surfaces in shadow ($\hat{\mathbf{n}}_i \cdot \hat{\mathbf{S}} \geq 0$) contribute nothing. In matrix form, the equation is

$$\tilde{\mathbf{M}}_s = \sum_{i=1}^n \left[-(\mathbf{n}_i^T \mathbf{S}) \tilde{\mathbf{r}}_i^{\times} \left[(1 - \rho_s) \mathbf{S} + 2 \left(\rho_s + \frac{\rho_d}{3} \right) \mathbf{n}_i \right] P_{sun} A_i \right] \quad (2.49)$$

where:

\mathbf{S} = components of unit vector from Sun to vehicle

\mathbf{n}_i = components of externally oriented unit normal vector of A_i

$\tilde{\mathbf{r}}_i$ = components of vector from vehicle center of mass to the center of pressure of A_i

Note in Figure 2.3 that the GPS Block IIR vehicle is modeled as eight planar rectangular surfaces, only six of which can ever be in shadow (the main body “sides”, “top”, and “bottom”). For the Hubble Space Telescope (Figure 2.4), however, the two main body cylinders are modeled such that half the cylinders are always in sun unless the $\hat{\mathbf{b}}_3$ axis is parallel to $\hat{\mathbf{S}}$. Due to our choice of body frame, the effective areas of these half cylinders are rectangles with widths equal to the cylinder diameters and heights equal to the cylinder heights, scaled to account for Sun vector angle by the $\mathbf{n}_i^T \mathbf{S}$ term. The center of pressure thus “moves” on the surface such that it is always in the center of the effective area, and the normal vector is defined as the surface normal at the center of pressure (with only $\hat{\mathbf{b}}_1$ and $\hat{\mathbf{b}}_2$ components).

Differences in the absorptivity and reflectivity of various parts of the spacecraft will also result in solar pressure differentials. For example, it would be expected that solar arrays have a higher absorptivity than the main body, which is typically covered in layers of reflective material. However, for simplicity of modeling, the material properties of both the GPS Block IIR and Hubble Space Telescope were assumed constant across all surfaces, with spectral reflectivity higher than diffuse reflectivity and absorptivity (see Appendices B and C for assumed values).

Due to the large distances from the Sun to the vehicle for an Earth-orbiting satellite and the relatively small size of the vehicle, it is reasonable to assume that the Sun vector direction is constant across all exposed surfaces for any point in time. However, since the Earth is moving relative to the Sun, the Sun vector *does* move with respect to our Earth-centered inertial reference frame \mathcal{F}_i . Since the Earth’s orbit is nearly circular and by definition of the ecliptic plane has inclination of zero [3], it is reasonable to assume that the Sun vector “rotates” at a constant angular rate in the $\hat{\mathbf{e}}_1 - \hat{\mathbf{e}}_2$ plane of our inertial

reference frame. If the angle of the Sun vector from the \hat{e}_1 axis is given by θ_s , then the Sun vector in \mathcal{F}_i can be represented in matrix form as

$$\mathbf{S} = [\cos \theta_s \quad \sin \theta_s \quad 0]^T \quad (2.50)$$

and the angle θ_s is governed by

$$\dot{\theta}_s = \omega_{sun} = \frac{2\pi}{365.25 \text{ days}} \approx 1.99 \times 10^{-7} \text{ rad/s} = \text{constant} \quad (2.51)$$

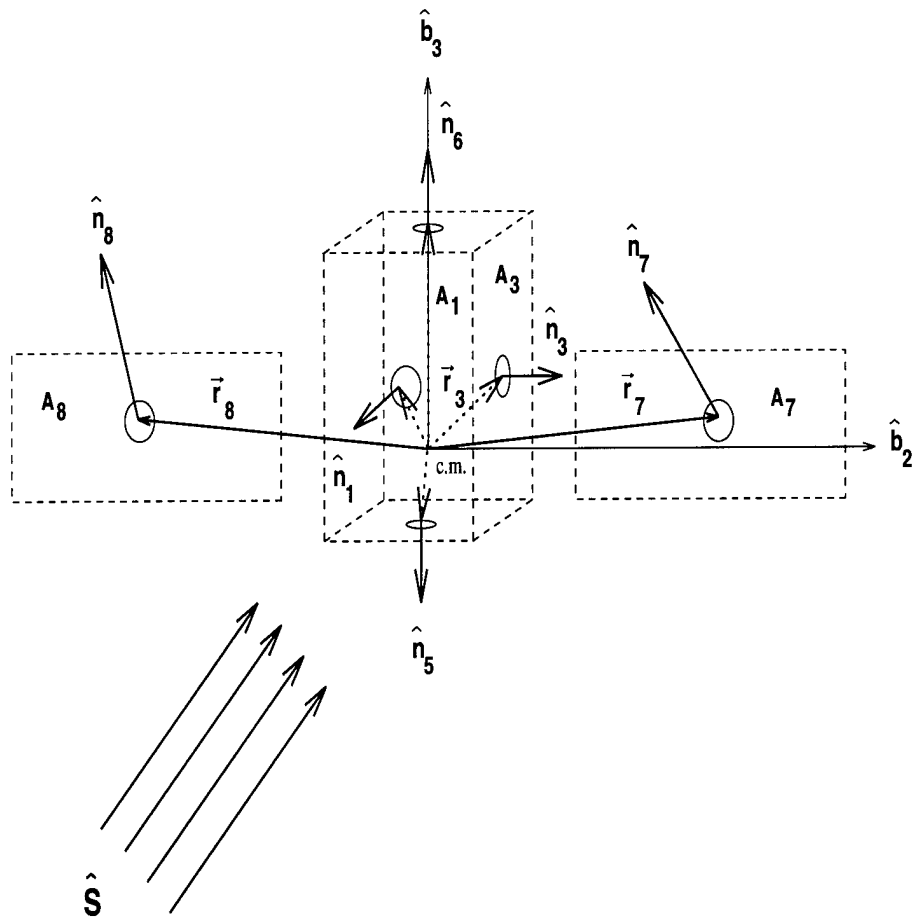


Figure 2.3 GPS Block IIR Idealization for Solar Pressure Modeling

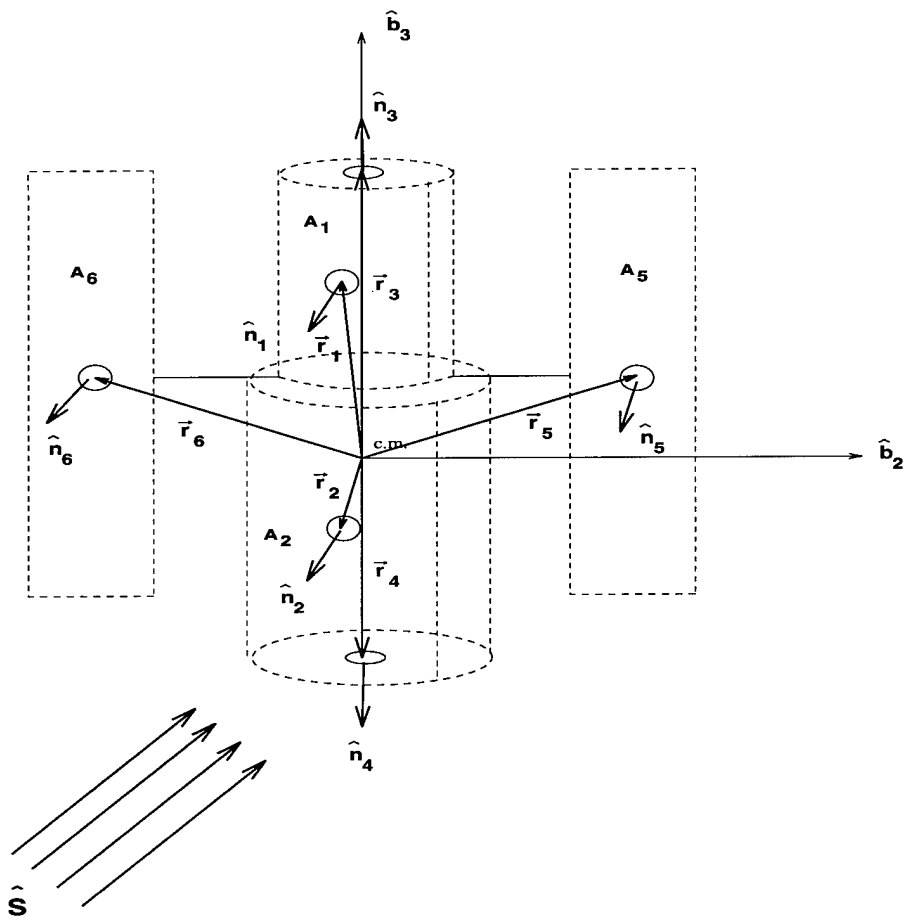


Figure 2.4 *Hubble Space Telescope Idealization for Solar Pressure Modeling*

2.4 Attitude Equations

There are numerous choices of parameters available to express the attitude of the vehicle body-fixed frame \mathcal{F}_b with respect to the inertial frame \mathcal{F}_i . Each has its own advantages and disadvantages depending on the application.

Euler angles, usually represented as three single axis rotations about the body axes, are perhaps the most commonly used parameters in spacecraft design, mission analysis, and spacecraft operations. This is due to ease of visualization and intuitive relationship between the body frame (containing spacecraft sensors and communications hardware) and the inertial frame (from which the sensors obtain data). However, the well documented singularities in the differential equations relating vehicle angular velocities to Euler angles leads to computational difficulties for passage through certain orientations (depending on the Euler angle set used).

Attitude equations utilizing quaternions, with a redundant fourth parameter, avoid these computational singularities. However, the cost of numerical stability is a loss of simple physical meaning of the four parameters to planners and analysts.

In all of the spacecraft command and control and simulation systems this author has dealt with, quaternions are used for attitude propagation within the modeling software, and Euler angles are calculated from the quaternions for display to the end user.

The quaternions are dimensionless parameters by definition. Following Chobotov [5:10], if the four quaternion parameters are represented by the column matrix $\mathbf{q} = (q_1 \ q_2 \ q_3 \ q_4)^T$, the attitude equations can be written as

$$\dot{\mathbf{q}} = \frac{1}{2} \begin{pmatrix} 0 & \tilde{\omega}_3 & -\tilde{\omega}_2 & \tilde{\omega}_1 \\ -\tilde{\omega}_3 & 0 & \tilde{\omega}_1 & \tilde{\omega}_2 \\ \tilde{\omega}_2 & -\tilde{\omega}_1 & 0 & \tilde{\omega}_3 \\ -\tilde{\omega}_1 & -\tilde{\omega}_2 & -\tilde{\omega}_3 & 0 \end{pmatrix} \mathbf{q} \quad (2.52)$$

It is really unnecessary to distinguish between the dimensional and non-dimensional forms of this equation, since if we substitute in for dt from Eq. (2.33) and note the relationship between $\tilde{\omega}$ and ω from Eq. (2.31), Eq. (2.52) becomes

$$\frac{d\mathbf{q}}{dt} \begin{pmatrix} \tilde{h} \\ \tilde{I}_c \end{pmatrix} = \frac{1}{2} \begin{pmatrix} \tilde{h} \\ \tilde{I}_c \end{pmatrix} \begin{pmatrix} 0 & \omega_3 & -\omega_2 & \omega_1 \\ -\omega_3 & 0 & \omega_1 & \omega_2 \\ \omega_2 & -\omega_1 & 0 & \omega_3 \\ -\omega_1 & -\omega_2 & -\omega_3 & 0 \end{pmatrix} \mathbf{q} \quad (2.53)$$

Clearly, elimination of common terms from both sides thus yields the non-dimensional form of the equation, which is the same form except that non-dimensional angular rates are used. Using the superscript notation Ω^\times to represent the 4×4 skew symmetric matrix of angular velocities (not to be confused with the 3×3 matrix ω^\times), the attitude equations can be expressed in the compact matrix form

$$\dot{\mathbf{q}} = \frac{1}{2} \Omega^\times \mathbf{q} \quad (2.54)$$

The quaternions obviously vary with time if the spacecraft is rotating with respect to the inertial frame. Certainly, the orientation of one orthogonal reference frame \mathcal{F}_b to another \mathcal{F}_i can be described by a 3×3 rotation matrix \mathbf{T} that also varies with time, and whose columns are the orthonormal basis vectors of \mathcal{F}_b expressed in terms of the basis vectors of \mathcal{F}_i . Again following Chobotov [5:9], the elements of this rotation matrix can be expressed in terms of the quaternions as

$$\mathbf{T}_{11} = q_1^2 - q_2^2 - q_3^2 + q_4^2$$

$$\mathbf{T}_{12} = 2(q_1 q_2 + q_3 q_4)$$

$$\mathbf{T}_{13} = 2(q_1 q_3 - q_2 q_4)$$

$$\mathbf{T}_{21} = 2(q_1 q_2 - q_3 q_4)$$

$$\mathbf{T}_{22} = -q_1^2 + q_2^2 - q_3^2 + q_4^2$$

$$\mathbf{T}_{23} = 2(q_1 q_4 + q_2 q_3)$$

$$\mathbf{T}_{31} = 2(q_1 q_3 + q_2 q_4)$$

$$\mathbf{T}_{32} = 2(-q_1 q_4 + q_2 q_3)$$

$$\mathbf{T}_{22} = -q_1^2 - q_2^2 + q_3^2 + q_4^2$$

Furthermore, since the rotation matrix can also be constructed as the product of three single-axis rotation matrices involving Euler angles (choice of sequence dependent on application), it should be clear that the Euler angles can be extracted from the \mathbf{T} found using quaternions. Angular rates in terms of the Euler angles can likewise be derived. The reader is referred to Chobotov [5:6-7].

2.5 Equations Summary

Before continuing, it will be useful to have all of the equations of motion summarized in one location for future reference (renumbered as well). Note that only the non-dimensional forms of the rotational and wheel torque equations are given, since they are used exclusively in the following sections. For subsequent developments which assume no external torques (as in Chapter III), the rotational equations of motion do not contain \mathbf{M} , and thus the gravity gradient and solar pressure torque equations used to calculate the components of \mathbf{M} (i.e. \mathbf{M}_g and \mathbf{M}_s) are not necessary. The following equations are for the general case *with external torques* included (which will be used in Chapter 5), and are provided in matrix form. All equations assume the matrices are expressed in \mathcal{F}_b except the orbital position, orbital velocity, and Sun vector equations. For definitions of variables and constants the reader is referred to the previous sections and to the *List of Symbols*.

$$\dot{\mathbf{x}} = \mathbf{x}^\times \boldsymbol{\omega} + \mathbf{M} \quad (2.55)$$

$$\dot{\boldsymbol{\mu}} = \boldsymbol{\varepsilon} \quad (2.56)$$

$$\dot{\mathbf{q}} = \frac{1}{2} \boldsymbol{\Omega}^\times \mathbf{q} \quad (2.57)$$

$$\left[\dot{\tilde{\mathbf{R}}} \right]_{\mathcal{F}_i} = \left[\tilde{\mathbf{V}} \right]_{\mathcal{F}_i} \quad (2.58)$$

$$\left[\dot{\tilde{\mathbf{V}}} \right]_{\mathcal{F}_i} = - \frac{\mu_\oplus}{|\tilde{\mathbf{R}}|^3} \left[\tilde{\mathbf{R}} \right]_{\mathcal{F}_i} \quad (2.59)$$

$$\dot{\theta}_s = \omega_{sun} \quad (2.60)$$

$$\mathbf{M} = \left(\frac{\tilde{I}_c}{\tilde{h}_o^2} \right) (\tilde{\mathbf{M}}_g + \tilde{\mathbf{M}}_s) \quad (2.61)$$

$$\tilde{\mathbf{M}}_g = \frac{3\mu}{|\tilde{\mathbf{R}}|^3} \mathbf{c}_3^\times \tilde{\mathbf{I}} \mathbf{c}_3 \quad (2.62)$$

$$\tilde{\mathbf{M}}_s = \sum_{i=1}^n \left[-(\mathbf{n}_i^T \mathbf{S}) \tilde{\mathbf{r}}_i^\times \left[(1 - \rho_s) \mathbf{S} + 2 \left(\rho_s + \frac{\rho_d}{3} \right) \mathbf{n}_i \right] P_{sun} A_i \right] \quad (2.63)$$

$$[\mathbf{S}]_{\mathcal{F}_i} = [\cos \theta_s \quad \sin \theta_s \quad 0]^T \quad (2.64)$$

III. Wheel Torque Control Law Derivation

The purpose of this chapter is to state the conditions on spacecraft momentum and wheel momenta necessary for a stationary platform (body angular rates very small), calculate some wheel torque controls to accomplish rest-to-rest and stationary platform maneuvers and discuss limitations on such maneuvers due to physical limitations of the wheels.

Examples of these maneuvers for specific spacecraft will be performed in Chapter 4 (without external perturbing torques) and Chapter 5 (with gravity gradient and solar pressure torques).

3.1 Stationary Platform Condition

Most spacecraft in operation today are used for communications or observation and thus have mission constraints that require them to remain Earth pointed (e.g. GPS) or essentially fixed in inertial space (e.g. Hubble Space Telescope) for long periods of time. This necessitates the ability to maintain the spacecraft attitude and counteract external perturbations such as gravity gradient and solar pressure torques. Also, especially in the case of the Hubble Space Telescope, it is often critical to be able to maneuver the vehicle from one stationary orientation to another with minimal induced motion on the vehicle (which might damage components such as solar arrays, antennas, or sensors).

It is immediately apparent from inspection of Eq. (2.31) that the vehicle will be stationary if

$$\boldsymbol{\omega} = \mathbf{J}^{-1}(\mathbf{x} - \mathbf{A}\boldsymbol{\mu}) = 0 \quad (3.1)$$

which leads to the **stationary platform condition**

$$\mathbf{x} = \mathbf{A}\boldsymbol{\mu} \quad (3.2)$$

For vehicles with 3 non-coplanar wheels, this can also be expressed as

$$\boldsymbol{\mu} = \mathbf{A}^{-1}\mathbf{x} \quad (3.3)$$

The physical interpretation of Eq. (3.2) is quite simple; for the platform to be stationary, the direction and magnitude of the spacecraft total momentum vector (\mathbf{x}) must be equal to the direction and magnitude of the total wheel momentum vector ($\mathbf{A}\boldsymbol{\mu}$) in the body frame for all time.

An interesting way of describing and visualizing this stationary platform condition was developed by Hall [8] by noting that since \mathbf{x} is normalized, conservation of angular momentum requires $\mathbf{x}^T\mathbf{x} = 1$, so that substituting from above ultimately yields

$$\boldsymbol{\mu}^T \mathbf{A}^T \mathbf{A} \boldsymbol{\mu} = 1 \quad (3.4)$$

which for a vehicle employing n momentum wheels, is readily recognized as a hyper-ellipsoid of dimension n in the space spanned by $(\mu_1 \ 0 \ \dots \ 0)$, $(0 \ \mu_2 \ 0 \ \dots \ 0)$, $(0 \ \dots \ 0 \ \mu_n)$, hereafter referred to as $\boldsymbol{\mu}$ space (or \mathcal{F}_μ). Thus, for a given value of total angular momentum (\tilde{h}_o), the platform \mathcal{R} will remain fixed with respect to inertial space (\mathcal{F}_i) as long as the wheel momenta $\boldsymbol{\mu} = (\mu_1 \ \mu_2 \ \dots \ \mu_n)$ lie on the surface of this wheel momenta ellipsoid and $\mathbf{x} = \mathbf{A}\boldsymbol{\mu}$.

Also, as is common in dynamics texts and attitude dynamics papers, the spacecraft total angular momentum itself can be represented by a sphere, in our case in \mathbf{x} space (see Fig. 3.1). Typically, this momentum sphere is used to visualize the stability of spacecraft motion about the angular momentum vector. However, in our applications, we will use this momentum sphere only to describe the spacecraft total momentum during reorientation maneuvers. It will prove particularly useful in showing how violations of assumptions on control torque magnitudes results in state errors.

While only three wheels are necessary for three degree of freedom attitude control, most vehicles employing them have a set of four, aligned in a “pyramid” fashion so that no combination of three of the wheels are co-planar (see Appendix C for GPS Blk IIR wheel orientations). Having a fourth wheel not only provides redundancy in the event of failure or degradation of performance of a single wheel, but also allows more total momentum storage by the wheels. Thus, while in some spacecraft only three of the four wheels are used simultaneously (e.g. Hubble Space Telescope), in others, the fourth wheel is routinely used to increase control authority (e.g. GPS Block IIR) [20],[2],[7]. For ease of visualization,

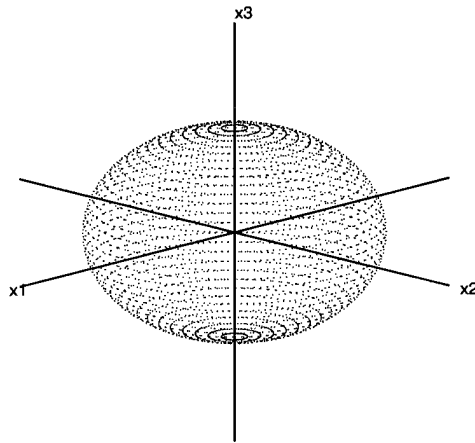


Figure 3.1 *Spacecraft Total Momentum Sphere*

we will focus primarily on reorientation maneuvers using sets of three wheels. This allows representation of the stationary platform condition by a three-dimensional wheel momenta ellipsoid. However, in later sections we will briefly discuss use of the fourth wheel in cases where the primary three wheels cannot generate enough angular momentum to maintain a stationary platform.

Figures 3.2 through 3.9 are examples of wheel momenta ellipsoids for vehicles using three momentum wheels for attitude control, for varying orientations of the wheels within the body frame. Notice that for the case of orthogonal wheels (Figs. 3.2 and 3.3), the ellipsoid reduces to a sphere, and that as the wheels approach co-planarity (Figs. 3.6 and 3.7), the ellipsoid elongates. If the three wheels are co-planar (but none co-linear), the principal axis of the ellipse perpendicular to the plane becomes infinitely large. This reflects the fact that the wheels can no longer “absorb” the spacecraft’s angular momentum (thus achieving stationary platform condition), no matter how small, if the direction of the angular momentum is not within the plane formed by the three wheels. As the three wheels become co-linear (see Fig. 3.9), two of the three principal axes become infinitely large, suggesting that the wheels can maintain a stationary platform only if the total angular momentum vector is aligned with the wheel spin axes.

It is important to note that the discussion in this chapter will be limited by the assumption that the spacecraft total angular momentum is constant ($\tilde{h}_o = const$), so that the momentum sphere and wheel momenta ellipsoid are of constant “size”. In other words, since these two graphical tools are constructed in non-dimensional variables (\mathbf{x} and $\boldsymbol{\mu}$), if the magnitude of the total angular momentum changes with time, the wheel momenta ellipsoid will “expand” or “contract” relative to the nominal ellipsoid calculated based on \tilde{h}_o . This will be discussed in more depth in Chapter 5 when perturbing torques are introduced into the simulations.

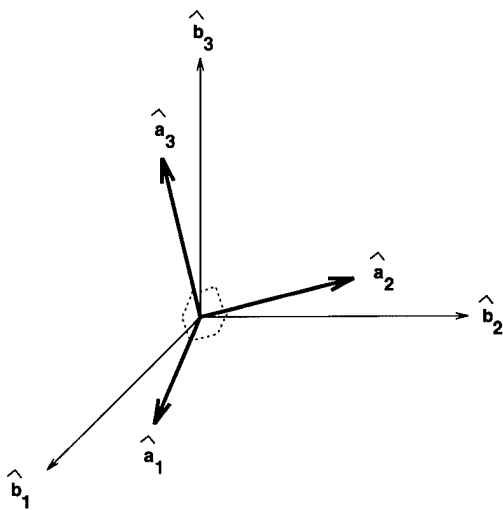


Figure 3.2 *Orthogonal Wheels*

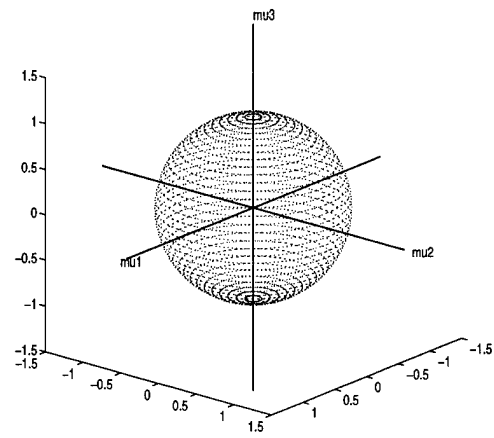


Figure 3.3 *Wheel Momenta Ellipsoid (Orthogonal Wheels)*

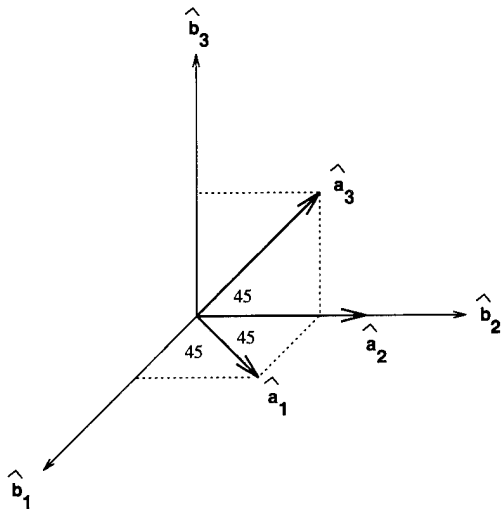


Figure 3.4 *Pyramidal Wheels*

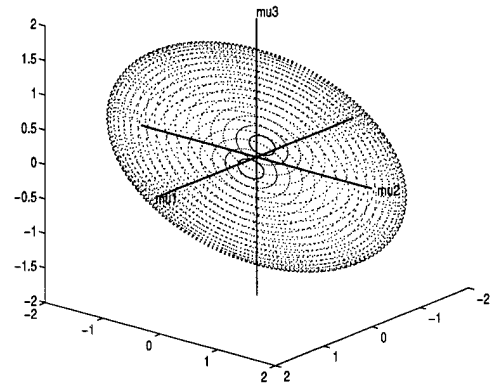


Figure 3.5 *Wheel Momenta Ellipsoid (Pyramidal Wheels)*

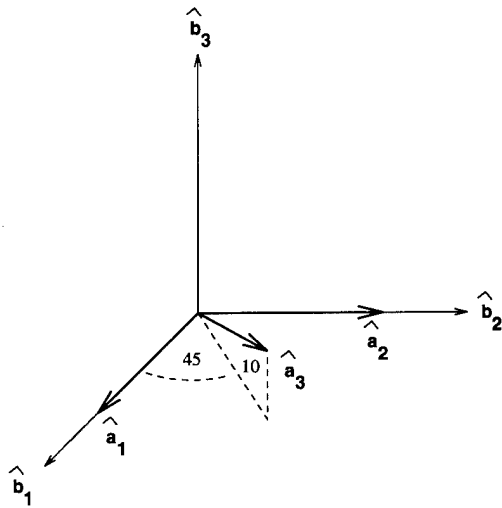


Figure 3.6 *Nearly Co-planar Wheels*

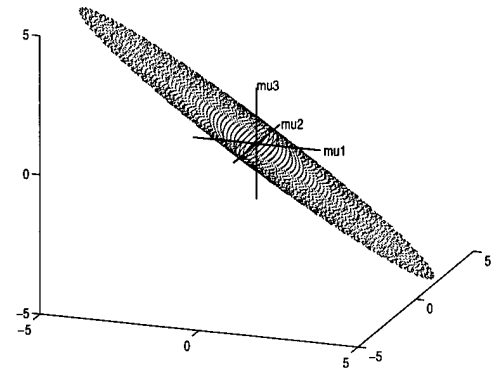


Figure 3.7 *Wheel Momentum Ellipsoid (Nearly Co-planar Wheels)*

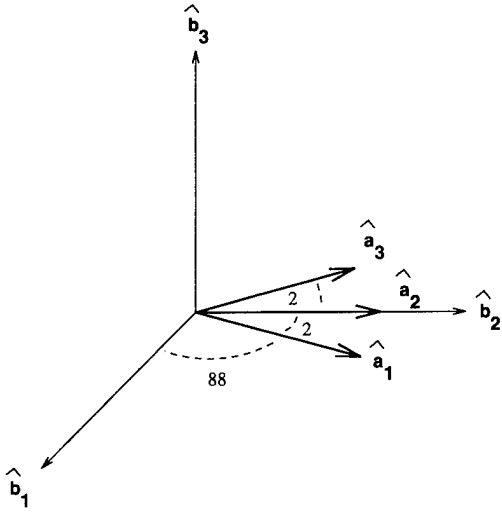


Figure 3.8 Nearly Co-linear Wheels

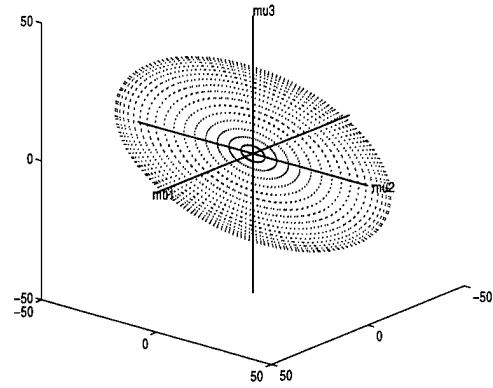


Figure 3.9 Wheel Momentum Ellipsoid (Nearly Co-linear Wheels)

Another important relationship to understand is that between the direction of the total angular momentum vector (\mathbf{x}), the direction of the wheel momenta vector ($\mathbf{A}\boldsymbol{\mu}$), and the attitude of the spacecraft with respect to \mathcal{F}_i . Let us assume that the wheels can absorb all the angular momentum of the spacecraft, so that the stationary platform condition $\mathbf{x} = \mathbf{A}\boldsymbol{\mu}$ (which is expressed in \mathcal{F}_b) holds. Also assume that we know (i.e. can accurately estimate) the direction of the spacecraft angular momentum vector in inertial space (\mathbf{x}_i), the wheel angular rates ($\boldsymbol{\omega}_s$), inertias ($\tilde{\mathbf{I}}_s$), and the orientation of the wheels with respect to the body frame (\mathbf{A}). Finally, let the attitude of the spacecraft body frame \mathcal{F}_b with respect to inertial \mathcal{F}_i be given by the rotation matrix \mathbf{T} . We can thus calculate the spacecraft total momentum in the body frame as

$$\mathbf{x} = \mathbf{T}\mathbf{x}_i \quad (3.5)$$

Substituting $\mathbf{A}\boldsymbol{\mu}$ in for \mathbf{x} and solving for $\boldsymbol{\mu}$ we obtain

$$\boldsymbol{\mu} = \mathbf{A}^{-1}\mathbf{T}\mathbf{x}_i \quad (3.6)$$

which is strictly only valid for a vehicle with three non-coplanar wheels (\mathbf{A} square and invertible). Since \mathbf{x}_i is constant in the absence of external torques, the vehicle can thus be maintained stationary at *any* attitude by varying the wheel momenta $\boldsymbol{\mu}$.

A useful extension of this result is that given a desired attitude for the vehicle, known wheel inertias and orientations in \mathcal{F}_b , and a known constant total momentum in \mathcal{F}_i , we can calculate the required wheel angular velocities to maintain a stationary platform as follows:

From Eqs. (2.14) and (2.15), we know

$$\tilde{\mathbf{h}}_a = \tilde{\mathbf{I}}_s \mathbf{A}^T \tilde{\boldsymbol{\omega}} + \tilde{\mathbf{I}}_s \tilde{\boldsymbol{\omega}}_s \quad (3.7)$$

Noting that for a stationary platform, $\tilde{\boldsymbol{\omega}} = 0$, we can solve for $\tilde{\boldsymbol{\omega}}_s$ to obtain

$$\tilde{\boldsymbol{\omega}}_s = \tilde{\mathbf{I}}_s^{-1} \tilde{\mathbf{h}}_a \quad (3.8)$$

Recognizing from Eq. (2.24) that $\tilde{\mathbf{h}}_a = \tilde{h}_o \boldsymbol{\mu}$, we can substitute into the above to obtain

$$\tilde{\boldsymbol{\omega}}_s = \tilde{h}_o \tilde{\mathbf{I}}_s^{-1} \boldsymbol{\mu} \quad (3.9)$$

Substituting from Eq.(3.3) for $\boldsymbol{\mu}$ yields

$$\tilde{\boldsymbol{\omega}}_s = \tilde{h}_o \left(\mathbf{A} \tilde{\mathbf{I}}_s \right)^{-1} \mathbf{x} \quad (3.10)$$

Finally, substituting from Eq. (3.5) for \mathbf{x} results in

$$\tilde{\boldsymbol{\omega}}_s = \tilde{h}_o \left(\mathbf{A} \tilde{\mathbf{I}}_s \right)^{-1} \mathbf{T} \mathbf{x}_i \quad (3.11)$$

A final useful extension of Eq. (3.5) is calculation of final wheel momenta for a maneuver. Given rotation matrices relating the body frame to inertial at an initial and final time (\mathbf{T}_o and \mathbf{T}_f), initial wheel momenta $\boldsymbol{\mu}_o$, and using the fact that \mathbf{x}_i is constant, it is easily shown that

$$\boldsymbol{\mu}_f = \mathbf{A}^{-1} \mathbf{T}_f \mathbf{T}_o^T \mathbf{A} \boldsymbol{\mu}_o \quad (3.12)$$

As a simple example, consider a vehicle with three orthogonal wheels ($\mathbf{A} = \mathbf{A}^{-1} = \mathcal{I}$) and total angular momentum vector pointing in the $\hat{\mathbf{e}}_1$ direction ($\mathbf{x}_i = (1 \ 0 \ 0)^T$). We assume the vehicle is stationary in \mathcal{F}_i .

If we wish to have the spacecraft $\hat{\mathbf{b}}_1$ axis aligned with the angular momentum vector (and thus parallel to $\hat{\mathbf{e}}_1$), then $\mathbf{T}_o = \mathcal{I}$, so by Eq. (3.6), $\boldsymbol{\mu} = (1 \ 0 \ 0)^T$. In other words, to maintain this attitude, only \mathcal{W}_1 is rotating, such that it contains all of the angular momentum of the vehicle.

To demonstrate that this attitude is not unique and that any is achievable (given our previous assumptions), let us now assume that the vehicle has been reoriented (without external forces) by a negative 45° rotation about the $\hat{\mathbf{b}}_3$ axis and is again stationary. The total momentum has not changed with respect to \mathcal{F}_i . Using Eq. (3.12), we find that now $\boldsymbol{\mu} = (1/\sqrt{2} \ 1/\sqrt{2} \ 0)^T$, meaning that both \mathcal{W}_1 and \mathcal{W}_2 are in use and each contribute half the total angular momentum of the vehicle. The angular rates of the wheels necessary for given wheel inertias and vehicle total angular momentum could be calculated using Eq. (3.10).

One final but important point which was identified by Hall [8] is the following: Although the relationship between the platform and momentum wheel angular momentum vectors direction and magnitude is uniquely determined by the stationary platform condition $\mathbf{x} = \mathbf{A}\boldsymbol{\mu}$, the attitude of the spacecraft with respect to inertial space is determined only within a rotation about the angular momentum vector. Thus, for all the maneuvers we will perform in the following sections, even though we can control the direction of the spacecraft angular momentum vector within the body, we cannot control the body rotation with respect to that vector. This will be particularly important when analyzing final state errors at the completion of maneuvers.

We will now address some additional issues regarding use of the wheel momentum ellipsoid to specify the stationary platform condition, derive two classes of wheel torque control laws for rest-to-rest attitude maneuvers, and run several representative simulations for actual spacecraft to characterize the utility and behavior of these control laws.

3.2 Unachievable Regions on the Wheel Momenta Ellipsoid

Since the wheel momenta ellipsoid is normalized (scaled by \tilde{h}_o), interpretation of points on the ellipsoid can be misleading when used to assess momentum transfer in actual spacecraft. There may in fact be regions on the wheel momenta ellipsoid that are unachievable because they require unrealistically high angular momentum for the individual wheels. Momentum wheels obviously have fixed axial inertias and maximum achievable angular rates, thereby limiting the total momentum an individual wheel can generate, as well as the total momentum that can be generated by the set of three wheels in certain directions within the body frame \mathcal{F}_b .

Consider a spacecraft using three orthogonal momentum wheels, with axial inertias of $\tilde{I}_s = 0.1 \text{ kg m}^2$ and maximum achievable angular rates of $\omega_{smax} = \pm 100 \text{ rad/s}$. The maximum momentum that a single wheel can store (in its axial direction) is thus $\tilde{h}_{max} = \tilde{I}_s \omega_{smax} = \pm 10 \text{ kg m}^2/\text{s}$. The wheel momenta ellipsoid representing the stationary platform condition for this vehicle is identical to Fig. 3.3. If we consider two wheels with spin axes aligned with the $\hat{\mathbf{b}}_1$ and $\hat{\mathbf{b}}_2$ body axes, the total momentum generated by these two wheels at maximum spin rate is $(\sqrt{2})\tilde{h}_{max} \approx \pm 14.14 \text{ kg m}^2/\text{s}$ in the $\pm(1/\sqrt{2})\hat{\mathbf{b}}_1 \pm (1/\sqrt{2})\hat{\mathbf{b}}_2$ direction. Obviously, extending this argument to three wheels, approximately $\pm 17.32 \text{ kg m}^2/\text{s}$ can be generated in $\pm(1/\sqrt{3})\hat{\mathbf{b}}_1 \pm (1/\sqrt{3})\hat{\mathbf{b}}_2 \pm (1/\sqrt{3})\hat{\mathbf{b}}_3$ direction.

First, let us suppose that we wish to maintain the platform in an inertially fixed orientation and the spacecraft total angular momentum magnitude is $\tilde{h}_o = 12 \text{ kg m}^2/\text{s}$, perhaps the result of buildup of angular momentum due to solar pressure and gravity gradient torques over time (the motivation for Chapter 5). Given the calculations in the last paragraph, it is apparent that a single wheel alone cannot produce enough angular momentum to maintain a stationary spacecraft. However, two wheels working together can. Thus, the only unachievable regions on the wheel momenta ellipsoid are at points "outside" the six planes which intersect the ellipsoid at the point on the μ axes where the wheel momentum maxima are reached (see Fig. 3.10). There are points in the $\mu_1 - \mu_2$, $\mu_1 - \mu_3$, and $\mu_2 - \mu_3$ planes that can be attained, and thus there are certain attitudes at which the spacecraft can be held stationary.

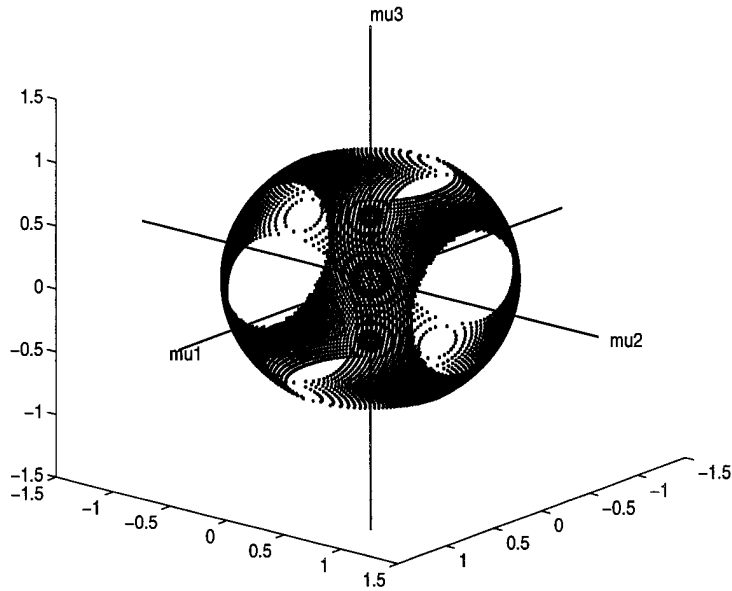


Figure 3.10 *Example 1 - Achievable Regions on Wheel Momenta Ellipsoid*

In the second example, assume that the total angular momentum magnitude is increased to $\tilde{h}_o = 15 \text{ kg m}^2/\text{s}$. Now, not only is a single wheel unable to maintain a stationary platform, but any two wheels working together are also insufficient. Certainly, three wheels at maximum angular rates can generate enough momentum. In terms of the wheel momenta ellipsoid, this means that no points on the ellipsoid in the $\mu_1 - \mu_2$, $\mu_1 - \mu_3$, or $\mu_2 - \mu_3$ planes can be reached given the wheel physical limitations, and in fact only certain regions off these planes are achievable. The achievable regions on the wheel momenta ellipsoid are those regions of the ellipsoid “inside” the six planes that define the maximum wheel momenta (see Fig. 3.11).

As a final extreme example, consider the case where $\tilde{h}_o = 20 \text{ kg m}^2/\text{s}$. It should be obvious that since even three wheels working together at maximum angular rates cannot generate more than $17.32 \text{ kg m}^2/\text{s}$, there is no way that the vehicle can be kept stationary using the momentum wheels alone *at any attitude*. Graphically, the six planes intersecting with the ellipsoid mentioned previously have moved inward so that the ellipsoid surface is entirely outside the cube enclosed by the planes.

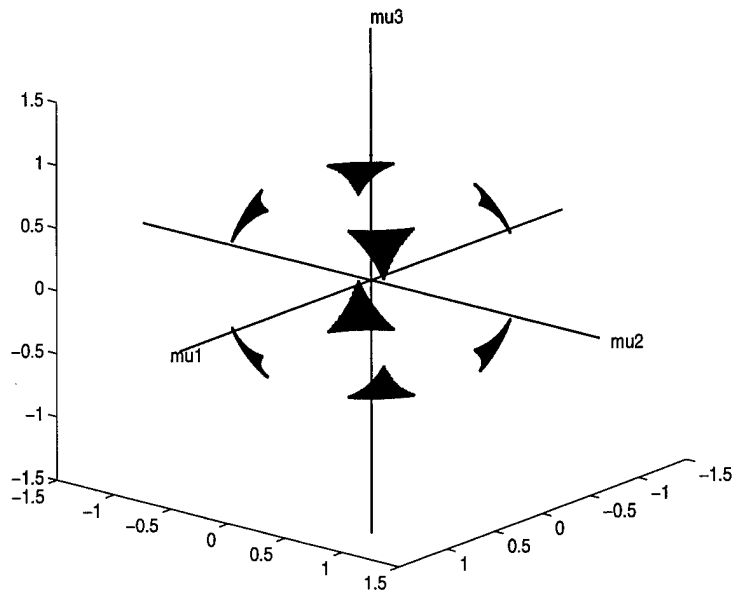


Figure 3.11 *Example 2 - Achievable Regions on Wheel Momenta Ellipsoid*

It is in such a case as this that the addition of the fourth momentum wheel proves useful. Since the redundant wheel is usually oriented such that it is non-coplanar with any other two wheels, it can provide a component of angular momentum in the direction of each of the other three wheels, thereby effectively increasing their momentum storage capacity. This in turn allows the wheels to maintain a stationary platform at higher total angular momentum magnitudes. In this example, if the fourth wheel spin axis were described in the body frame as $\hat{\mathbf{a}}_4 = (1/\sqrt{3} \ 1/\sqrt{3} \ 1/\sqrt{3})^T$, the maximum angular momentum capacity in the direction of each of the other three primary wheels is increased by a factor of $1/\sqrt{3} \approx 0.58$ to approximately $15.8 \text{ kg m}^2/\text{s}$. Furthermore, in the direction of the fourth wheel, the total momentum capacity of the four wheels at maximum angular rates is increased to approximately $17.32 + 10.00 = 27.32 \text{ kg m}^2/\text{s}$. Thus, in our extreme example above, the addition of the fourth wheel would result in regions of the momenta ellipsoid that *are* achievable (similar to Fig 3.11), and thus attitudes for which the vehicle *can* be held stationary.

The implications of the fourth wheel in maneuvers are apparent; if we wish to reorient the spacecraft from one stationary condition to another, the wheel torque control must be such that the wheel momenta are within the achievable regions defined by the cube discussed above. Also, if we choose a torque control law that runs tangent to the surface of the wheel momenta ellipsoid (which is the point of Section 3.5), we obviously must choose that path such that it avoids the unachievable regions on the surface.

Although the above examples were for sets of orthogonal wheels, it should be apparent that the same arguments hold for non-orthogonal wheels. The only difference is that since the wheel momenta ellipsoids are not symmetric with respect to the μ axes, the intersection of the six planes with the ellipsoid produces slightly different results (see Fig. 3.12).

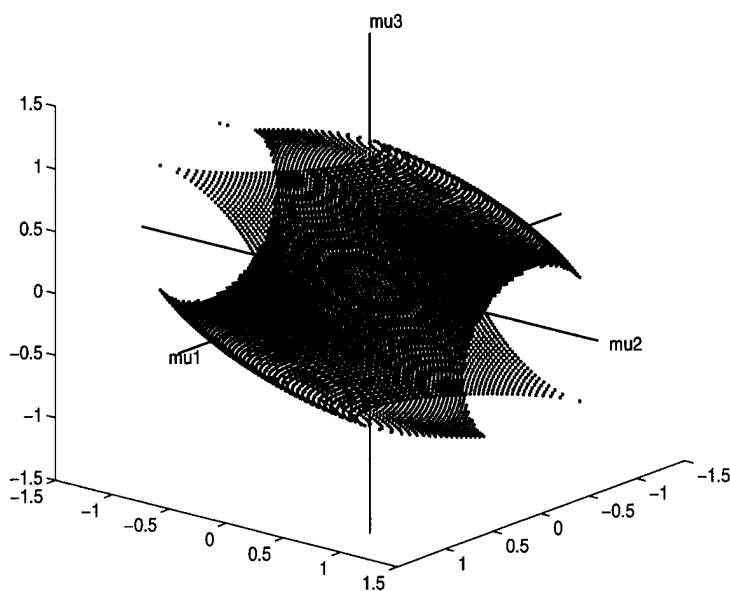


Figure 3.12 *Achievable Regions on Wheel Momenta Ellipsoid (Non-orthogonal Wheels)*

Now that we understand the limits of the stationary platform condition and the use of the wheel momenta ellipsoids to visualize it, let us develop some torque control laws to allow us to reorient the vehicle from one stationary platform state to another (rest-to-rest). In Section 3.4 we address a simple constant wheel torque case to use as a baseline for comparison with a sub-optimal control law developed in Section 3.5.

Before continuing, however, it is important to step back briefly and review some of the work accomplished by Hall [8] in terms of stability of motion and allowable wheel torques.

3.3 Allowable Torque Magnitudes

Hall [8] shows that for our idealized rigid spacecraft with embedded momentum wheels, the system Hamiltonian, using non-dimensional variables, is given by

$$H = \frac{1}{2} \mathbf{x}^T \mathbf{J}^{-1} \mathbf{x} - \boldsymbol{\mu}^T \mathbf{A}^T \mathbf{J}^{-1} \mathbf{x} + f(C) \quad (3.13)$$

where $f(C)$ is an arbitrary function of the first integral $C = \mathbf{x}^T \mathbf{x} / 2 = 1/2$ and does not affect the resulting equations of motion.

Furthermore, Hall shows that the Hamiltonian satisfies

$$\dot{H} = \boldsymbol{\varepsilon}^T \frac{\partial H}{\partial \boldsymbol{\mu}} = -\boldsymbol{\varepsilon}^T \mathbf{A}^T \mathbf{J}^{-1} \mathbf{x} \quad (3.14)$$

He then continues by analyzing equilibrium motions of the integrable zero torque case ($\boldsymbol{\varepsilon} = \mathbf{0}$), plotting equilibrium surfaces in " $\boldsymbol{\mu}H$ space" (which is 4-dimensional for a vehicle with three wheels), and using the method of averaging to show that for the case of small constant torques ($\boldsymbol{\varepsilon} = \epsilon \boldsymbol{\sigma}$, $\epsilon \ll 1$, $\boldsymbol{\sigma} = \text{const}$) the equilibrium surfaces contain exact solutions to the averaged equations. Extending this approach to that of small but not necessarily constant torques (such as the sub-optimal control laws in Section 3.5), he states [9:10]

...trajectories which start on or near an equilibrium surface in $[\boldsymbol{\mu}H]$ space will remain near the equilibrium surface as long as no resonance zone (instantaneous separatrix) is traversed. If the initial condition is also near a stationary platform equilibrium ($\boldsymbol{\omega} = \mathbf{0}$) and the torques are chosen so that the trajectory in $[\boldsymbol{\mu}]$ space satisfies the stationary platform condition ..., then the angular velocity of the platform will remain small throughout the maneuver.

Thus, in our applications, for the stability analysis to be strictly valid, all wheel torque trajectories must start on an equilibrium surface in $\boldsymbol{\mu}H$ space, must remain small, and should not cross a resonance zone (which might result in capture into unsteady motion).

Since the primary purpose of this report is to assess the utility and limitations of a sub-optimal wheel torque control law for real vehicles, and because the visualization

of equilibrium surfaces in μH space for a three wheel vehicle is difficult, stability of the various trajectories will in general not be addressed.

Stability issues aside, as we shall see in more detail in the examples in Chapter 4, violations of the small torque assumption also result in errors in the final vehicle states. Specifically, *any* movement along the stationary platform wheel momenta ellipsoid *must* violate the stationary platform condition in Eq. (3.2) because for there to be motion of the vehicle, no matter how small, ω cannot be zero. Thus, the angular momentum vector \mathbf{x} will move with respect to the platform during maneuvers, and we shall see that the character of this motion (large or small platform angular velocities) is dependent on the choice of the torque scaling parameter ϵ .

Two other basic assumptions for this analysis are that at the initial time the platform is stationary and at the completion of maneuvers, all torques are turned off such that the momentum wheels remain at the final angular velocities (no energy loss in wheels). In real applications, of course, a controller using state feedback may be necessary to stabilize the platform prior to beginning such a maneuver as well as to reduce final state errors, and there may be bearing or other losses in the wheels requiring small torques to maintain constant angular velocities after the maneuver.

3.4 Direct Rest-to-rest Trajectories

As mentioned previously, there are certainly applications for “large angle” spacecraft maneuvers that start and end with a stationary platform ($\tilde{\omega} \approx 0$ at t_o and t_f). This general class of maneuver is commonly referred to as *rest-to-rest*, and includes both the arbitrary intermediate state sub-class ($\tilde{\omega} \neq 0$, $t_o < t < t_f$) and the *stationary platform maneuver* sub-class for which platform angular rates are small throughout the maneuver. In this section, we will focus on a special case of the former sub-class, known as the *direct rest-to-rest* maneuver. The latter sub-class will be discussed in the next section of this chapter.

The direct rest-to-rest maneuver (hereafter referred to as the *direct trajectory*) is depicted in Fig. 3.13 in terms of the wheel momenta ellipsoid.

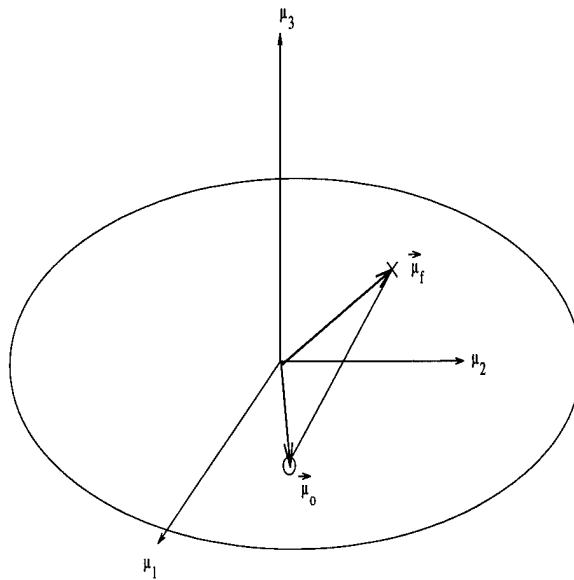


Figure 3.13 *Direct Trajectory on Wheel Momenta Ellipsoid*

It is apparent that while both the initial and final wheel momenta states satisfy the stationary platform criteria (are on the ellipsoid surface), the intermediate states do not, and we thus do *not* expect to have small platform angular velocities throughout the maneuver. As we shall see in later sections, violation of the stationary platform condition during these maneuvers also results in final state errors (in \mathbf{x}), so that even though the total angular momentum is constant (no external torques), we can strictly only use the

method outlined in section 3.1 to calculate the attitude of the vehicle at the initial and final times if the vehicle is totally stationary.

The wheel torque control law for this direct trajectory from μ_o to μ_f is

$$\dot{\mu} = \epsilon = \epsilon \frac{\mu_f - \mu_o}{|\mu_f - \mu_o|} \quad (3.15)$$

where ϵ is the small parameter discussed in section 3.3. Note that using this approach, ϵ is a positive constant.

Assuming $t_o = 0$, the final (non-dimensional) time for such a maneuver given initial and final rotor momenta is found to be

$$t_f = \frac{|\mu_f - \mu_o|}{\epsilon} \quad (3.16)$$

Using Eq. (2.27), the dimensional time is easily calculated and is given by

$$\tilde{t}_f = \left(\frac{\tilde{I}_c}{\tilde{h}_o} \right) \frac{|\mu_f - \mu_o|}{\epsilon} \quad (3.17)$$

By solving Eq. (3.16) for ϵ and substituting in for \tilde{t}_f from Eq. (3.17), we can find the value of the small parameter ϵ required to accomplish the maneuver in time \tilde{t}_f

$$\epsilon = \left(\frac{\tilde{I}_c}{\tilde{h}_o} \right) \frac{|\mu_f - \mu_o|}{\tilde{t}_f} \quad (3.18)$$

Note that ϵ is directly proportional to \tilde{I}_c and $|\mu_f - \mu_o|$, while it is inversely proportional to \tilde{h}_o and \tilde{t}_f . Thus, we would expect larger required torques for larger vehicle inertias and longer torque trajectories, while increasing wheel momenta and final times will result in smaller required torques.

A plot of ϵ vs. t_f for the Hubble Space Telescope, with $\tilde{I}_c \approx 1.8 \times 10^5 \text{ kg m}^2$, using wheels $\mathcal{W}_1 - \mathcal{W}_3$ with $\mu_o = [1 \ 0 \ 0]$, $\mu_f = [0 \ 1 \ 0]$ for both $\tilde{h}_o = 100$ and $200 \text{ kg m}^2/\text{s}$, is shown in Fig. 3.14.

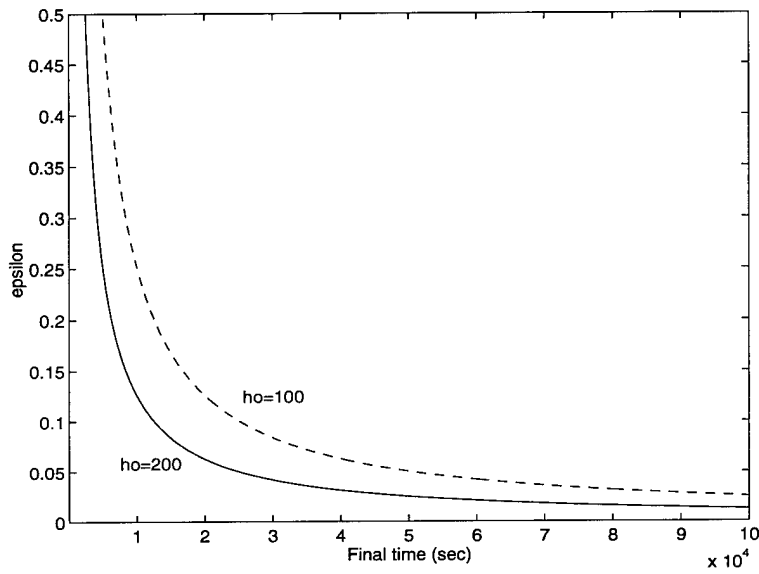


Figure 3.14 *Direct Trajectory - Small Torque Parameter ϵ vs. \tilde{t}_f for varying \tilde{h}_o*

As we would expect, reducing \tilde{I}_c/\tilde{h}_o by 1/2, either by doubling \tilde{h}_o or halving \tilde{I}_c results in required torques for a given \tilde{t}_f being reduced by a factor of 2 as well. Recalling from our earlier discussion about allowable torques and the resulting state errors during and at the end of maneuvers, we see that there is a significant trade-off between final time and wheel torques. This trade-off will be discussed in more detail for the individual vehicles of interest in Chapter 4.

3.5 Sub-optimal Trajectories on the Wheel Momenta Ellipsoid

While the direct trajectories discussed in the previous section are certainly easy to calculate and simple to implement, it will become apparent from examples in Chapter 4 that the relatively large body angular rates that result during the maneuver for large wheel torques could prove harmful to flexible and/or sensitive components on board. We therefore wish to derive a wheel torque control law that not only reorients the vehicle from one stationary orientation to another, but that maintains small angular velocities of the platform throughout the maneuver. One could consider such a maneuver to be "smooth".

Large angle reorientations for spacecraft using momentum wheels are often accomplished via "Euler-axis" or "eigen-axis" rotations, which are finite angle rotations about a body fixed axis of rotation [11:10-11]. While simple in concept, calculations to determine such maneuvers are somewhat computationally intense, requiring the solution to an eigenvalue problem. Today, such calculations are typically performed by high speed ground segment computers based on down-linked telemetry, then sent to the relatively "dumb" satellite via the command up-link for immediate or delayed execution. However, the logical and inevitable progression toward greater spacecraft autonomy (driven by lowered operations costs) dictates on-board attitude determination as well as large angle maneuvering capability. Also, although these maneuvers can be accomplished rather quickly, they can also result in undesirably large body angular velocities.

The sub-optimal control law discussed herein is a "smooth" maneuver in the sense that it reduces unwanted body motions, and requires only matrix multiplications and transpose operations to perform (with the exception of final time calculations which need not be done on-board).

Recalling the discussion in Section 3.2, Hall [8] showed that for a spacecraft using two momentum wheels, if a wheel torque trajectory was calculated that stayed on a stable surface in the μH space, used small torques ($\epsilon \ll 1$), and was tangent to the stationary platform wheel momenta ellipse, a "smooth" reorientation could be performed with only small induced body angular velocities.

Hall derived this torque control law by differentiating the wheel momenta ellipsoid Eq. (3.4) with respect to time, yielding

$$\dot{\boldsymbol{\mu}}^T \mathbf{A}^T \mathbf{A} \boldsymbol{\mu} = 0 \quad (3.19)$$

Since $\mathbf{A}^T \mathbf{A}$ is positive definite and we are not interested in the trivial solution $\boldsymbol{\mu} = 0$, this requires that $\dot{\boldsymbol{\mu}}^T$ lie in the left nullspace of $\mathbf{A}^T \mathbf{A} \boldsymbol{\mu}$. In the two wheel case, it is thus evident that the wheel torque law is given by

$$\dot{\boldsymbol{\mu}} = \epsilon \begin{pmatrix} \hat{\mathbf{a}}_1^T \hat{\mathbf{a}}_2 & \hat{\mathbf{a}}_2^T \hat{\mathbf{a}}_2 \\ -\hat{\mathbf{a}}_1^T \hat{\mathbf{a}}_1 & -\hat{\mathbf{a}}_1^T \hat{\mathbf{a}}_2 \end{pmatrix} \boldsymbol{\mu} \quad (3.20)$$

which is easily seen as a slowly moving trajectory along the tangent to the wheel momenta ellipse in two dimensions. Note as well that $\hat{\mathbf{a}}_1^T \hat{\mathbf{a}}_1 = 1$ and $\hat{\mathbf{a}}_2^T \hat{\mathbf{a}}_2 = 1$.

To extend this simple result to three wheels, for which the wheel momenta ellipsoid is three dimensional, we define a new orthonormal frame \mathcal{F}_ν with the same origin as \mathcal{F}_μ , but rotated such that the ν_1 axis is co-linear with $\boldsymbol{\mu}_o$ and both $\boldsymbol{\mu}_o$ and $\boldsymbol{\mu}_f$ lie in the $\nu_1 - \nu_2$ plane. The intersection of the $\nu_1 - \nu_2$ plane with the surface of the wheel momenta ellipsoid is thus a wheel torque trajectory that will transfer momentum from $\boldsymbol{\mu}_o$ to $\boldsymbol{\mu}_f$ (See Fig. 3.15). Note that strictly there are two trajectories between these points, depending on the sign of ϵ chosen (the “long” and “short” trajectories). We will be primarily concerned with the “short” trajectory since we expect this to require less maneuvering time. For the sub-optimal control law derived below, this corresponds to negative ϵ .

For a vehicle with orthogonal wheels (wheel momenta ellipsoid is a sphere), this is seen to be the “great circle” trajectory, and is the minimum distance (in $\boldsymbol{\mu}$ space) between $\boldsymbol{\mu}_o$ and $\boldsymbol{\mu}_f$ on the sphere. For vehicles whose wheels are more co-planar or co-linear, this path obviously is no longer minimum distance, but is a close approximation. In an extreme case of the ellipsoid becoming quite long and thin (see Fig. 3.6), the minimum distance trajectory would best be approximated by the ellipse formed by taking a cross-section through $\boldsymbol{\mu}_o$, $\boldsymbol{\mu}_f$, and their reflections across the longest principal axis of the ellipsoid. However, since spacecraft typically have pyramidal wheel arrangements,

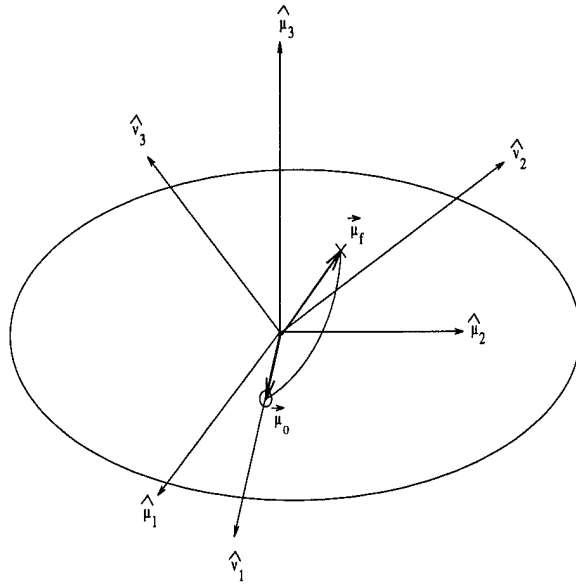


Figure 3.15 *Sub-optimal Trajectory on Wheel Momenta Ellipsoid*

the wheel momenta ellipsoids are more spherical than cylindrical, and the simpler result obtained below with this assumption should be adequate.

Finding the rotation matrix $\mathbf{T}_{\mu\nu}$ relating \mathcal{F}_ν to \mathcal{F}_μ is straightforward. The basis vectors for \mathcal{F}_ν expressed in \mathcal{F}_μ are

$$\hat{\nu}_1 = \boldsymbol{\mu}_o / |\boldsymbol{\mu}_o| \quad (3.21)$$

$$\hat{\nu}_3 = (\boldsymbol{\mu}_o \times \boldsymbol{\mu}_f) / |\boldsymbol{\mu}_o \times \boldsymbol{\mu}_f| \quad (3.22)$$

$$\hat{\nu}_2 = \hat{\nu}_3 \times \hat{\nu}_1 \quad (3.23)$$

so that

$$\mathbf{T}_{\mu\nu} = \begin{pmatrix} \vdots & \vdots & \vdots \\ \hat{\nu}_1 & \hat{\nu}_2 & \hat{\nu}_3 \\ \vdots & \vdots & \vdots \end{pmatrix} \quad (3.24)$$

This orthonormal matrix allows us to transform a vector $\boldsymbol{\nu}$ expressed in \mathcal{F}_ν to its equivalent form $\boldsymbol{\mu}$ in \mathcal{F}_μ through the relationship

$$\boldsymbol{\mu} = \mathbf{T}_{\mu\nu} \boldsymbol{\nu} \quad (3.25)$$

Substituting from this equation for $\boldsymbol{\mu}$ in Eq. (3.4) yields the stationary platform wheel momentum ellipsoid expressed in \mathcal{F}_ν

$$\boldsymbol{\nu}^T \mathbf{T}_{\mu\nu}^T \mathbf{A}^T \mathbf{A} \mathbf{T}_{\mu\nu} \boldsymbol{\nu} = 1 \quad (3.26)$$

Looking at the trajectory with respect to the new frame \mathcal{F}_ν , we note that the $\hat{\boldsymbol{\nu}}_3$ component of $\boldsymbol{\nu} = (\nu_1 \ \nu_2 \ \nu_3)$ along the trajectory is zero, so that Eq. (3.26) in expanded form now reduces to

$$\begin{pmatrix} \nu_1 & \nu_2 \end{pmatrix} \begin{pmatrix} \boldsymbol{\alpha}_1^T \boldsymbol{\alpha}_1 & \boldsymbol{\alpha}_1^T \boldsymbol{\alpha}_2 \\ \boldsymbol{\alpha}_1^T \boldsymbol{\alpha}_2 & \boldsymbol{\alpha}_2^T \boldsymbol{\alpha}_2 \end{pmatrix} \begin{pmatrix} \nu_1 \\ \nu_2 \end{pmatrix} = 1 \quad (3.27)$$

where $\boldsymbol{\alpha}_1$ and $\boldsymbol{\alpha}_2$ are the first two columns of $\mathbf{A} \mathbf{T}_{\mu\nu}$. Note that since $\mathbf{T}_{\mu\nu}$ is post-multiplying \mathbf{A} , the diagonal elements $\boldsymbol{\alpha}_1^T \boldsymbol{\alpha}_1$ and $\boldsymbol{\alpha}_2^T \boldsymbol{\alpha}_2$ are not unity in this case.

Equation (3.27) is the same form as the stationary platform wheel momenta ellipsoid Eq. (3.4) for the case of two wheels, expressed in \mathcal{F}_ν . Thus, the same control law as Eq. (3.20) applies to the three wheel case, with $\dot{\nu}_3 = 0$

$$\dot{\boldsymbol{\nu}} = \epsilon \begin{pmatrix} \boldsymbol{\alpha}_1^T \boldsymbol{\alpha}_2 & \boldsymbol{\alpha}_2^T \boldsymbol{\alpha}_2 & 0 \\ -\boldsymbol{\alpha}_1^T \boldsymbol{\alpha}_1 & -\boldsymbol{\alpha}_1^T \boldsymbol{\alpha}_2 & 0 \\ 0 & 0 & 0 \end{pmatrix} \boldsymbol{\nu} = \epsilon \mathbf{B} \boldsymbol{\nu} \quad (3.28)$$

Now, by solving Eq. (3.25) for $\boldsymbol{\nu}$ and recognizing that $\mathbf{T}_{\mu\nu}^{-1} = \mathbf{T}_{\mu\nu}^T$, we can substitute into Eq. (3.28) to obtain

$$\mathbf{T}_{\mu\nu}^T \dot{\boldsymbol{\mu}} = \epsilon \mathbf{B} \mathbf{T}_{\mu\nu}^T \boldsymbol{\mu} \quad (3.29)$$

or

$$\dot{\boldsymbol{\mu}} = \epsilon \mathbf{T}_{\mu\nu} \mathbf{B} \mathbf{T}_{\mu\nu}^T \boldsymbol{\mu} \quad (3.30)$$

which is the sub-optimal wheel torque control law for a vehicle using three momentum wheels. Use of this control law with "small" ϵ should result in a reorientation from an initial $\boldsymbol{\mu}_o$ to a final $\boldsymbol{\mu}_f$ with little induced platform motion.

The time required to accomplish a stationary platform maneuver is certainly of interest to us, as this will be a significant factor in assessing the utility of these control laws

for real applications. As with the direct trajectory, we assume $t_o = 0$ and that we are given initial and final wheel momenta $\boldsymbol{\mu}_o$ and $\boldsymbol{\mu}_f$.

We return to the wheel torque control law in the \mathcal{F}_ν frame, given in Eq. (3.28), eliminating the state $\boldsymbol{\nu}_3$ since it is zero and constant. This results in a system of two linear constant co-efficient equations. The solution (at time t_f) to this linear equation is

$$\boldsymbol{\nu}_f = e^{\mathbf{B}t_f} \boldsymbol{\nu}_o = \mathbf{V} e^{\boldsymbol{\Lambda}t_f} \mathbf{V}^{-1} \boldsymbol{\nu}_o \quad (3.31)$$

where the columns of \mathbf{V} are the eigenvectors of \mathbf{B} , $e^{\boldsymbol{\Lambda}t_f}$ is a diagonal matrix with diagonal elements $e^{\lambda_i t_f}$, and λ_i are the eigenvalues of \mathbf{B} . Putting \mathbf{B} into the form

$$\mathbf{B} = \begin{pmatrix} B_{11} & B_{12} \\ -B_{21} & -B_{11} \end{pmatrix} \quad (3.32)$$

allows us to see that the eigenvalues will be purely imaginary as long as $B_{12}B_{21} > B_{11}^2$. In the case where $\mathcal{F}_\nu = \mathcal{F}_\mu$, the off-diagonal elements are 1 and the diagonal elements are always less than 1 as long as the wheels are non-colinear. In the more general case, the elements B_{ij} are formed from inner products of the first two columns of $\mathbf{A}\mathbf{T}_{\mu\nu}$, where $\mathbf{T}_{\mu\nu}$ is orthonormal, and we find that in all the cases presented herein the eigenvalues are indeed imaginary.

Since the eigenvalues of \mathbf{B} are purely imaginary ($\pm j\sqrt{B_{12}B_{21} - B_{11}^2}$), we note that $e^{\mathbf{B}t_f}$ is a rotation matrix [21:212]. If we define $\phi = \epsilon(\sqrt{B_{12}B_{21} - B_{11}^2})t_f$, and recognize that by definition of \mathcal{F}_ν that $\boldsymbol{\nu}_o = (1 \ 0)^T$, then Eq. (3.31) can be written

$$\mathbf{V}^{-1} \boldsymbol{\nu}_f = \begin{pmatrix} \cos \phi & \sin \phi \\ -\sin \phi & \cos \phi \end{pmatrix} \mathbf{V}^{-1} \begin{pmatrix} 1 \\ 0 \end{pmatrix} \quad (3.33)$$

Denoting the elements of the 2×2 matrix \mathbf{V}^{-1} by \mathcal{V}_{ij} , and the matrix resulting from $\mathbf{V}^{-1} \boldsymbol{\nu}_f$ by $\mathbf{v} = (v_1 \ v_2)^T$, Eq. (3.33) can be reduced through some manipulation to the form

$$\begin{pmatrix} \cos \phi \\ \sin \phi \end{pmatrix} = \frac{1}{\mathcal{V}_{11}^2 + \mathcal{V}_{21}^2} \begin{pmatrix} \mathcal{V}_{11}v_1 + \mathcal{V}_{21}v_2 \\ \mathcal{V}_{21}v_1 + \mathcal{V}_{11}v_2 \end{pmatrix} \quad (3.34)$$

which can be solved for ϕ to obtain

$$\phi = \tan^{-1} \left(\frac{\mathcal{V}_{21}v_1 + \mathcal{V}_{11}v_2}{\mathcal{V}_{11}v_1 + \mathcal{V}_{21}v_2} \right) \quad (3.35)$$

Recalling the definition of ϕ above and the relationship between t and \tilde{t} from Eq.(2.27), this can be solved for the dimensional final time

$$\tilde{t}_f = \left(\frac{\tilde{I}_c}{\tilde{h}_o} \right) \left(\frac{1}{\epsilon \sqrt{B_{12}B_{21} - B_{11}^2}} \right) \tan^{-1} \left(\frac{\mathcal{V}_{21}v_1 + \mathcal{V}_{11}v_2}{\mathcal{V}_{11}v_1 + \mathcal{V}_{21}v_2} \right) \quad (3.36)$$

The magnitude of the small torque parameter ϵ vs. \tilde{t}_f is obviously found directly from this equation, and is provided here to motivate discussion.

$$\epsilon = \left(\frac{\tilde{I}_c}{\tilde{h}_o} \right) \left(\frac{1}{\tilde{t}_f \sqrt{B_{12}B_{21} - B_{11}^2}} \right) \tan^{-1} \left(\frac{\mathcal{V}_{21}v_1 + \mathcal{V}_{11}v_2}{\mathcal{V}_{11}v_1 + \mathcal{V}_{21}v_2} \right) \quad (3.37)$$

Using this approach, to obtain positive final time values, the small parameter ϵ must be negative.

Fig. 3.16 is a plot of $|\epsilon|$ vs. t_f for the Hubble Space Telescope using the sub-optimal control law. The boundary conditions and vehicle parameters are the same as for the direct maneuver depicted in Fig. 3.14, with $\tilde{I}_c \approx 1.8 \times 10^5 \text{ kg m}^2$, using wheels $\mathcal{W}_1 - \mathcal{W}_3$ with $\boldsymbol{\mu}_o = [1 \ 0 \ 0]$, $\boldsymbol{\mu}_f = [0 \ 1 \ 0]$ for both $\tilde{h}_o = 100$ and $200 \text{ kg m}^2/\text{s}$. This corresponds to a 90° maneuver, so that for $\epsilon = 0.1$, the spacecraft rotates at approximately $0.009^\circ/\text{s}$.

As with the direct trajectory, we note a significant trade-off between final time and torque magnitude, and again see that reducing \tilde{I}_c/\tilde{h}_o and/or increasing \tilde{t}_f reduces the required torques for this maneuver.

It might be tempting to conclude that since the direct trajectories have shorter path lengths in \mathcal{F}_μ than sub-optimal trajectories for identical initial and final conditions, the maneuver times would also be less. However, as Figs. 3.17 and 3.18 show, this is not always the case. Both figures are for the Hubble Space Telescope using wheels $\mathcal{W}_1 - \mathcal{W}_3$, with equal total angular momentum and initial conditions ($\boldsymbol{\mu}_o = [1 \ 0 \ 0]^T$). However, whereas the final condition in the first case in $\boldsymbol{\mu}_f = [0 \ 1 \ 0]^T$, in the second it is $\boldsymbol{\mu}_f \approx [0.715 \ -1.086 \ -0.074]^T$.

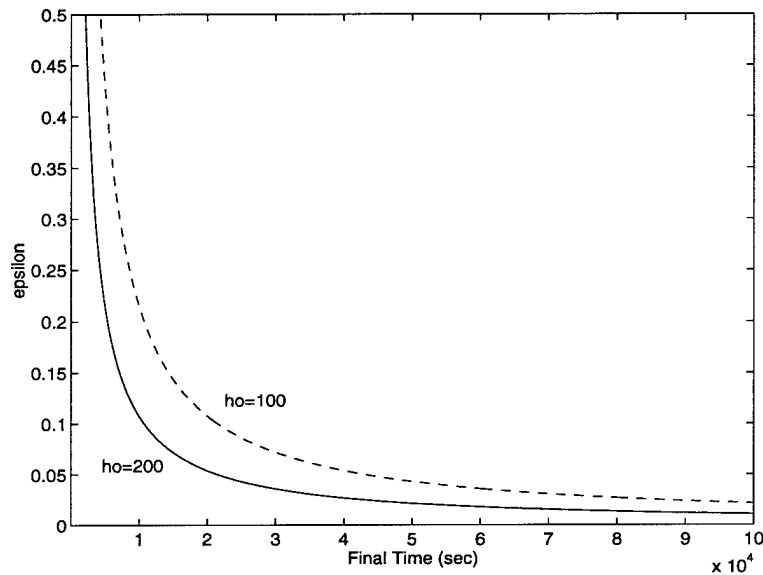


Figure 3.16 *Sub-optimal Trajectory - Small Torque Parameter ϵ vs. \tilde{t}_f for varying \tilde{h}_o*

The explanation for this lies in the fact that the average wheel momenta for sub-optimal trajectories are generally larger than for direct trajectories, and can thus be traversed more quickly. As demonstrated, however, the relationship between ϵ , \tilde{t}_f , and the control trajectory depends on the momentum wheels used and the boundary conditions.

Now that we have developed the wheel torque control laws for both direct and sub-optimal trajectories, let us run some example simulations for both the GPS Block IIR and Hubble Space Telescope vehicles, in an environment free from external perturbing torques. This will allow us to compare both types of maneuvers, and particularly to assess the utility of the sub-optimal control law for “real” vehicles. Then, in Chapter 5, external perturbing torques will be introduced to allow assessment of the sub-optimal control law for “real” vehicles in a more “realistic” environment.

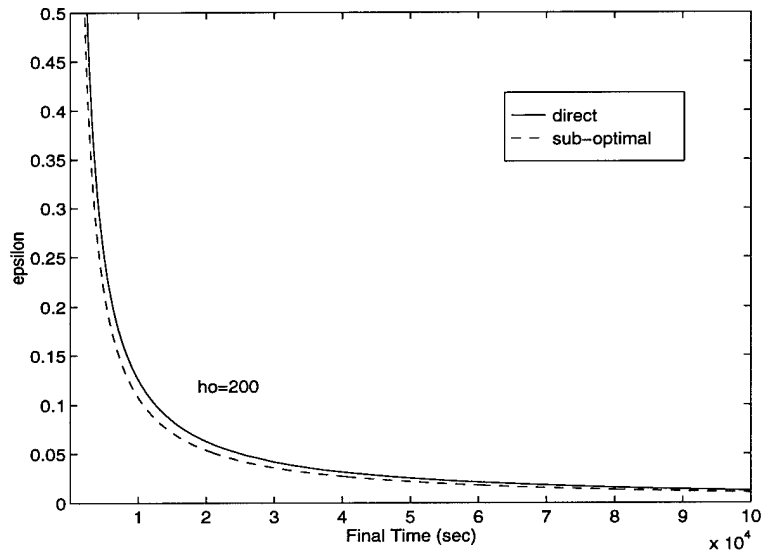


Figure 3.17 Case 1 - Comparison of ϵ vs. \tilde{t}_f for Direct and Sub-optimal Trajectories

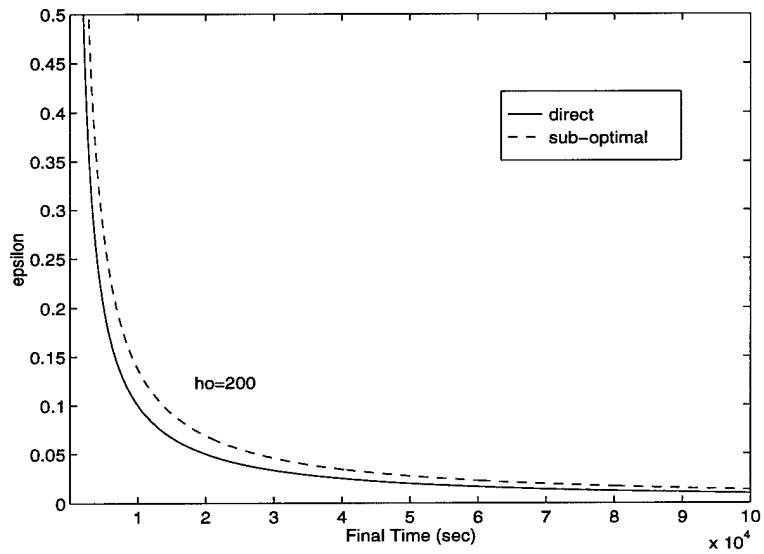


Figure 3.18 Case 2 - Comparison of ϵ vs. \tilde{t}_f for Direct and Sub-optimal Trajectories

IV. Unperturbed Maneuvers

In this chapter, specific examples of maneuvers using the GPS Block IIR and Hubble Space Telescope vehicles will be presented. These two vehicles were chosen because they both employ at least three momentum wheels for attitude control, but in varying degrees. While momentum wheels are used only to offset small perturbative torques on the GPS Block IIR vehicle, they are the primary attitude control mechanism for the Hubble Space Telescope. The momentum storage capacities of the vehicles' momentum wheels are thus quite different, and the vehicles can be seen to represent two ends of the spectrum for momentum storage device use.

Appendix D provides a functional block diagram of the simulation computer program used to generate the results in this section. The main program (`rotor.m.m`) first calls the data definition file (`dat_gps.m`, `dat_hub.m`) to load vehicle physical parameters, orbital parameters, and simulation control parameters. Next, after calculating the appropriate wheel torque control law for the maneuver (direct or sub-optimal), the program sends the appropriate equations of motion (with or without perturbing forces) to the integration subroutine (`ode45.m`). After integration is complete, important data is output in either text or graphical format.

The simulation program has the capability to output more than 10 different data plots, in both dimensional and non-dimensional values. However, the most important plots that will be used in our analysis are the following: Torque trajectory relative to stationary platform wheel momenta ellipsoid, torque trajectory relative to spacecraft total momentum sphere, momentum wheel angular velocities vs. time, spacecraft angular velocities vs. time, and three dimensional spacecraft attitude plots.

To minimize the number of examples that will be presented, let us first state the objectives we wish to meet in the following two sections. For GPS, we will first perform a maneuver from a specific stationary attitude to another (or close to it, depending upon final state errors), using both the direct control law and sub-optimal control law, with identical ϵ and \tilde{h}_o , to show the difference in final state error and intermediate angular velocities for each approach. Next, we will calculate the maximum allowable \tilde{h}_o for each

vehicle, then perform the same maneuver using the sub-optimal control law several times, varying the magnitude of ϵ , to identify what value of ϵ is reasonable in terms of final state errors, maneuver time, and intermediate angular velocities.

4.1 GPS Block IIR Examples

As mentioned previously, the GPS Block IIR vehicle uses expendable fuel thrusters for large angle maneuvers, and employs four *reaction* wheels, arranged in a pyramid fashion, to offset small perturbative torques acting on the vehicle. The wheels are augmented by a magnetic torquing system which is used for momentum dumping. The vehicle physical parameters are detailed in Appendix B. The difference in application between reaction wheels and momentum wheels (nominal angular rates, commandable torques) will be ignored in the following simulations, to better allow comparison between GPS and Hubble Space Telescope.

We first note that the maximum momentum a single wheel can generate is $\tilde{h}_{max} \approx \pm 8 \text{ kg m}^2/\text{s}$. Thus, to allow arbitrary reorientations, \tilde{h}_o should be set as less than $8 \text{ kg m}^2/\text{s}$ in the simulations. The ratio of wheel inertia to maximum principal inertia of the vehicle is $\tilde{I}_s/\tilde{I}_{max} \approx 0.0046$. Although not derived herein, it can be shown that if we assume a single wheel is attempting to absorb the angular momentum for a pure (stable) spin about the major axis of the vehicle, and that the wheel is parallel to the major axis, the maximum initial rate of the vehicle such that the wheel can achieve a stationary platform is approximately $4.014 \times 10^{-3} \text{ rad/s}$. Similar analysis for a minor axis spin results in a maximum angular rate of approximately $1.030 \times 10^{-2} \text{ rad/s}$. While this analysis is based on several simplifying assumptions, it does allow us to see that only small vehicle angular velocities can be offset using the momentum wheels, which requires that final state errors be within or below this range to be controllable using the momentum wheels alone.

To be realistic, we must also be concerned about the magnitude of the torques used, since in actual applications we cannot exceed the maximum nor go below the minimum commandable values. Using Eq. (2.26), noting the values for minimum and maximum commandable torques from Appendix B, the known value of $\tilde{I}_c = 4.5266 \times 10^3 \text{ kg m}^2$, and

$\tilde{h}_o = 5 \text{ kg m}^2/\text{s}$ results in

$$\epsilon_{max} = \frac{\tilde{g}_{max} \tilde{I}_c}{\tilde{h}_o^2} \approx 12.86 \quad (4.1)$$

$$\epsilon_{min} = \frac{\tilde{g}_{min} \tilde{I}_c}{\tilde{h}_o^2} \approx 0.05 \quad (4.2)$$

The purpose of the following simulations is both to compare direct and sub-optimal control laws for attitude maneuvers, as well as demonstrate the growth in final state errors with increasing torque scaling parameter ϵ .

Discussion and comparison of the simulation results for both GPS Block IIR and the Hubble Space Telescope is deferred to section 4.3.

GPS Example 1 - Direct vs. Sub-optimal Trajectories

As our first example, we will compare direct and sub-optimal trajectory maneuver times, angular velocities, and final state errors for a combined 45° rotation about the $\hat{\mathbf{b}}_3$ and $\hat{\mathbf{b}}_1$ axis with \mathcal{W}_1 initially containing all the angular momentum, using wheels $\mathcal{W}_1, \mathcal{W}_2, \mathcal{W}_4$. Table 4.1 summarizes the simulation parameters. The results are summarized in Figs. 4.1-4.12 and Table 4.2.

Table 4.1 GPS Example 1 - Direct vs. Sub-optimal Simulation Parameters

parameter	value
\mathbf{A}	$(\mathbf{a}_1 \quad \mathbf{a}_2 \quad \mathbf{a}_4)$
\tilde{h}_o	$5 \text{ kg m}^2/\text{s}$
ϵ	0.01
ϕ_o, θ_o, ψ_o	0, 0, 0
ϕ_f, θ_f, ψ_f	$45^\circ, 45^\circ, 0$
$\boldsymbol{\mu}_o$	$(1 \quad 0 \quad 0)$

Table 4.2 GPS Example 1 - Direct vs. Sub-optimal Simulation Results

result	Direct	Sub-optimal
\tilde{t}_f	24 hr 22 min	28 hr 38 min
$ \tilde{\omega} _{max}$	$3.461 \times 10^{-4} \text{ rad/s}$	$1.895 \times 10^{-5} \text{ rad/s}$
$ \tilde{\omega}_s _{max}$	590.3 rad/s	613.2 rad/s
$ \tilde{\omega}(\tilde{t}_f) _{max}$	$2.788 \times 10^{-6} \text{ rad/s}$	$1.526 \times 10^{-5} \text{ rad/s}$
ϕ_f, θ_f, ψ_f	$-53.30, 119.48, -5.133^\circ$	$48.35, 44.04, -2.27^\circ$

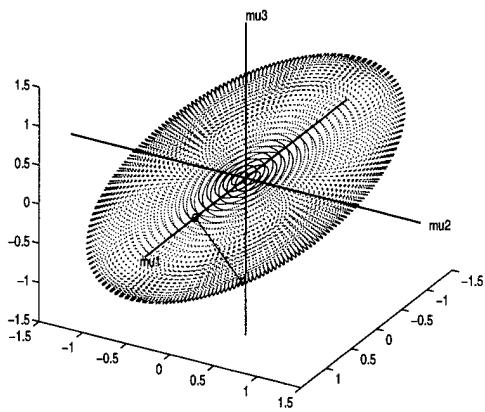


Figure 4.1 *GPS Example 1 - (Direct)
Torque Trajectory on Wheel
Momenta Ellipsoid*

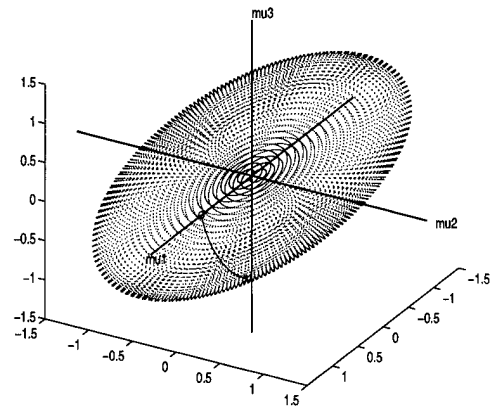


Figure 4.2 *GPS Example 1 - (Sub-opt)
Torque Trajectory on Wheel
Momenta Ellipsoid*

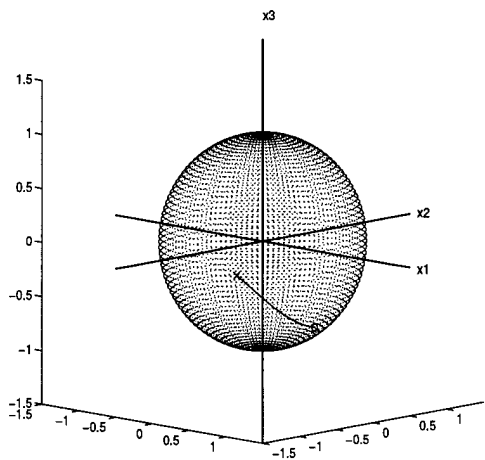


Figure 4.3 *GPS Example 1 - (Direct)
Torque Trajectory on Total
Momentum Sphere*

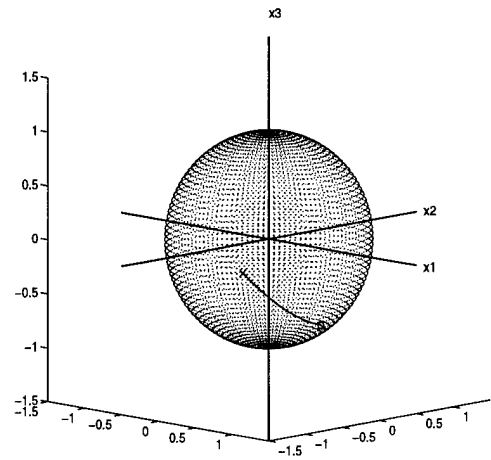


Figure 4.4 *GPS Example 1 - (Sub-opt)
Torque Trajectory on Total
Momentum Sphere*

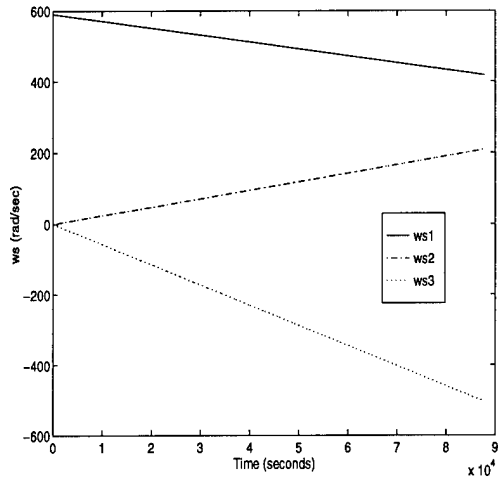


Figure 4.5 *GPS Example 1 - (Direct) Wheel Angular Velocities*

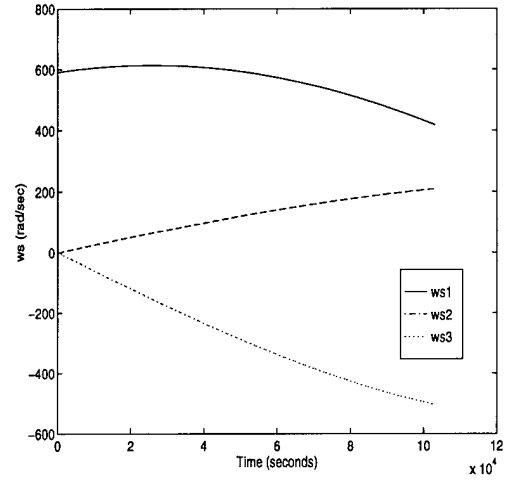


Figure 4.6 *GPS Example 1 - (Sub-opt) Wheel Angular Velocities*

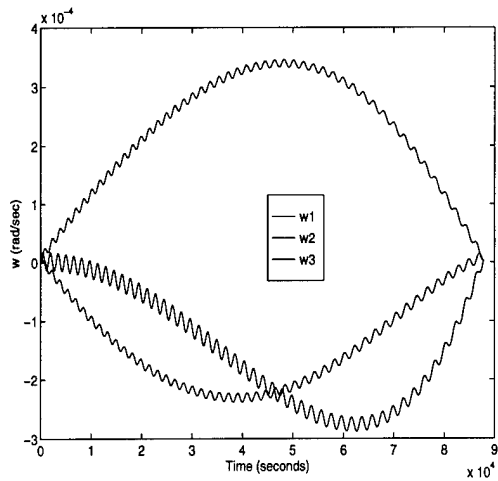


Figure 4.7 *GPS Example 1 - (Direct) Vehicle Angular Velocities*

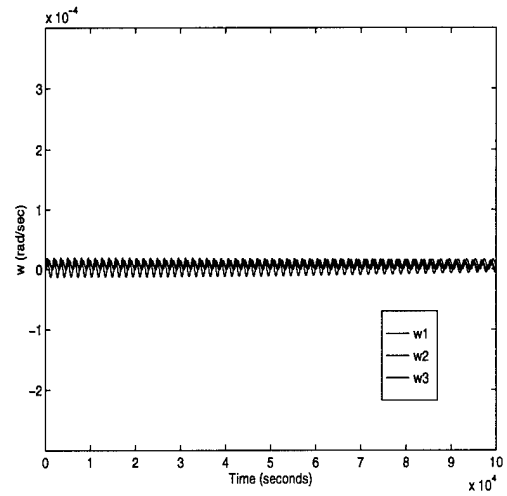


Figure 4.8 *GPS Example 1 - (Sub-opt) Vehicle Angular Velocities*

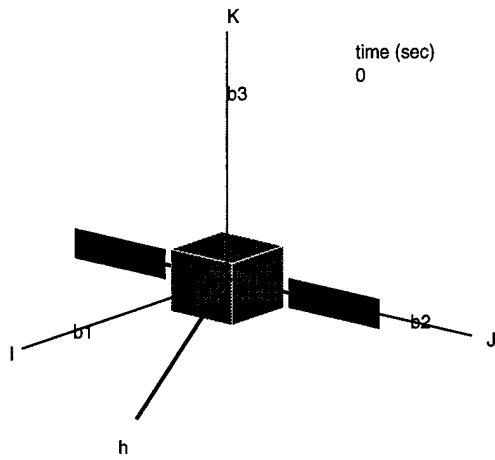


Figure 4.9 *GPS Example 1 - Initial Attitude*

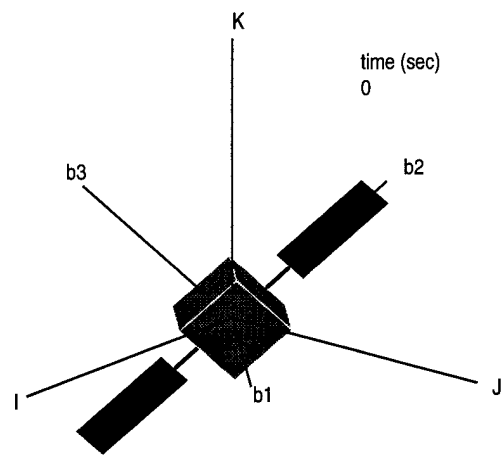


Figure 4.10 *GPS Example 1 - Desired Final Attitude*

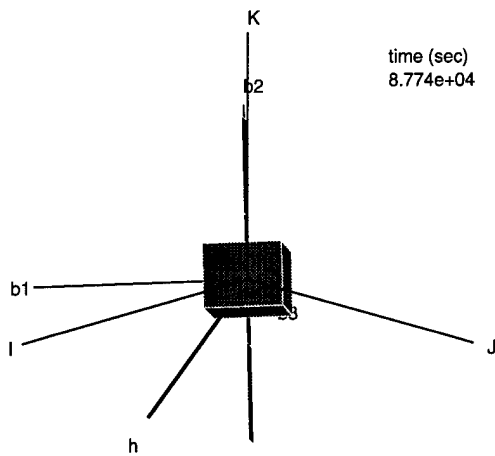


Figure 4.11 *GPS Example 1 - (Direct) Final Attitude*

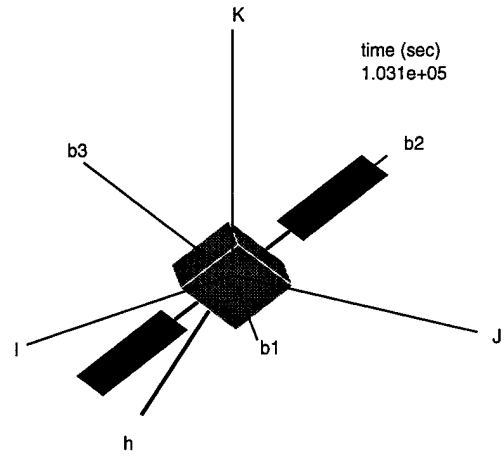


Figure 4.12 *GPS Example 1 - (Sub-opt) Final Attitude*

GPS Example 2 - Sub-optimal Trajectory

In the second example, we will now address the sub-optimal trajectory only, this time increasing ϵ to 0.05. The other simulation parameters are identical to the first example. Table 4.3 summarizes the simulation parameters. The results are summarized in Figs. 4.13-4.16 and Table 4.4.

Table 4.3 GPS Example 2 - Sub-optimal Simulation Parameters

parameter	value
A	(a₁ a₂ a₄)
\tilde{h}_o	$5 \text{ kg m}^2/\text{s}$
ϵ	0.05
ϕ_o, θ_o, ψ_o	0, 0, 0
ϕ_f, θ_f, ψ_f	$45^\circ, 45^\circ, 0$
μ_o	(1 0 0)

Table 4.4 GPS Example 2 - Sub-optimal Simulation Results

result	Sub-optimal
\tilde{t}_f	$5 \text{ hr } 43 \text{ min}$
$ \tilde{\omega} _{max}$	$9.482 \times 10^{-5} \text{ rad/s}$
$ \tilde{\omega}_s _{max}$	613.2 rad/s
$ \tilde{\omega}(\tilde{t}_f) _{max}$	$7.172 \times 10^{-5} \text{ rad/s}$
ϕ_f, θ_f, ψ_f	$49.12, 43.96, -3.84^\circ$

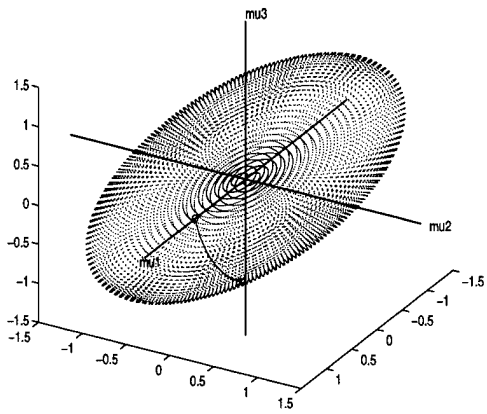


Figure 4.13 *GPS Example 2 - (Sub-opt) Torque Trajectory on Wheel Momenta Ellipsoid*

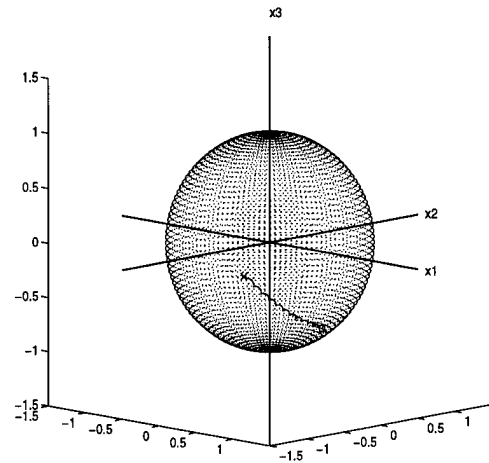


Figure 4.14 *GPS Example 2 - (Sub-opt) Torque Trajectory on Total Momentum Sphere*

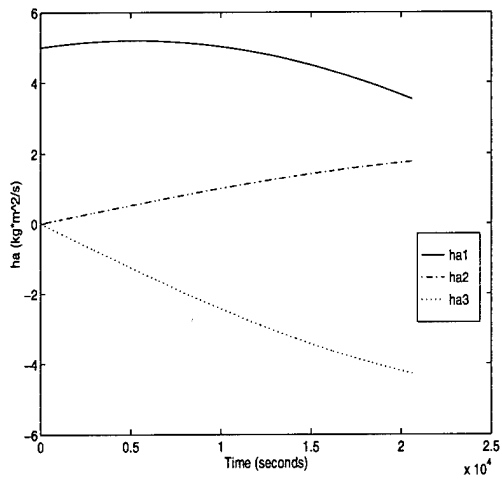


Figure 4.15 *GPS Example 2 - (Sub-opt) Wheel Angular Velocities*

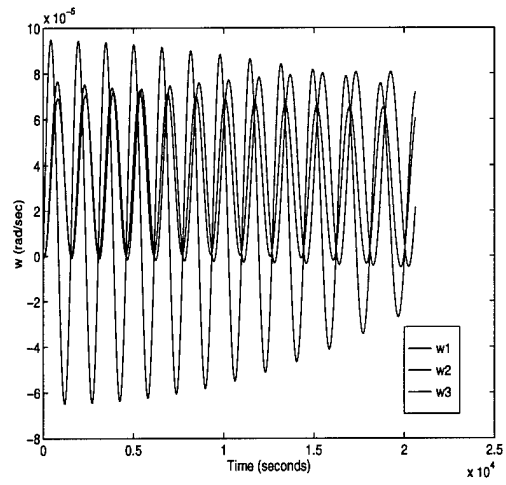


Figure 4.16 *GPS Example 2 - (Sub-opt) Vehicle Angular Velocities*

GPS Example 3 - Sub-optimal Trajectory

In the last example for GPS Blk IIR, we again address the sub-optimal trajectory only, this time increasing ϵ to 0.10. The other simulation parameters are identical to the first two examples. Table 4.5 summarizes the simulation parameters. The results are summarized in Figs. 4.17-4.20 and Table 4.6.

Table 4.5 GPS Example 3 - Sub-optimal Simulation Parameters

parameter	value
\mathbf{A}	$(\mathbf{a}_1 \ \mathbf{a}_2 \ \mathbf{a}_4)$
\tilde{h}_o	$5 \text{ kg m}^2/\text{s}$
ϵ	0.10
ϕ_o, θ_o, ψ_o	0, 0, 0
ϕ_f, θ_f, ψ_f	$45^\circ, 45^\circ, 0$
μ_o	(1 0 0)

Table 4.6 GPS Example 3 - Sub-optimal Simulation Results

result	Sub-optimal
t_f	$2 \text{ hr } 52 \text{ min}$
$ \tilde{\omega} _{max}$	$1.897 \times 10^{-4} \text{ rad/s}$
$ \tilde{\omega}_s _{max}$	613.2 rad/s
$ \tilde{\omega}(t_f) _{max}$	$7.999 \times 10^{-5} \text{ rad/s}$
ϕ_f, θ_f, ψ_f	$48.58, 43.34, -3.64^\circ$

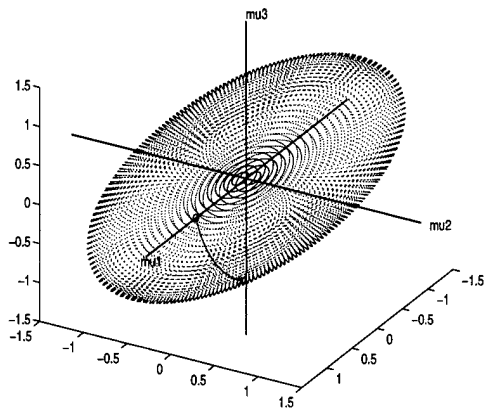


Figure 4.17 *GPS Example 3 - (Sub-opt) Torque Trajectory on Wheel Momenta Ellipsoid*

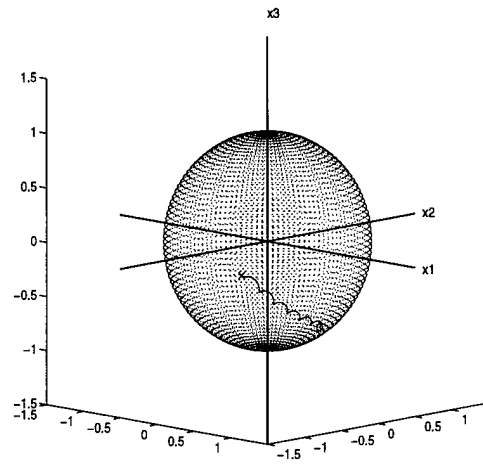


Figure 4.18 *GPS Example 3 - (Sub-opt) Torque Trajectory on Total Momentum Sphere*

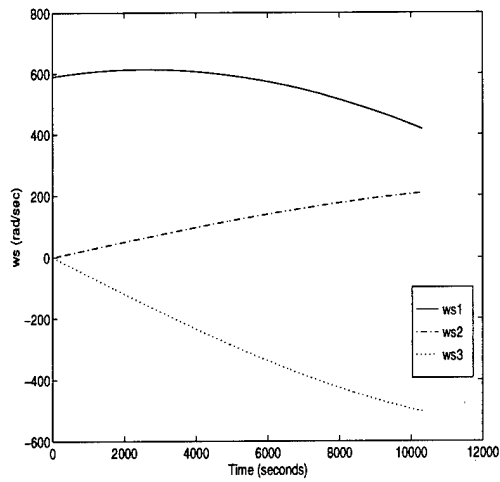


Figure 4.19 *GPS Example 3 - (Sub-opt) Wheel Angular Velocities*

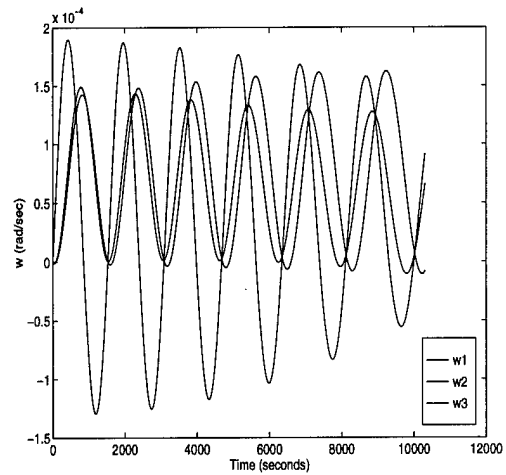


Figure 4.20 *GPS Example 3 - (Sub-opt) Vehicle Angular Velocities*

4.2 Hubble Space Telescope Examples

Unlike GPS, the Hubble Space Telescope uses momentum wheels exclusively for attitude control, both for large angle maneuvers and fine pointing control. Although data on the wheel inertias and angular rates were available, their orientation within the vehicle was not. Thus, the same arrangement as for GPS Block IIR was assumed for simplicity (see Appendix C). A magnetic torquing system is used for momentum dumping [2].

The Hubble pointing control system is currently able to slew the vehicle through a 90° reorientation using an eigen-axis maneuvering scheme in approximately 18 minutes [2], with 0.01 arc-second pointing accuracy. It will thus be of interest to compare the sub-optimal control results to these values.

The maximum momentum a single wheel can generate is $\tilde{h}_{max} \approx \pm 263.4 \text{ kg m}^2/\text{s}$. While this is obviously much greater on an absolute scale, the ratio of wheel inertia to maximum principal inertia of the vehicle is actually smaller than for GPS Block IIR at $\tilde{I}_s/\tilde{I}_{max} \approx 0.0033$. To allow arbitrary reorientations, \tilde{h}_o should be set somewhat less than $263.4 \text{ kg m}^2/\text{s}$ in the simulations. In all the examples below, \tilde{h}_o is set at $200 \text{ kg m}^2/\text{s}$. As we shall see in Example 3, due to the wheels chosen, this results in there being small regions of the wheel momenta ellipsoid that are unachievable, resulting in excessively high wheel speeds for trajectories that traverse these regions. The unachievable regions are only shown in the figures for Example 3, but they are present for Examples 1 and 2 as well.

Although not derived explicitly, it can be shown that if we assume a single wheel is attempting to absorb the angular momentum for a pure (stable) spin about the major axis of the vehicle, and that the wheel is parallel to the major axis, the maximum initial rate of the vehicle such that the wheel can achieve a stationary platform is approximately $3.299 \times 10^{-3} \text{ rad/s}$. Similar analysis for a minor axis spin results in a maximum angular rate of approximately $1.215 \times 10^{-2} \text{ rad/s}$. While this analysis is based on several simplifying assumptions, it does allow us to see that only small vehicle angular velocities can be offset using the momentum wheels, which requires that final state errors be within or below this range to be controllable using the momentum wheels alone.

To be realistic, we must also be concerned about the magnitude of the torques used, since in actual applications we cannot exceed the maximum nor go below the minimum commandable values. Using Eq. (2.26), noting the assumed values for minimum and maximum commandable torques from Appendix C, the known value of $\tilde{I}_c = 1.7815 \times 10^5 \text{ kg m}^2$, and $\tilde{h}_o = 200 \text{ kg m}^2/\text{s}$ results in

$$\epsilon_{max} = \frac{\tilde{g}_{max} \tilde{I}_c}{\tilde{h}_o^2} \approx 0.891 \quad (4.3)$$

$$\epsilon_{min} = \frac{\tilde{g}_{min} \tilde{I}_c}{\tilde{h}_o^2} \approx 0.001 \quad (4.4)$$

The purpose of the following simulations is both to compare direct and sub-optimal control laws for attitude maneuvers, as well as demonstrate the growth in final state errors with increasing torque scaling parameter ϵ . The last example is also useful in comparing the sub-optimal control performance to the eigen-axis maneuvers mentioned above. Discussion and comparison of the simulation results for both GPS Block IIR and the Hubble Space Telescope is deferred to section 4.3.

Hubble Example 1 - Sub-optimal Trajectory

In the first example for Hubble, we will address the sub-optimal trajectory only for a combined 45° rotation about the $\hat{\mathbf{b}}_3$ and $\hat{\mathbf{b}}_1$ axes, with ϵ set at 0.01. Momentum wheels $\mathcal{W}_1 - \mathcal{W}_3$ are used, with \mathcal{W}_1 initially containing all the momentum for the vehicle. Table 4.7 summarizes the simulation parameters. The results are summarized in Figs. 4.21-4.26 and Table 4.8.

Table 4.7 Hubble Example 1 - Sub-optimal Simulation Parameters

parameter	value
\mathbf{A}	$(\mathbf{a}_1 \quad \mathbf{a}_2 \quad \mathbf{a}_3)$
\tilde{h}_o	$200 \text{ kg m}^2/\text{s}$
ϵ	0.01
ϕ_o, θ_o, ψ_o	0, 0, 0
ϕ_f, θ_f, ψ_f	$45^\circ, 45^\circ, 0$
μ_o	$(1 \quad 0 \quad 0)$

Table 4.8 Hubble Example 1 - Sub-optimal Simulation Results

result	Sub-optimal
\tilde{t}_f	$45 \text{ hr } 5 \text{ min}$
$ \tilde{\omega} _{max}$	$1.506 \times 10^{-5} \text{ rad/s}$
$ \tilde{\omega}_s _{max}$	287.4 rad/s
$ \tilde{\omega}(\tilde{t}_f) _{max}$	$8.871 \times 10^{-6} \text{ rad/s}$
ϕ_f, θ_f, ψ_f	$72.89, 37.74, -18.44^\circ$

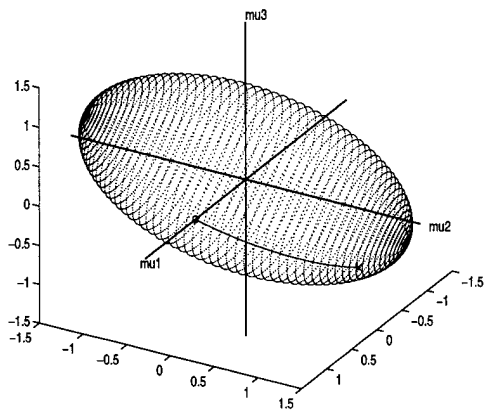


Figure 4.21 *Hubble Example 1 - (Sub-opt) Torque Trajectory on Wheel Momenta Ellipsoid*

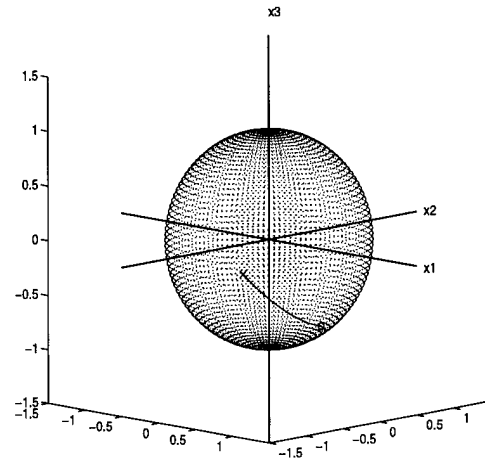


Figure 4.22 *Hubble Example 1 - (Sub-opt) Torque Trajectory on Total Momentum Sphere*

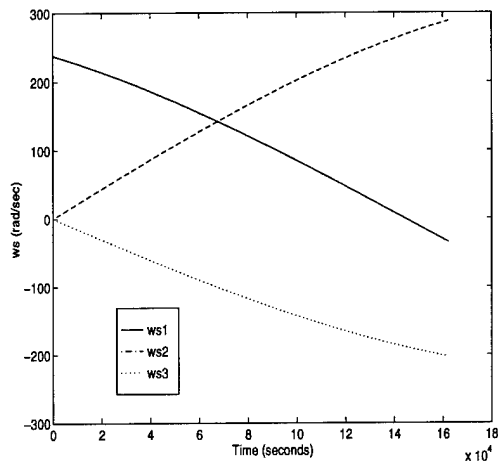


Figure 4.23 *Hubble Example 1 - (Sub-opt) Wheel Angular Velocities*

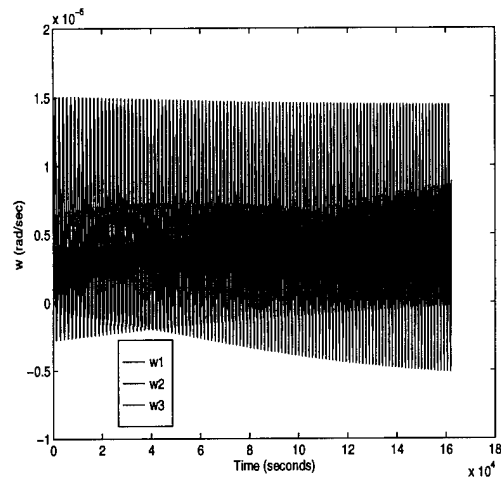


Figure 4.24 *Hubble Example 1 - (Sub-opt) Vehicle Angular Velocities*

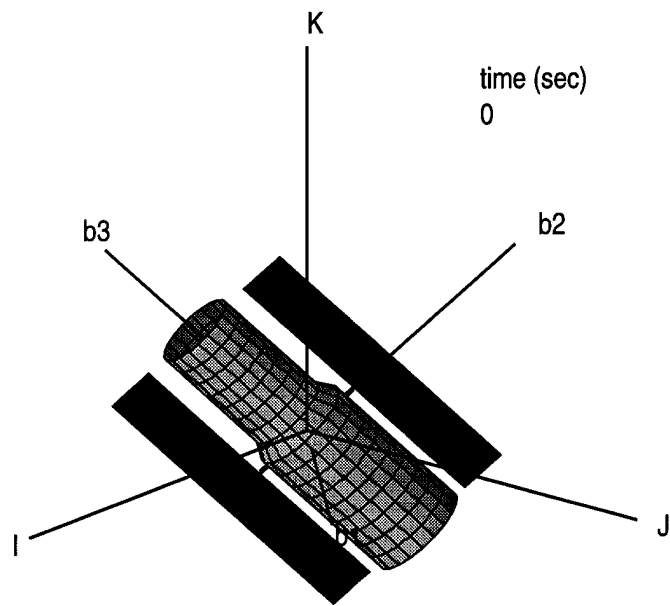


Figure 4.25 *Hubble Example 1 - Desired Final Attitude*

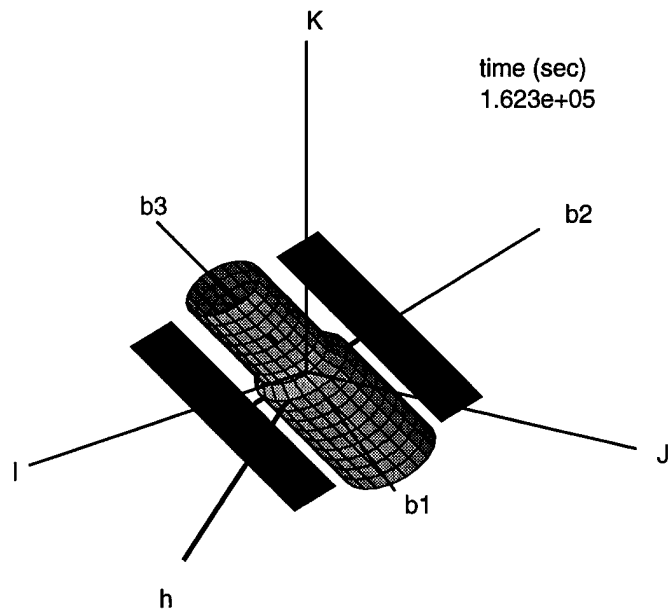


Figure 4.26 *Hubble Example 1 - (Sub-opt) Final Attitude*

Hubble Example 2 - Sub-optimal Trajectory

In the next example, we again address the sub-optimal trajectory only, this time increasing ϵ to 0.5. The other simulation parameters are identical to the first example. Table 4.9 summarizes the simulation parameters. The results are summarized in Figs. 4.27-4.32 and Table 4.10.

Table 4.9 Hubble Example 2 - Sub-optimal Simulation Parameters

parameter	value
A	(a₁ a₂ a₃)
\tilde{h}_o	200 kg m ² /s
ϵ	0.5
ϕ_o, θ_o, ψ_o	0, 0, 0
ϕ_f, θ_f, ψ_f	45°, 45°, 0
μ_o	(1 0 0)

Table 4.10 Hubble Example 2 - Sub-optimal Simulation Results

result	Sub-optimal
\tilde{t}_f	54 min
$ \tilde{\omega} _{max}$	6.909×10^{-4} rad/s
$ \tilde{\omega}_s _{max}$	287.4 rad/s
$ \tilde{\omega}(\tilde{t}_f) _{max}$	3.740×10^{-4} rad/s
ϕ_f, θ_f, ψ_f	72.94, 38.25, -2.89°

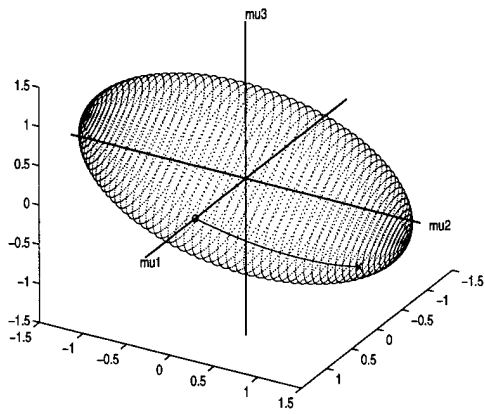


Figure 4.27 *Hubble Example 2 - (Sub-opt) Torque Trajectory on Wheel Momenta Ellipsoid*

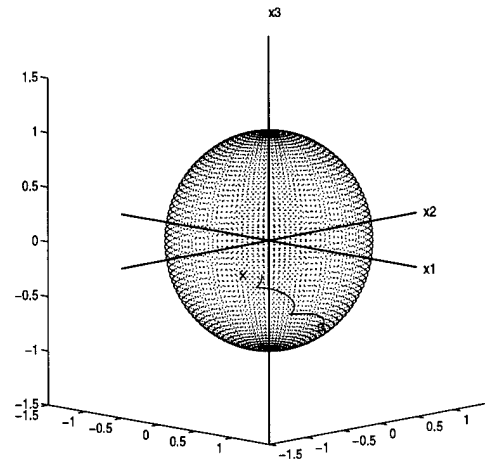


Figure 4.28 *Hubble Example 2 - (Sub-opt) Torque Trajectory on Total Momentum Sphere*

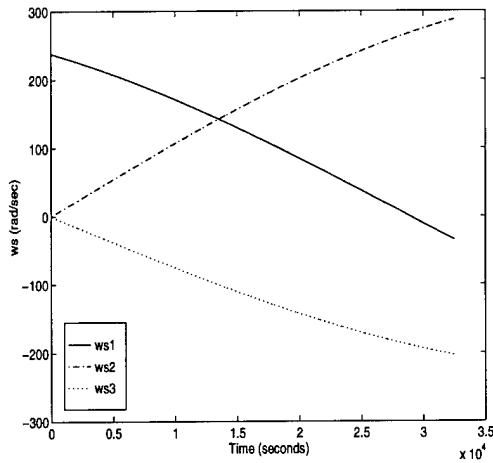


Figure 4.29 *Hubble Example 2 - (Sub-opt) Wheel Angular Velocities*

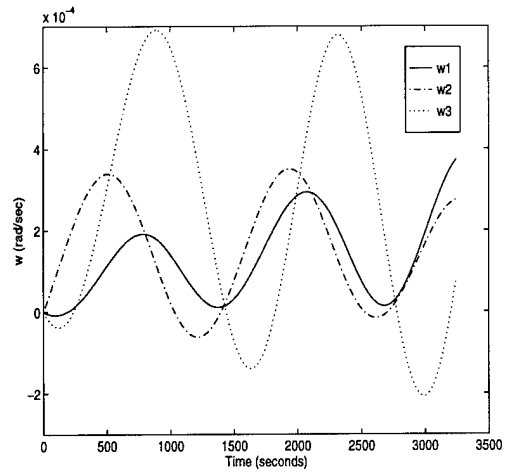


Figure 4.30 *Hubble Example 2 - (Sub-opt) Vehicle Angular Velocities*

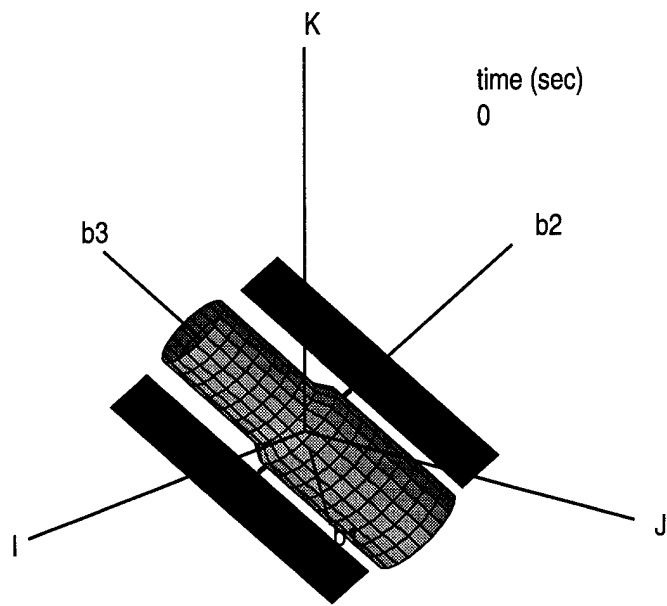


Figure 4.31 *Hubble Example 2 - Desired Final Attitude*

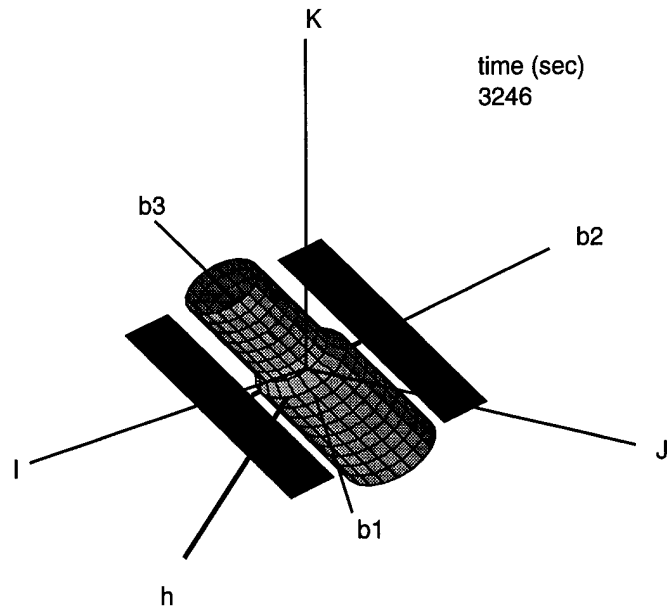


Figure 4.32 *Hubble Example 2 - (Sub-opt) Final Attitude*

Hubble Example 3 - Direct vs. Sub-optimal Trajectories

In this example for Hubble, both the direct and the sub-optimal control laws are used to attempt a positive 90° “slewing” maneuver about the $\hat{\mathbf{b}}_1$ axis. To keep both maneuver times and state errors reasonable, ϵ is set to 0.1. Wheels $\mathcal{W}_1 - \mathcal{W}_3$ are again used to perform the maneuver, with \mathcal{W}_2 initially containing all the angular momentum for the vehicle. Table 4.11 summarizes the simulation parameters. The results are summarized in Figs. 4.33-4.44 and Table 4.12.

Table 4.11 Hubble example 3 - Direct vs. Sub-optimal Simulation Parameters

parameter	value
\mathbf{A}	$(\mathbf{a}_1 \ \mathbf{a}_2 \ \mathbf{a}_3)$
\tilde{h}_o	$200 \text{ kg m}^2/\text{s}$
ϵ	0.10
ϕ_o, θ_o, ψ_o	0, 0, 0
ϕ_f, θ_f, ψ_f	0, 90°, 0
$\boldsymbol{\mu}_o$	$(0 \ 1 \ 0)$

Table 4.12 Hubble example 3 - Direct vs. Sub-optimal Simulation Results

result	Sub-optimal	Direct
\tilde{t}_f	$5 \text{ hr } 30 \text{ min}$	$3 \text{ hr } 30 \text{ min}$
$ \tilde{\omega} _{max}$	$1.702 \times 10^{-4} \text{ rad/s}$	$7.625 \times 10^{-4} \text{ rad/s}$
$ \tilde{\omega}_s _{max}$	336.7 rad/s	238.1 rad/s
$ \tilde{\omega}(\tilde{t}_f) _{max}$	$7.042 \times 10^{-5} \text{ rad/s}$	$2.050 \times 10^{-4} \text{ rad/s}$
ϕ_f, θ_f, ψ_f	$-0.65, 89.39, 0.28^\circ$	$-22.69, 96.15, 16.49^\circ$

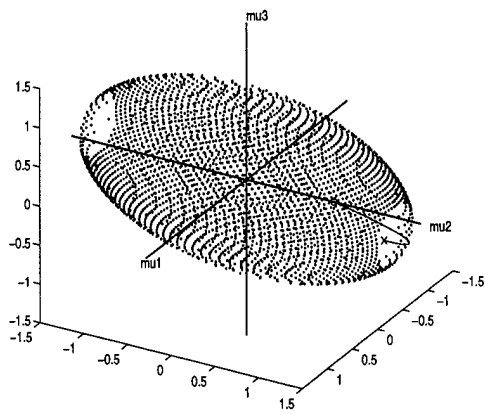


Figure 4.33 *Hubble Example 3 - (Sub-opt) Torque Trajectory on Wheel Momenta Ellipsoid*

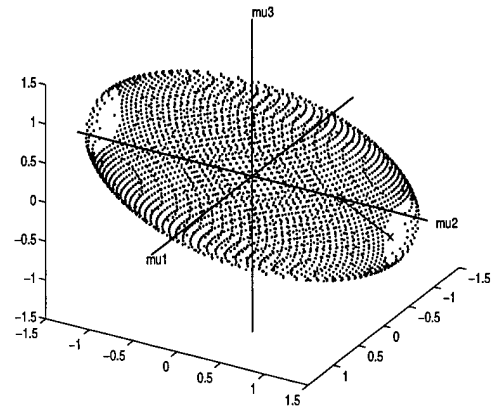


Figure 4.34 *Hubble Example 3 - (Direct) Torque Trajectory on Wheel Momenta Ellipsoid*

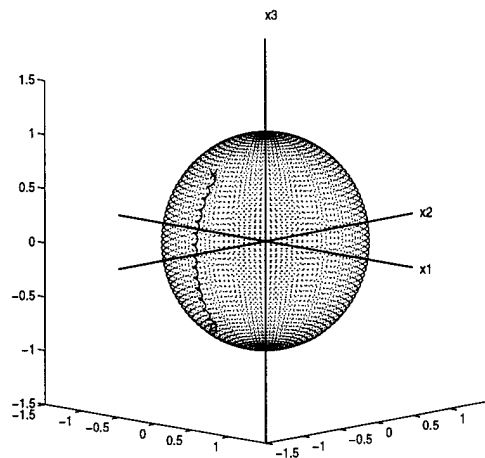


Figure 4.35 *Hubble Example 3 - (Sub-opt) Torque Trajectory on Total Momentum Sphere*

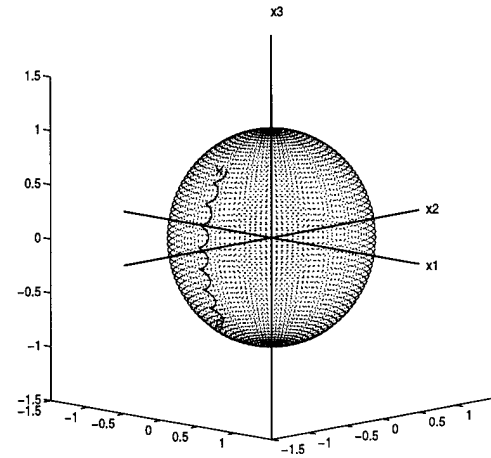


Figure 4.36 *Hubble Example 3 - (Direct) Torque Trajectory on Total Momentum Sphere*

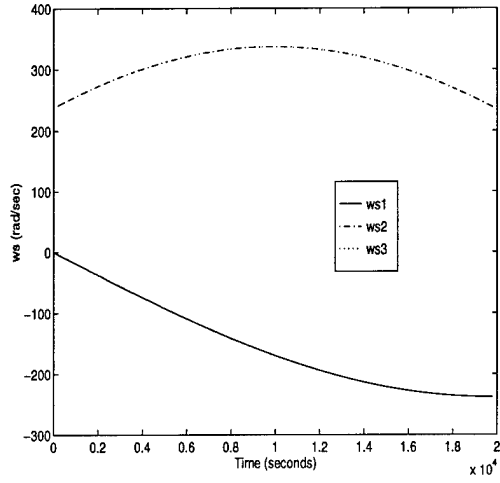


Figure 4.37 *Hubble Example 3 - (Sub-opt) Wheel Angular Velocities*

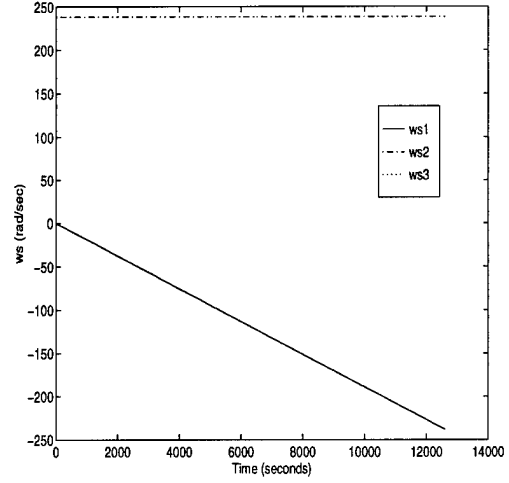


Figure 4.38 *Hubble Example 3 - (Direct) Wheel Angular Velocities*

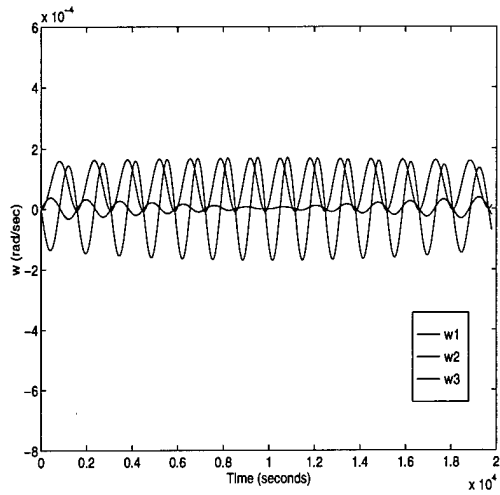


Figure 4.39 *Hubble Example 3 - (Sub-opt) Vehicle Angular Velocities*

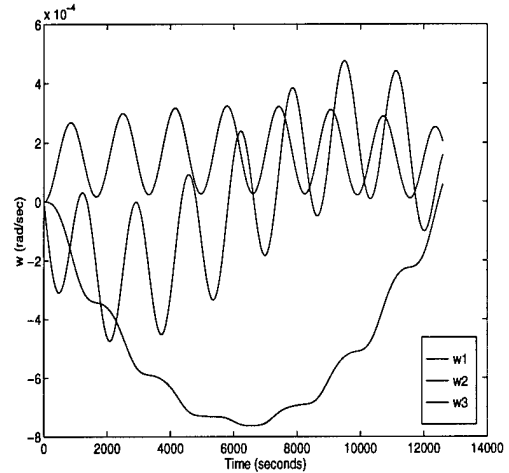


Figure 4.40 *Hubble Example 3 - (Direct) Vehicle Angular Velocities*

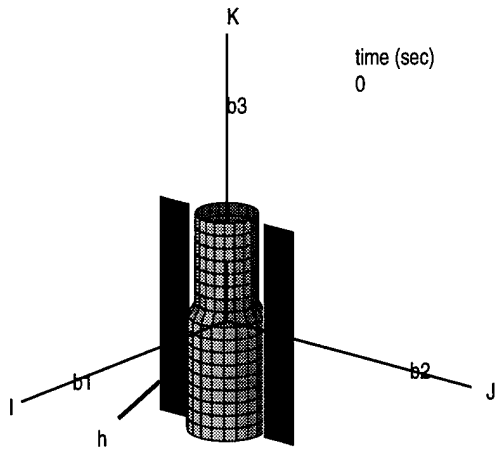


Figure 4.41 *Hubble Example 3 - Initial Attitude*

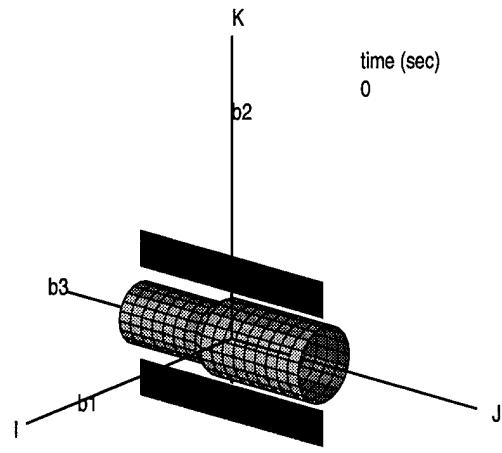


Figure 4.42 *Hubble Example 3 - Desired Final Attitude*

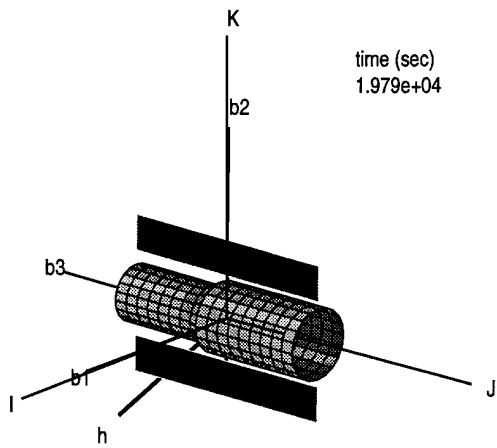


Figure 4.43 *Hubble Example 3 - (Sub-opt) Final Attitude*

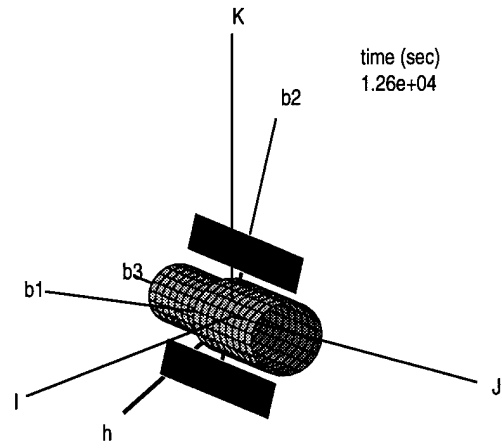


Figure 4.44 *Hubble Example 3 - (Direct) Final Attitude*

Hubble Example 4 - Sub-optimal Trajectory

In the final example for Hubble, we will perform the same maneuver as in Example 3, this time using wheels \mathcal{W}_1 , \mathcal{W}_2 , and \mathcal{W}_4 , with \mathcal{W}_2 initially containing all the momentum for the vehicle. Table 4.13 summarizes the simulation parameters. The results are summarized in Figs. 4.45-4.50 and Table 4.14.

Table 4.13 Hubble Example 4 - Sub-optimal Simulation Parameters

parameter	value
\mathbf{A}	$(\mathbf{a}_1 \quad \mathbf{a}_2 \quad \mathbf{a}_4)$
\tilde{h}_o	$200 \text{ kg m}^2/\text{s}$
ϵ	0.1
ϕ_o, θ_o, ψ_o	$0, 0, 0$
ϕ_f, θ_f, ψ_f	$0, 90^\circ, 0$
μ_o	$(0 \quad 1 \quad 0)$

Table 4.14 Hubble Example 4 - Sub-optimal Simulation Results

result	Sub-optimal
\tilde{t}_f	$3 \text{ hr } 53 \text{ min}$
$ \tilde{\omega} _{max}$	$2.406 \times 10^{-4} \text{ rad/s}$
$ \tilde{\omega}_s _{max}$	238.1 rad/s
$ \tilde{\omega}(\tilde{t}_f) _{max}$	$4.816 \times 10^{-5} \text{ rad/s}$
ϕ_f, θ_f, ψ_f	$-0.82, 90.43, 0.70^\circ$

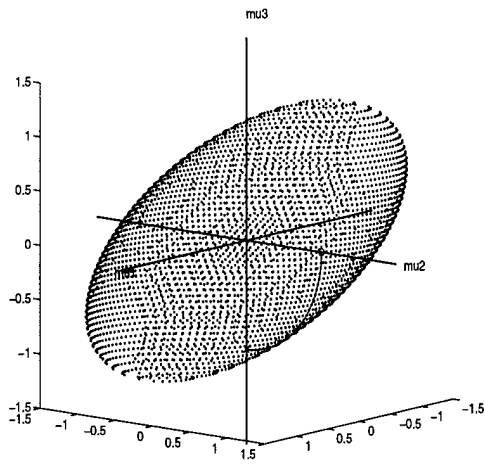


Figure 4.45 *Hubble Example 4 - (Sub-opt) Torque Trajectory on Wheel Momenta Ellipsoid*

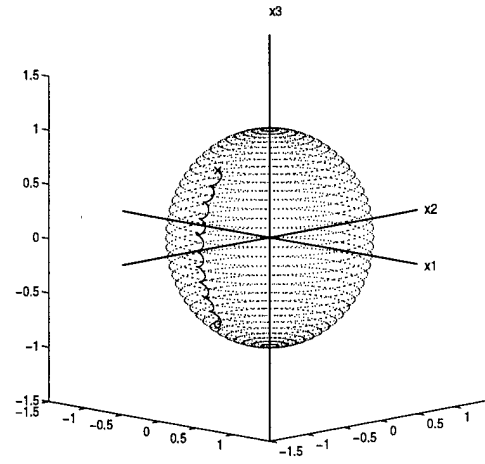


Figure 4.46 *Hubble Example 4 - (Sub-opt) Torque Trajectory on Total Momentum Sphere*

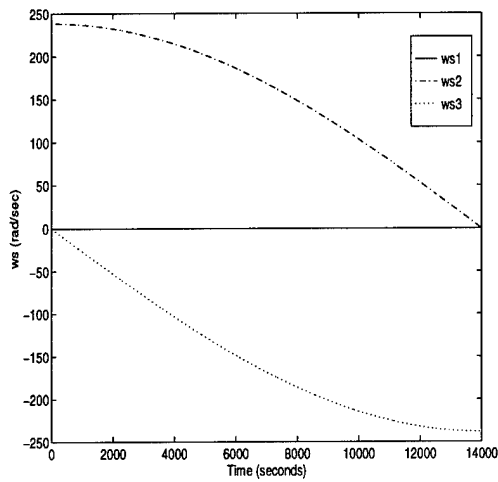


Figure 4.47 *Hubble Example 4 - (Sub-opt) Wheel Angular Velocities*

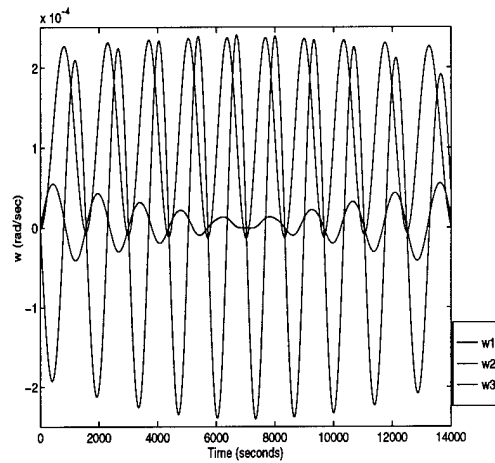


Figure 4.48 *Hubble Example 4 - (Sub-opt) Vehicle Angular Velocities*

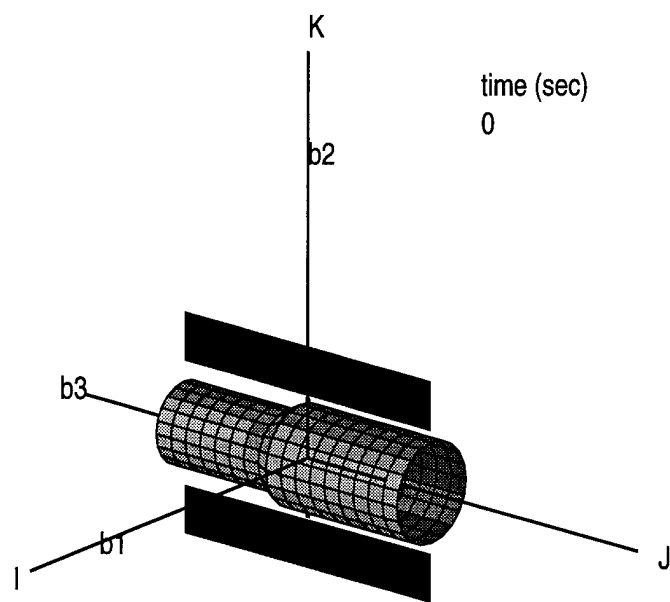


Figure 4.49 *Hubble Example 4 - (Sub-opt) Desired Final Attitude*

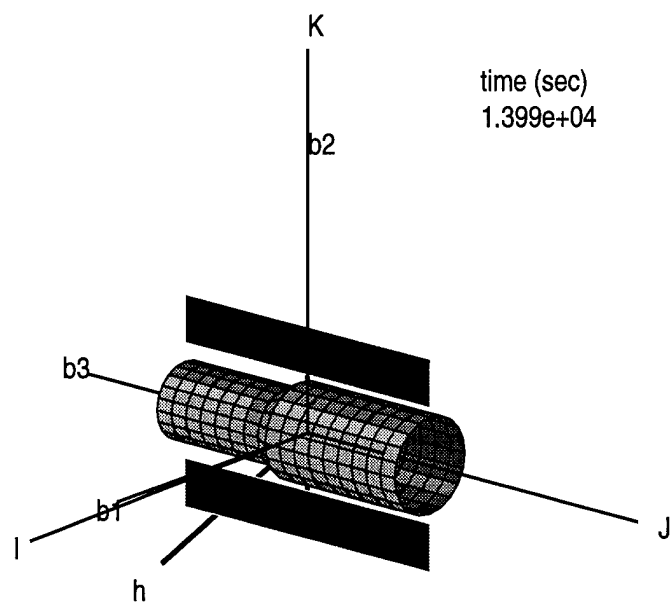


Figure 4.50 *Hubble Example 4 - (Sub-opt) Final Attitude*

4.3 Summary of Results

GPS Example 1 and Hubble Example 3 both compared direct and sub-optimal maneuvers for a specified initial conditions and desired final wheel momenta and vehicle attitude (See Tables 4.2 and 4.12). As discussed in Section 3.5, the relative time to complete a maneuver using both approaches varies depending on the parameters of the problem. For these two somewhat dissimilar examples, the sub-optimal trajectory required between 2 and 4 hours longer to complete the maneuver than the direct trajectory.

For both examples, the the maximum wheel speeds for the direct trajectory were well below the maximum allowable values, with the sub-optimal trajectory requiring slightly higher speeds. While the wheel speeds for GPS were well below the 943 rad/s limit for both approaches, the sub-optimal trajectory for the Hubble example exceeded the maximum of 314 rad/s for a small portion of the simulation. A look at the wheel speed histories in Figures 4.5, 4.6, 4.37, and 4.38 shows that it is due to the quadratic form of the sub-optimal control law that the maximum is reached in the sub-optimal cases. Thus, the sub-optimal control law is infeasible due to wheel speed limitations for smaller values of total angular momentum than is the direct trajectory. Recalling our discussion of achievable momenta ellipsoid regions in Section 3.2, it is apparent that trajectories that have initial and final states near the axes planes in \mathcal{F}_μ and near the “ends” of the major axis of the ellipsoid will traverse regions of the ellipsoid requiring larger wheel momenta due to the nature of the sub-optimal control law. In such cases, other trajectories on the ellipsoid surface would be necessary, or different sets of momentum wheels could be used. Hubble Example 4 uses \mathcal{W}_1 , \mathcal{W}_2 , and \mathcal{W}_4 to perform the same maneuver with the same total angular momentum, using the sub-optimal control law. Note that using these three wheels, the sub-optimal trajectory no longer traverses the unachievable regions of the ellipsoid, the final attitude is very close to desired, and the resulting maximum wheel speeds are below the limit throughout the simulation (Table 4.14). This clearly demonstrates the advantages of having a redundant non-coplanar wheel in momentum limited situations such as Example 3.

In terms of maximum vehicle angular velocities during maneuvers, the sub-optimal trajectory is clearly superior. While absolute angular velocities remained small for both direct and sub-optimal trajectories (due to small wheel torques), the *relative* magnitude for

the direct trajectories was between 4 and 18 times larger. This is certainly not surprising given the definition of the stationary platform condition and the way in which each torque trajectory traverses the stationary platform wheel momenta ellipsoid.

What is interesting are the final vehicle angular velocities using each approach for the two vehicles. One might expect that the sub-optimal trajectories, since they maintain smaller angular velocities throughout the maneuver, would “end up” with smaller final angular velocities. However, a glance at the results shows that this is not true in GPS Example 1. Deviations from the stationary platform condition (requiring $\mathbf{x} = \mathbf{A}\boldsymbol{\mu}$ and $\boldsymbol{\omega} = 0$) can be visualized by the magnitude of the “humps” on the torque trajectory traced on the total momentum sphere (Figures 4.3,4.4 and 4.35,4.36). Thus, larger deviations (caused by larger ϵ and/or straying farther off the wheel momenta ellipsoid surface) result in larger humps and larger variations in angular velocities. The *final* angular velocities (which can be thought of as state errors from the nominal $\boldsymbol{\omega} = 0$) depend on the distance between the *actual* final state \mathbf{x}_{act} vs. the *desired* final state \mathbf{x}_f which is calculated from the stationary platform condition $\mathbf{x}_f = \mathbf{A}\boldsymbol{\mu}_f$ in \mathbf{x} space at the time when the wheel torques are turned off. This is difficult to see in the GPS example (since ϵ is much smaller), but in the Hubble example (Fig. 4.36), it is obvious that \mathbf{x}_{act} is farther from \mathbf{x}_f (denoted by the \times on the sphere) in the direct trajectory case. However, because the period of the humps plays as important a role as the amplitude, there may be cases where the final state just happens to be closer to the desired state for the direct trajectory, even though absolute variations in angular velocities are greater. This situation occurs in Hubble Example 3.

Perhaps the most important results to consider are the errors in the final attitude after each maneuver. As shown in Table 4.12 and Figures 4.43 and 4.44, the sub-optimal control law results in final attitude within 0.65° of desired, while the direct trajectory leaves the vehicle over 20° off in some directions. As discussed at the end of Section 3.1, the final attitude for both trajectories is off by a finite rotation about the total angular momentum vector \mathbf{x} , recognizing that there are final state errors as well. It is clear that for this example, the sub-optimal control results in a much smaller necessary rotation about \mathbf{x} and thus significantly smaller final attitude errors.

Turning now to a comparison of the sub-optimal trajectories for varying values of ϵ (GPS Examples 1-3, Hubble Examples 1-2), it is evident that increasing ϵ for a given \tilde{h}_o reduces maneuver times but results in larger intermediate and final angular velocities and greater final attitude errors. These results are certainly not unexpected given the discussion earlier in the chapter.

What is interesting, though, is that when ϵ is increased significantly (e.g. 0.5 in Hubble Example 2), maneuver times become reasonable (less than an hour), angular velocities during the maneuver increase, yet the motion of the vehicle is still much "smoother" than the direct maneuver with much smaller torques (see Hubble Example 3). As a result, maneuvers can be accomplished in realistic time-frames and yet maintain small platform angular velocities and achieve a final attitude near the desired one. Although maneuver times using this approach were still greater than can be achieved currently with the Hubble using eigen-axis maneuvers, the nature of the motion is "smooth" and thus desirable. Obviously, the maximum value of ϵ found previously cannot be exceeded for a given \tilde{h}_o , since this would result in commanding the wheel torque motors beyond their practical limit. However, it is apparent that even at torques well below the maximum commandable (as in Hubble Example 2), the sub-optimal control law can effect large angle reorientations in reasonable times.

In all the examples for GPS and Hubble, the angular velocities at the end of the maneuvers were all of order 10^{-4} or smaller, while the maximum allowable body rates calculated in Sections 3.6.1 and 3.6.2 were of order $10^{-3} - 10^{-2}$. Thus, one might assume that the final angular velocities were acceptably small, and could be offset using additional momentum wheel control. However, it is important to note that the analyses previously performed to calculate these maximum body rates were approximate, and also assumed that the wheels were initially not spinning and were torqued to absorb this momentum. In all the examples above, the wheels *already* contain some angular momentum (i.e. they are spinning), and thus must absorb this additional angular momentum due to the body angular rates. Thus, depending on the magnitude of the body rates and the final wheel momenta, the additional residual angular momentum may or may not be absorbable by

the wheels without momentum dumping (using magnetic torquers and/or thrusters in the case of GPS).

Nonetheless, the examples show that the sub-optimal control is easily calculable, is superior to the constant torque case in terms of body angular rates and final state errors, and can be used to achieve large angle reorientations in reasonable times.

Now, let us introduce solar pressure and gravity gradient torques to increase the "realism" of the simulations, and assess the affect on intermediate angular velocities and final state errors.

V. Perturbed Stationary Platform Maneuvers

As discussed during the development of the external perturbing torque equations in Chapter 2, the magnitudes of solar pressure and gravity gradient torques vary depending on vehicle configuration, orbital altitude, and spacecraft attitude. While gravity gradient torques decrease in *absolute* magnitude with altitude, solar pressure torques remain essentially constant (since $P_{sun} = const$). Thus, for a given vehicle, as orbital altitude increases, the *relative* contribution of solar pressure to total external torques increases.

Both of these vehicles are in nearly circular orbits and are asymmetric in both physical shape and inertia properties. Recalling the discussion about gravity gradient stability from Section 2.3.1, we expect gravity to attempt to reorient both vehicles such that their minor axes are aligned with the local vertical. Of course, solar pressure is also affecting the attitude throughout the orbit.

GPS Block IIR vehicles are at much higher altitudes than Hubble and are significantly less massive, and as a result, gravity gradient torques are of roughly the same magnitude as solar pressure torques. Using Eq. (2.46) and (2.49) for GPS Block IIR an altitude of 26,560 km, assuming \mathcal{F}_b is the principal frame (this is nearly true), with the $\hat{\mathbf{b}}_1$ axis rotated $+45^\circ$ in the $\hat{\mathbf{e}}_1 - \hat{\mathbf{e}}_2$ plane initially, the solar pressure and gravity gradient torques are both found to be on the order of 10^{-6} N m. However, for Hubble, the same analysis at an altitude of 6,993 km results in gravity gradient being of order 10^{-2} N m at times, while solar pressure torques remain of order 10^{-5} N m. The solar pressure torques are larger on average for Hubble due to its larger surface area.

As a result of this difference in both relative and absolute external torques, we expect that Hubble will experience greater fluctuation in angular momentum and thus larger state errors during stationary platform maneuvers than GPS for equivalent maneuver times.

GPS Block IIR vehicles also have significantly longer orbital periods than Hubble (≈ 12 hrs vs. ≈ 1.6 hrs). If the Earth's gravitational field were modeled more accurately (not uniform), and if eclipse effects were included, both solar pressure and gravity gradient torques would be more pronounced for the Hubble since multiple revolutions could occur during a 2 hour maneuver.

All of these factors result in net changes in total angular momentum ($\tilde{\mathbf{h}}$) of the vehicle. The sub-optimal wheel torque control law developed in Chapter 3 assumed that $\tilde{\mathbf{h}}$ was constant, since it was based on the stationary platform condition $\mathbf{x} = \mathbf{A}\boldsymbol{\mu}$ which was non-dimensionalized by an initial "nominal" angular momentum ($\tilde{\mathbf{h}}_o$). Changes in total angular momentum from the "nominal" thus result in a change in the "size" of the total momentum sphere and the stationary platform wheel momenta ellipsoid. Accordingly, even though the sub-optimal control law is closed-loop in the sense that the control is calculated based on vehicle states ($\boldsymbol{\mu}$ and \mathbf{x}), it is based on an incomplete dynamics model.

In real applications, then, as the wheel momenta ellipsoid expands and contracts, some provision is necessary to control the wheel speeds to "stay" on the ellipsoid surface if a stationary platform is desired. Furthermore, if a particular stationary attitude is desired, the wheels must be controlled to stay at a particular point on the ellipsoid surface. Finally, if a stationary platform maneuver is attempted, the vehicle states would need to be accurately estimated to allow constant modification of the sub-optimal trajectory.

Two examples are presented below which demonstrate the relative and absolute effects of solar pressure and gravity gradient torques during a stationary platform maneuver. The first example is the same maneuver as performed in GPS Example 3 in Chapter 3, with perturbing torques included. The second example is the same as Hubble Example 4, with torques included. These two examples were chosen for several reasons. The maneuver times are both reasonable and nearly equal ($\approx 1 \times 10^4$ s), final attitudes were close to desired, and final angular velocities were small ($10^{-4} - 10^{-5}$ rad/s).

Analysis of the results of both simulations is presented in Section 5.3.

5.1 Example Using GPS Blk IIR

This example using GPS Block IIR is the same as GPS Example 3 in Chapter 4, with solar pressure and gravity gradient torques acting on the vehicle. Table 5.1 summarizes the simulation parameters. The results are summarized in Figs. 5.1-5.6 and Table 5.2.

Table 5.1 GPS example 4 - Perturbed Sub-optimal Simulation Parameters

parameter	value
\mathbf{A}	$(\mathbf{a}_1 \quad \mathbf{a}_2 \quad \mathbf{a}_4)$
\tilde{h}_o	$5 \text{ kg m}^2/\text{s}$
ϵ	0.10
ϕ_o, θ_o, ψ_o	0, 0, 0
ϕ_f, θ_f, ψ_f	$45^\circ, 45^\circ, 0$
μ_o	(1 0 0)

Table 5.2 GPS example 4 - Perturbed Sub-optimal Simulation Results

result	Sub-optimal
\tilde{t}_f	2 hr 52 min
number of orbital periods	0.24
$ \tilde{\omega} _{max}$	$2.210 \times 10^{-4} \text{ rad/s}$
$ \tilde{\omega}_s _{max}$	613.2 rad/s
$ \tilde{\omega}(\tilde{t}_f) _{max}$	$1.577 \times 10^{-4} \text{ rad/s}$
ϕ_f, θ_f, ψ_f	1.04, 77.39, 14.07°

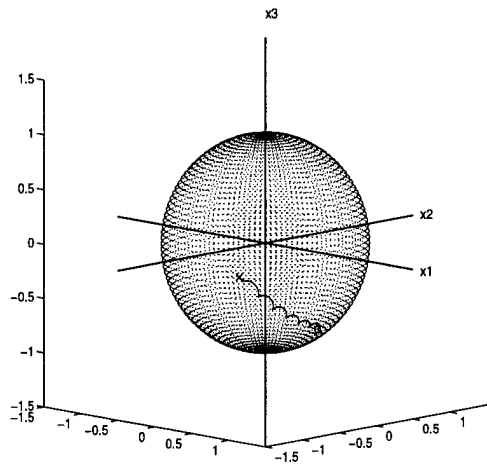


Figure 5.1 *GPS Example 4 - (Sub-opt) Perturbed Torque Trajectory on Total Momentum Sphere*

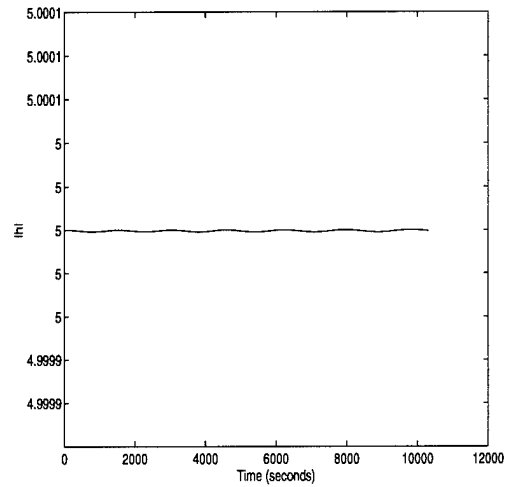


Figure 5.2 *GPS Example 4 - (Sub-opt) Perturbed Total Angular Momentum Magnitude*

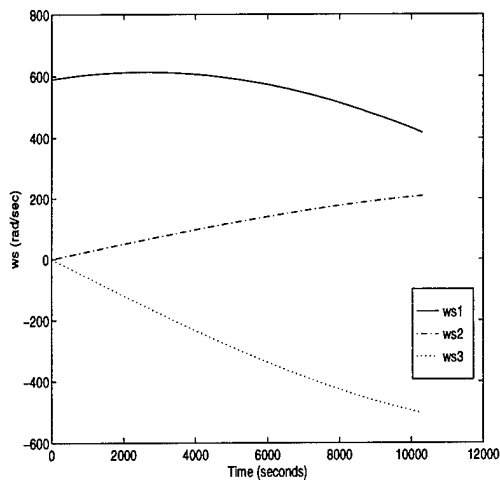


Figure 5.3 *GPS Example 4 - (Sub-opt) Perturbed Wheel Angular Velocities*

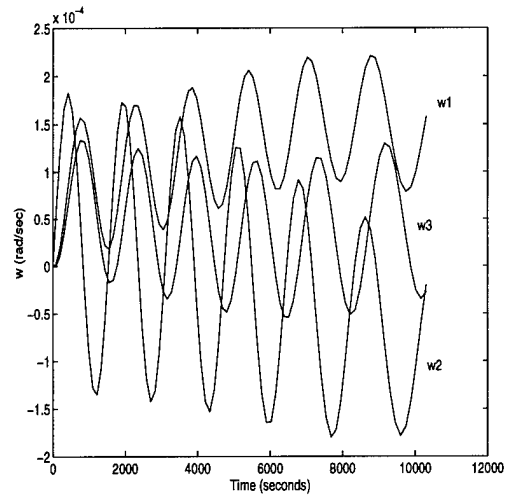


Figure 5.4 *GPS Example 4 - (Sub-opt) Perturbed Vehicle Angular Velocities*

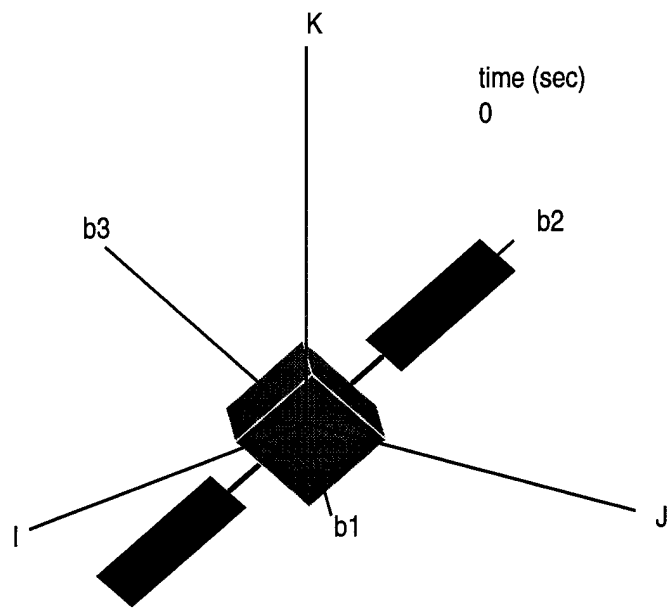


Figure 5.5 *GPS Example 4 - Desired Final Attitude*

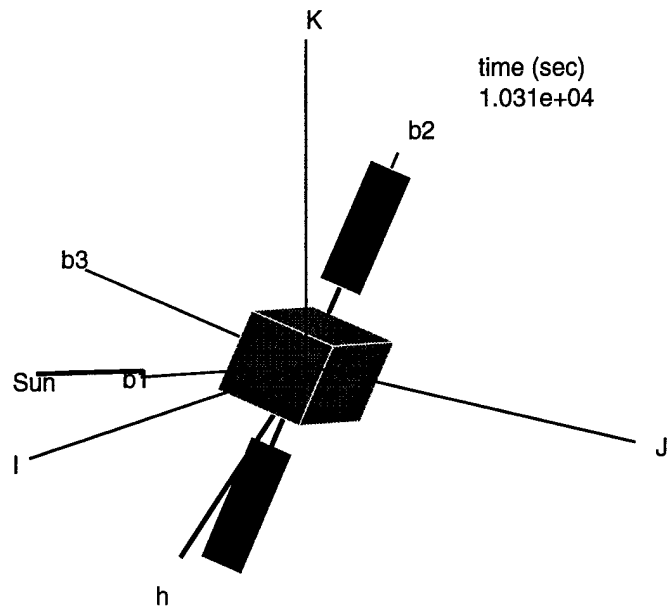


Figure 5.6 *GPS Example 4 - (Sub-opt) Perturbed Final Attitude*

5.2 Example Using Hubble Space Telescope

This example for Hubble Space Telescope is the same as Hubble Example 4 in Chapter 4, with solar pressure and gravity gradient torques acting on the vehicle. Table 5.3 summarizes the simulation parameters. The results are summarized in Figs. 5.7-5.12 and Table 5.4.

Table 5.3 Hubble Example 5 - Perturbed Sub-optimal Simulation Parameters

parameter	value
\mathbf{A}	$(\mathbf{a}_1 \quad \mathbf{a}_2 \quad \mathbf{a}_4)$
\tilde{h}_o	$200 \text{ kg m}^2/\text{s}$
ϵ	0.10
ϕ_o, θ_o, ψ_o	0, 0, 0
ϕ_f, θ_f, ψ_f	0, 90°, 0
μ_o	$(0 \quad 1 \quad 0)$

Table 5.4 Hubble Example 5 - Perturbed Sub-optimal Simulation Results

result	Sub-optimal
\tilde{t}_f	3 hr 53 min
number of orbital periods	2.40
$ \tilde{\omega} _{max}$	$1.582 \times 10^{-3} \text{ rad/s}$
$ \tilde{\omega}_s _{max}$	238.1 rad/s
$ \tilde{\omega}(\tilde{t}_f) _{max}$	$5.690 \times 10^{-4} \text{ rad/s}$
ϕ_f, θ_f, ψ_f	53.84, 66.31, -54.49°

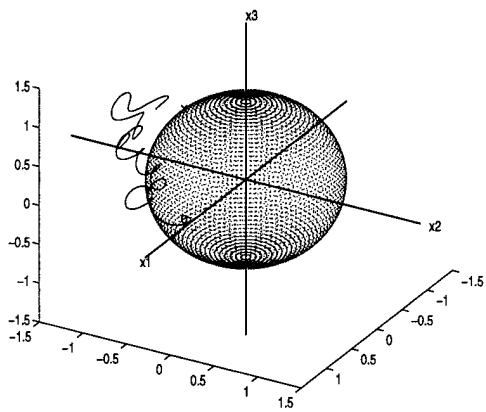


Figure 5.7 *Hubble Example 5 - (Sub-opt) Perturbed Torque Trajectory on Total Momentum Sphere*

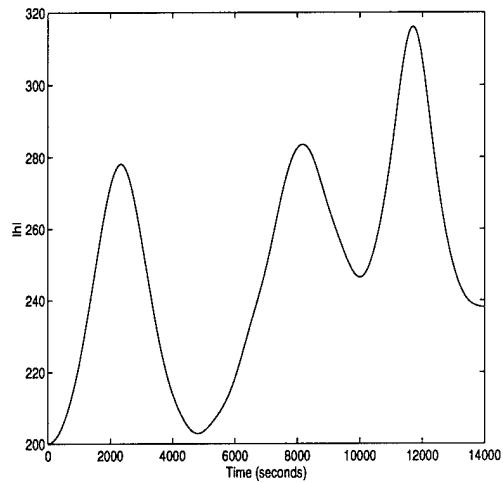


Figure 5.8 *Hubble Example 5 - (Sub-opt) Perturbed Total Angular Momentum Magnitude*

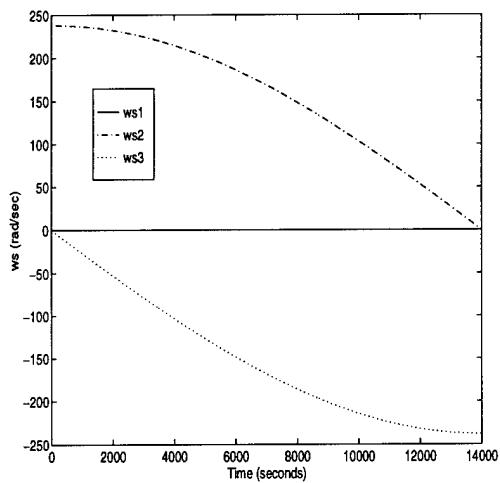


Figure 5.9 *Hubble Example 5 - (Sub-opt) Perturbed Wheel Angular Velocities*

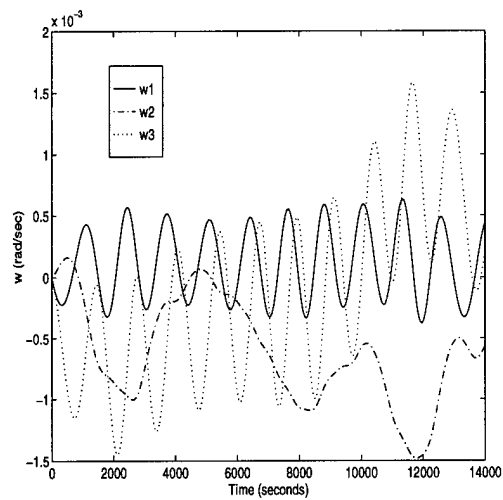


Figure 5.10 *Hubble Example 5 - (Sub-opt) Perturbed Vehicle Angular Velocities*

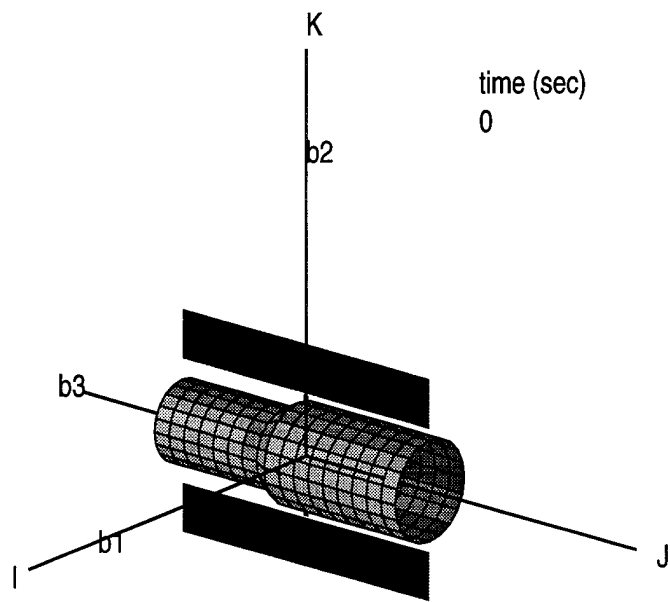


Figure 5.11 *Hubble Example 5 - Desired Final Attitude*

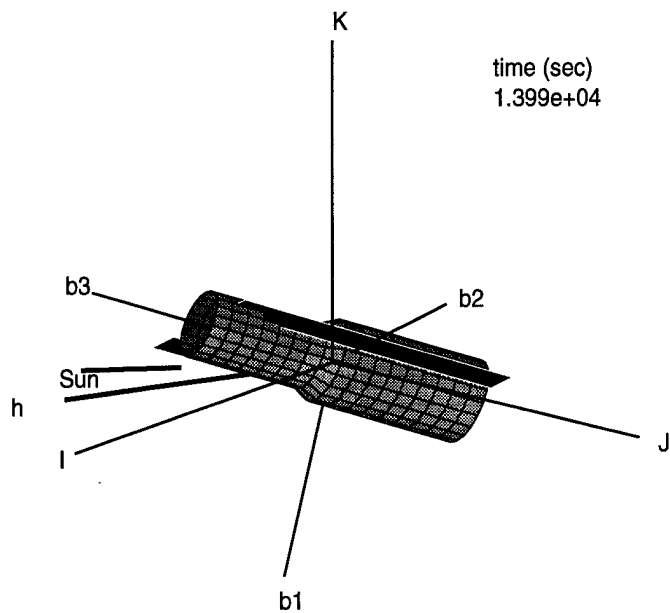


Figure 5.12 *GPS Example 5 - (Sub-opt) Perturbed Final Attitude*

5.3 Summary of Results

As expected, the maximum angular velocities during the perturbed maneuvers increased for both vehicles compared to the unperturbed maneuvers. Again as predicted, the increase for Hubble was more dramatic (≈ 6.56 times) than for GPS (≈ 1.16 times). The maximum final angular velocities likewise increased more for Hubble than for GPS (≈ 11.81 times vs. ≈ 1.97 times), and the pointing accuracy at the completion of the maneuver is arguably better for GPS. The figures show that Hubble does indeed experience both a greater *absolute* increase in total momentum (Figs. 5.2 and 5.8) and a greater *relative* increase (Figs. 5.1 and 5.7), due to its greater mass, surface area, and lower altitude orbit.

The maneuver time for GPS was approximately 2.9 hours, compared to nearly 3.9 hours for the Hubble. This equates to nearly 2.4 orbital periods for Hubble vs. only 0.24 for GPS. These relatively long maneuvers (compared to Hubble Example 2 which is less than an hour) were intentionally chosen to show the relative affects of the perturbing torques for these two vehicles. The same affects would be present, although less obvious, for more "realistic" wheel torques ($\epsilon \approx 0.5$) as well. A glance at Figs. 5.3 and 5.9 shows that while both experience general growth in angular velocities, the gravity gradient and solar pressure torques are more evident in Hubble Example 5, particularly for ω_2 . As expected, the gravity gradient has more time to act on Hubble, and is attempting to align the minor axis with the local vertical.

Even though the performance of the sub-optimal control law appears to be *better* for for GPS than for Hubble in the presence of perturbing torques, in terms of final attitude errors it is clearly inadequate in its present implementation. It is obvious that a closed loop controller needs to be developed which can use estimates of the vehicle states (wheel angular velocities, vehicle angular velocities, vehicle attitude) to control wheel torques to traverse the stationary platform torque trajectory even when the momenta ellipsoid is expanding and the angular velocity vector is moving with respect to inertial space. However, the results of these simulations using it in open-loop form indicate that it is more effective for vehicles experiencing smaller perturbing torques. This is particularly true since increases in total angular momentum will result in the need for increased wheel

speeds for almost all maneuvers, which could push the wheels to their commandable limits. For the Hubble, such limits would be reached more quickly, resulting in more unachievable stationary attitudes, or to avoid this, the need for more frequent momentum dumping using the magnetic torquers.

VI. Conclusions and Recommendations

6.1 Conclusions

This report focused on reorientations of a rigid spacecraft with three axisymmetric momentum wheels. After deriving the equations of motion and expressions for solar pressure and gravity gradient torques in Chapter 2, two conditions involving the spacecraft angular momentum and wheel angular momenta were presented in Chapter 3 such that the vehicle could be held stationary with respect to inertial space using the momentum wheels alone. After deriving a constant wheel torque control law (*direct trajectory*) to transfer wheel angular momentum without regard to intermediate angular velocities, a *sub-optimal* wheel torque control law was presented that kept angular velocities small throughout the maneuver.

Simulation runs using both the direct and sub-optimal control law were performed in Chapter 4 for the GPS Block IIR and Hubble Space Telescope vehicles, in an environment free from external perturbing torques. As expected, intermediate angular velocities, final angular velocities, and final attitude errors were significantly smaller using the sub-optimal control law vs. using constant torques. Also, as the magnitude of the control torques increased using the sub-optimal approach, angular velocities (intermediate and final) increased, as did the final attitude error. However, by increasing the small torque parameter ϵ to 0.5, a 45° reorientation of the Hubble Space Telescope about two axes was accomplished in 54 minutes using the sub-optimal control law, with acceptably small intermediate and final angular velocities and final attitude close to desired. The resulting motion was quite "smooth" compared to the direct maneuver, and showed the applicability of this type of control scheme in real applications.

Gravity gradient and solar pressure torques were introduced in Chapter 5, and two previous simulations were re-run with these torques present (one for GPS, one for Hubble). As the preliminary analysis predicted, the effects on Hubble were much greater than on GPS Block IIR for equivalent time spans, due to Hubble's larger surface area, greater mass, and lower altitude orbit. Intermediate and final angular velocities increased 6-11 times over the unperturbed maneuver, compared to only 1-2 times for GPS. Although

difficult to judge, the final attitude for GPS appeared to be slightly closer to desired than Hubble.

All things considered, the sub-optimal control law worked well for both GPS Block IIR and Hubble Space Telescope in the unperturbed environment. However, due to the inherently open-loop nature of the control law as developed, it failed to perform well in the presence of perturbing torques for either vehicle. The following section presents some specific ideas for future research that will enhance the utility of this control law in real applications.

6.2 Recommendations for Further Study

The sub-optimal control law as currently developed suffers from two basic weaknesses. The first is that vehicle kinematics are not considered in the formulation, resulting in an essentially arbitrary (although small) rotation about the angular momentum vector at the completion of maneuvers, even in the unperturbed case. This certainly limits its utility in real applications where precise control over pointing of communications and/or remote sensing hardware is required. Future work could thus focus on including the quaternions (or other attitude parameters) into the development of trajectories along the surface of the stationary platform condition wheel momenta ellipsoid. The resulting torque control trajectories would result in "smooth" large angle reorientations with reduced attitude errors. Calculation of such trajectories would in all likelihood not be as simple as the one developed herein, and thus care should be taken to avoid complicated computations that could not easily be performed by the on-board computer.

Another limitation of this control law is that it is based on an assumption of perfect knowledge of the vehicle momentum (\mathbf{x}) and wheel momenta ($\boldsymbol{\mu}$), and is calculated assuming that total angular momentum of the vehicle does not change. As demonstrated in Chapter 5, external perturbing torques cause the angular momentum to change with time, resulting in increased body motion and final attitude and state errors. The control law thus needs to be modified to allow for adjustment of control torques based on actual vehicle angular momentum. This would require an increase in the fidelity of the spacecraft models to include vehicle and wheel angular velocity estimation from sensor data (star sensors,

horizon sensors, wheel tachometers, etc.). The attitude control logic could thus calculate current angular momentum, body rates, wheel angular momentum, and spacecraft attitude, constantly determining the wheel torque trajectory necessary to move "closer" to the stationary platform momenta ellipsoid (to regulate angular rates) as well as to accurately reorient the vehicle to its final stationary attitude.

Once a sub-optimal control law is found that accounts for final attitude, it would be interesting to compare the resulting trajectory to optimal control solutions of the problem. Specifically, if one solved an optimal control problem with an objective function involving the final states (\mathbf{x}_f , $\boldsymbol{\mu}_f$, and \mathbf{q}_f), as well as weighted penalties on state variations and control usage, it would be interesting to see the results. Three cases would be of particular interest. First, specifying the end-time to be equal to the sub-optimal maneuver would allow direct comparison of state variations for the two approaches. Second, the problem could be formulated to obtain a minimum time solution to see what the "fastest" trajectory is (again compare state variations). Finally, leaving end-time free would result in minimization of states and controls without regard to time, and the relative magnitude of the resulting angular velocities as compared to the sub-optimal approach would be very interesting. Hopefully, results would show that the sub-optimal approach is "close" to optimal control solutions (for the fixed final time and perhaps minimum time cases), and by virtue of its simplicity, a candidate for implementation in future attitude control systems.

Appendix A. Constants and Unit Conversions

Physical Constants

μ_{\oplus}	=	$3.986012 \times 10^5 \text{ kg m}^3/\text{s}^2$	Earth gravitational parameter [3:429]
P_{sun}	=	$4.644 \times 10^{-6} \text{ N/m}^2$	Solar radiation pressure at 1 Earth radius [1:134]
R_{\oplus}	=	6378.135 km	Mean equatorial radius of Earth

Unit Conversions

Source: CRC Tables [4]

1 in.	=	0.0254 m
1 nmi.	=	1.15077945 mi.
1 mi.	=	1.609344 km
1 lb.	=	0.45359237 kg
1 lb.	=	4.448 N

Appendix B. Global Positioning System (GPS) Block IIR Modeling Data

Sources for data are indicated in the section headings. Data within a section that were either derived or taken from other sources are labeled accordingly.

B.1 Mass and Inertia Properties Calculations

Source: [17]

The original mass properties data contained in the GPS Block IIR mass properties report [17] included detailed identification of spacecraft components, their locations within the vehicle, and their masses. Thus, foreign export of the document was restricted. However, the data extracted for use and used in this appendix is neither exactly replicated nor in sufficient detail to warrant such restrictions.

Figure B.1 represents the fully deployed configuration for the GPS Block IIR vehicle used in mass properties calculations. The following data were estimated based on source data:

Vehicle total mass, on-orbit beginning of life:	$m_{tot} = 2423.4 \text{ lb} \approx 1099.2 \text{ kg}$
Solar array mass (each):	$m_{sa} = 103.304 \text{ lb} \approx 46.858 \text{ kg}$
Solar array surface area (each):	$A_{sa} = 7.65 \text{ m}^2$
Solar array mass/area ratio (derived):	6.125 kg/m^2

Moments and products of inertia (in \mathcal{F}_b frame), relative to spacecraft center of mass, on-orbit, fully deployed, beginning of life are given as

$$\begin{aligned}\tilde{I}_{11} &= 15267 \text{ in lbf s}^2 && \approx 1724.9 \text{ kg m}^2 \\ \tilde{I}_{22} &= 6924 \text{ in lbf s}^2 && \approx 782.27 \text{ kg m}^2 \\ \tilde{I}_{33} &= 17875 \text{ in lbf s}^2 && \approx 2019.5 \text{ kg m}^2 \\ \tilde{I}_{12} &= I_{21} = -233 \text{ in lbf s}^2 && \approx -26.324 \text{ kg m}^2 \\ \tilde{I}_{13} &= I_{31} = -4 \text{ in lbf s}^2 && \approx -0.45192 \text{ kg m}^2 \\ \tilde{I}_{23} &= I_{32} = -233 \text{ in lbf s}^2 && \approx -26.32 \text{ kg m}^2\end{aligned}$$

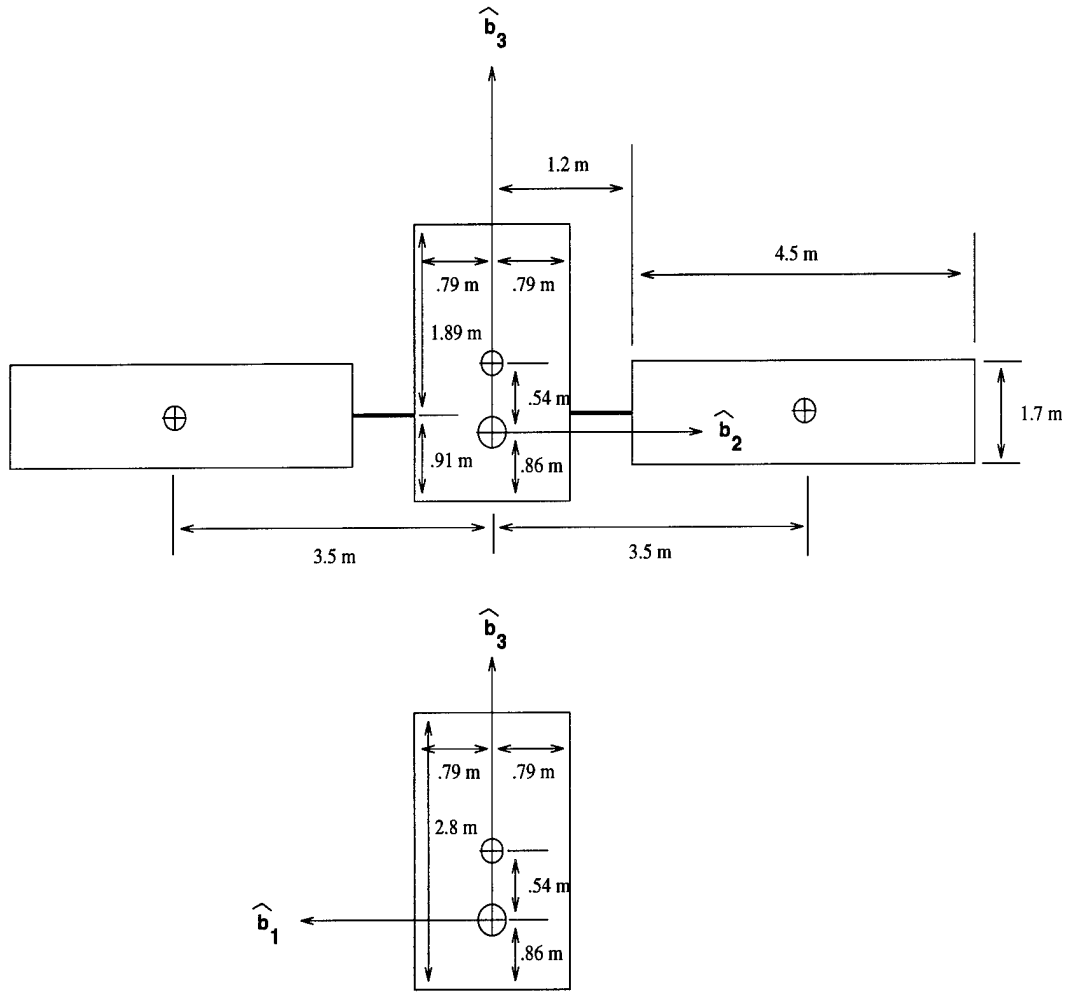


Figure B.1 GPS Block IIR Estimated Dimensions (Front and Side)

B.2 Material Properties

Assumed properties for solar pressure modeling are as follows:

$$\rho_a = 0.3 \quad (\text{fraction of incident photons absorbed})$$

$$\rho_s = 0.4 \quad (\text{fraction of incident photons specularly reflected})$$

$$\rho_d = 0.3 \quad (\text{fraction of incident photons diffusely reflected})$$

B.3 Momentum Wheel Assembly Properties Calculations

Sources: [19],[7]

Momentum wheel orientation in vehicle, with respect to body fixed frame \mathcal{F}_b are given as

$$\begin{aligned}\hat{\mathbf{a}}_1 &= \left(\sqrt{2}/2 \quad 0 \quad -\sqrt{2}/2 \right)^T \\ \hat{\mathbf{a}}_2 &= \left(0 \quad -\sqrt{2}/2 \quad -\sqrt{2}/2 \right)^T \\ \hat{\mathbf{a}}_3 &= \left(-\sqrt{2}/2 \quad 0 \quad -\sqrt{2}/2 \right)^T \\ \hat{\mathbf{a}}_4 &= \left(0 \quad \sqrt{2}/2 \quad -\sqrt{2}/2 \right)^T\end{aligned}$$

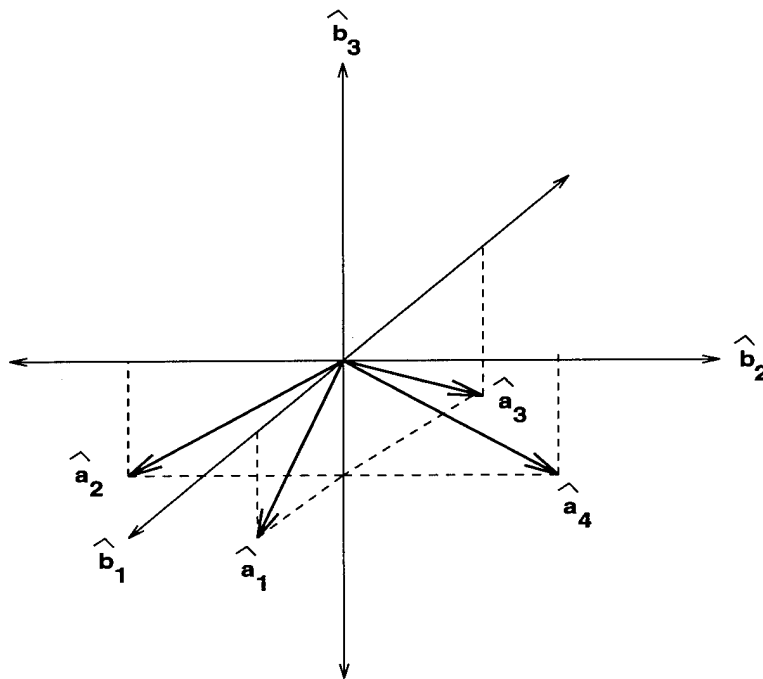


Figure B.2 GPS Block IIR Wheel Orientations

Axial wheel moments of inertia

$$\tilde{I}_{s1} = \tilde{I}_{s2} = \tilde{I}_{s3} = \tilde{I}_{s4} = 0.075 \text{ in lb s}^2 \approx 0.00847 \text{ kg m}^2$$

Maximum momentum wheel angular rate: $\pm 9000 \text{ rpm} \approx \pm 943 \text{ rad/s}$

Minimum commandable wheel motor torque (derived): $\pm 2.768 \times 10^{-4} \text{ N m}$

Maximum commandable wheel motor torque (derived): $\pm 0.071 \text{ N m}$

B.4 Orbital Parameters

Source: [18]

All of the following parameters were assumed constant for modeling simplicity:

a	$=$	26559.91 km	(semi-major axis)
e	$=$	0.0039	(eccentricity)
i	$=$	54.28°	(inclination)
ω	$=$	0.0°	(right ascension of node (assumed value for modeling simplicity))
Ω	$=$	$\pi/2$	(argument of perigee (assumed value for modeling simplicity))
T_o	$=$	0 s	(time of perigee passage (assumed value for modeling simplicity))

Appendix C. Hubble Space Telescope Modeling Data

Sources for data are indicated in the section headings. Data within a section that were either derived or taken from other sources are labeled accordingly.

C.1 Mass and Inertia Properties Calculations

Source: [2]

Figure C.1 represents the fully deployed configuration for the Hubble Space Telescope vehicle used in mass properties calculations. The following data were obtained from the source or assumed as indicated:

Vehicle total mass, on-orbit beginning of life:	$m_{tot} = 24000 \text{ lb} \approx 10886 \text{ kg}$
Estimated solar array surface area (each):	$A_{sa} = 16 \text{ m}^2$
Assumed solar array mass/area ratio (from Appendix A):	6.125 kg/m^2
Estimated solar array mass (derived):	$m_{sa} = 6.1252(A_{sa}) \approx 98 \text{ kg}$

The moments and products of inertia were derived by first calculating the inertia matrices for each of the four components of the vehicle (small cylinder, large cylinder, two solar arrays) about their mass centers, calculating the mass center for the entire vehicle, and then translating each component's inertia matrix to the vehicle mass center using the parallel axis theorem as outlined by Likins [16:524-525].

The spacecraft body was modeled as a small right circular cylinder (radius 1.5 m, height 4 m) adjoined to a large right circular cylinder (radius 2 m, height 5 m), both of uniform mass distribution. Each solar array was modeled as a thin rectangular plate (height 8 m, width 2 m, thickness 0.05 m). The solar arrays were assumed to be equal distance from the $\hat{\mathbf{b}}_3$ axis and in the $\hat{\mathbf{b}}_2 - \hat{\mathbf{b}}_3$ plane.

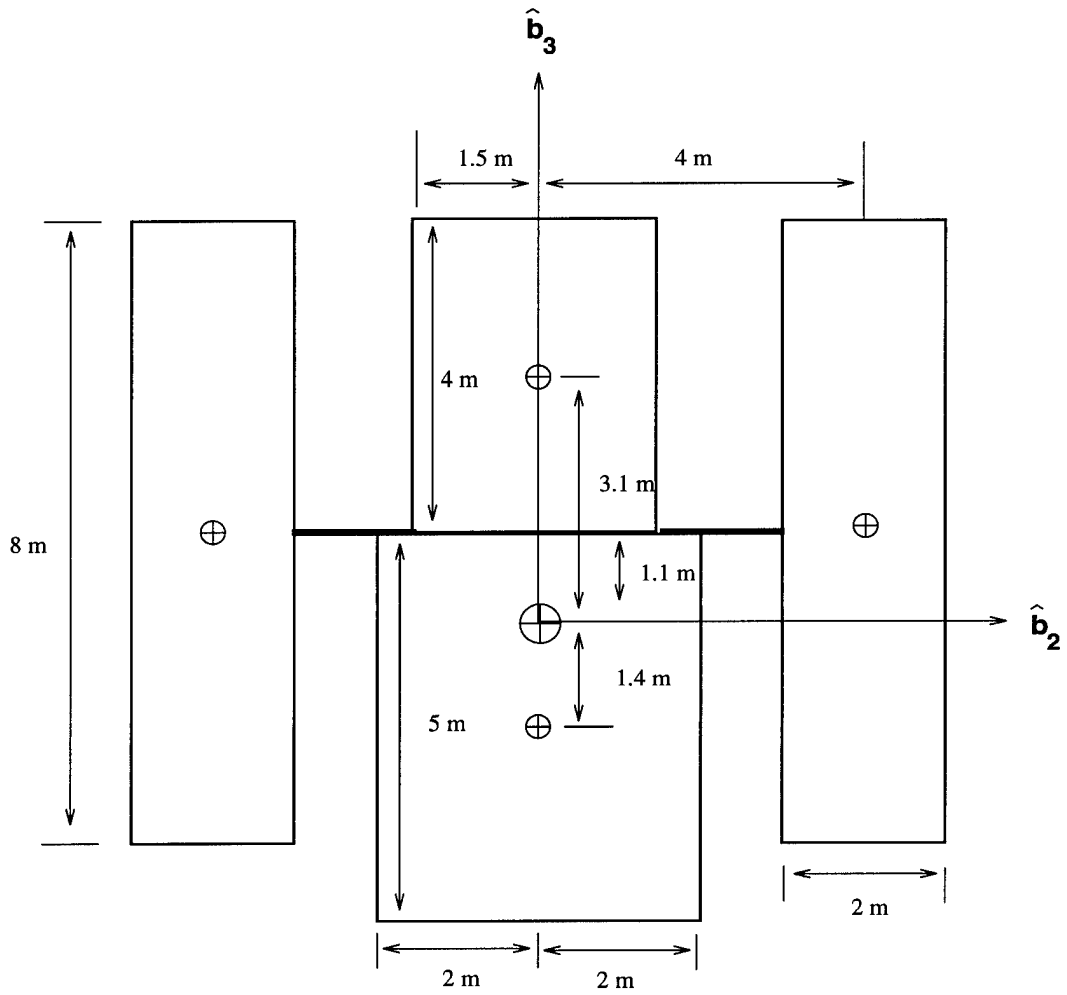


Figure C.1 *Hubble Space Telescope Estimated Dimensions*

Given these assumptions, the moments and products of inertia for the composite spacecraft about the center of mass, expressed in \mathcal{F}_b are

$$\tilde{I}_{11} \approx 79836 \text{ kg m}^2$$

$$\tilde{I}_{22} \approx 76634 \text{ kg m}^2$$

$$\tilde{I}_{33} \approx 21679 \text{ kg m}^2$$

$$\tilde{I}_{12} = I_{21} = 0$$

$$\tilde{I}_{13} = I_{31} = 0$$

$$\tilde{I}_{23} = I_{32} = 0$$

C.2 Material Properties

Assumed properties for solar pressure modeling are as follows:

$$\rho_a = 0.3 \quad (\text{fraction of incident photons absorbed})$$

$$\rho_s = 0.4 \quad (\text{fraction of incident photons specularly reflected})$$

$$\rho_d = 0.3 \quad (\text{fraction of incident photons diffusely reflected})$$

C.3 Momentum Wheel Assembly Properties Calculations

Sources: [2],[20]

Momentum wheel orientation in vehicle, with respect to body fixed frame \mathcal{F}_b (assumed):

$$\begin{aligned}\hat{\mathbf{a}}_1 &= \left(\sqrt{2}/2 \quad 0 \quad -\sqrt{2}/2 \right)^T \\ \hat{\mathbf{a}}_2 &= \left(0 \quad -\sqrt{2}/2 \quad -\sqrt{2}/2 \right)^T \\ \hat{\mathbf{a}}_3 &= \left(-\sqrt{2}/2 \quad 0 \quad -\sqrt{2}/2 \right)^T \\ \hat{\mathbf{a}}_4 &= \left(0 \quad \sqrt{2}/2 \quad -\sqrt{2}/2 \right)^T\end{aligned}$$

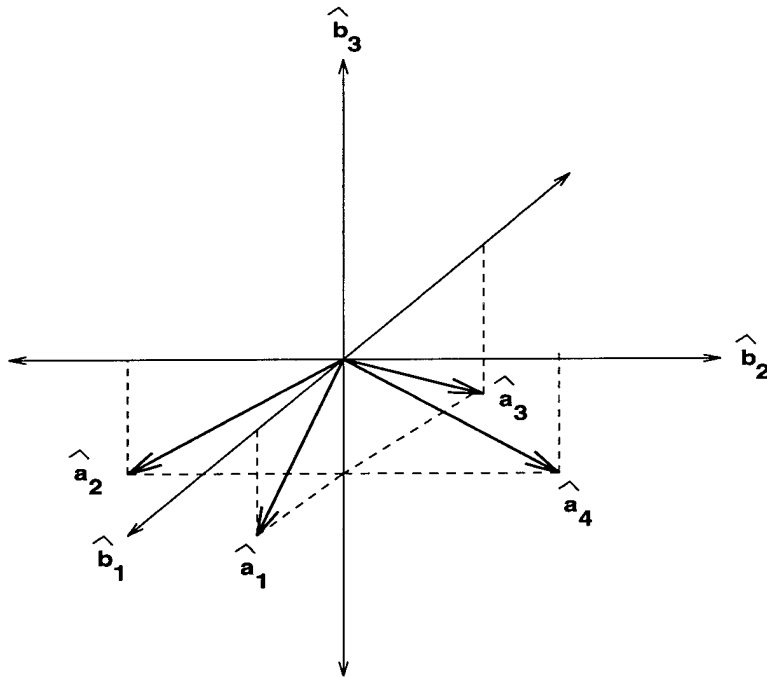


Figure C.2 *Hubble Space Telescope Assumed Wheel Orientations*

Axial wheel moments of inertia

$$\tilde{I}_{s1} = \tilde{I}_{s2} = \tilde{I}_{s3} = \tilde{I}_{s4} = 0.84 \text{ kg } m^2$$

Maximum momentum wheel angular rate: $\pm 3000 \text{ rpm} \approx \pm 314 \text{ rad/s}$

Minimum commandable wheel motor torque (Assumed): $0.2 \text{ N } m$

Maximum commandable wheel motor torque (Assumed): $3.0 \times 10^{-4} \text{ N } m$

C.4 *Orbital Parameters*

Source: [20]

All of the following parameters were assumed constant for modeling simplicity:

a	$=$	6993.135 km	(semi-major axis)
e	$=$	0.001	(eccentricity)
i	$=$	45°	(inclination)
ω	$=$	0.0°	(right ascension of node (assumed value for modeling simplicity))
Ω	$=$	$\pi/2$	(argument of perigee (assumed value for modeling simplicity))
T_o	$=$	0 s	(time of perigee passage (assumed value for modeling simplicity))

Appendix D. MATLAB Code Listings

The following programs were developed by the author from January-November 1995. They are MATLABTM script files, and along with the standard MATLABTM library routines, provide full functionality for all simulations conducted in this report. The programs were run on a Sun SPARCstation 20 workstation under Sun Operating System ver. 4.1 or later and MATLABTM ver. 4.2c.

Figure D.1 portrays the functional flow of data within the programs.

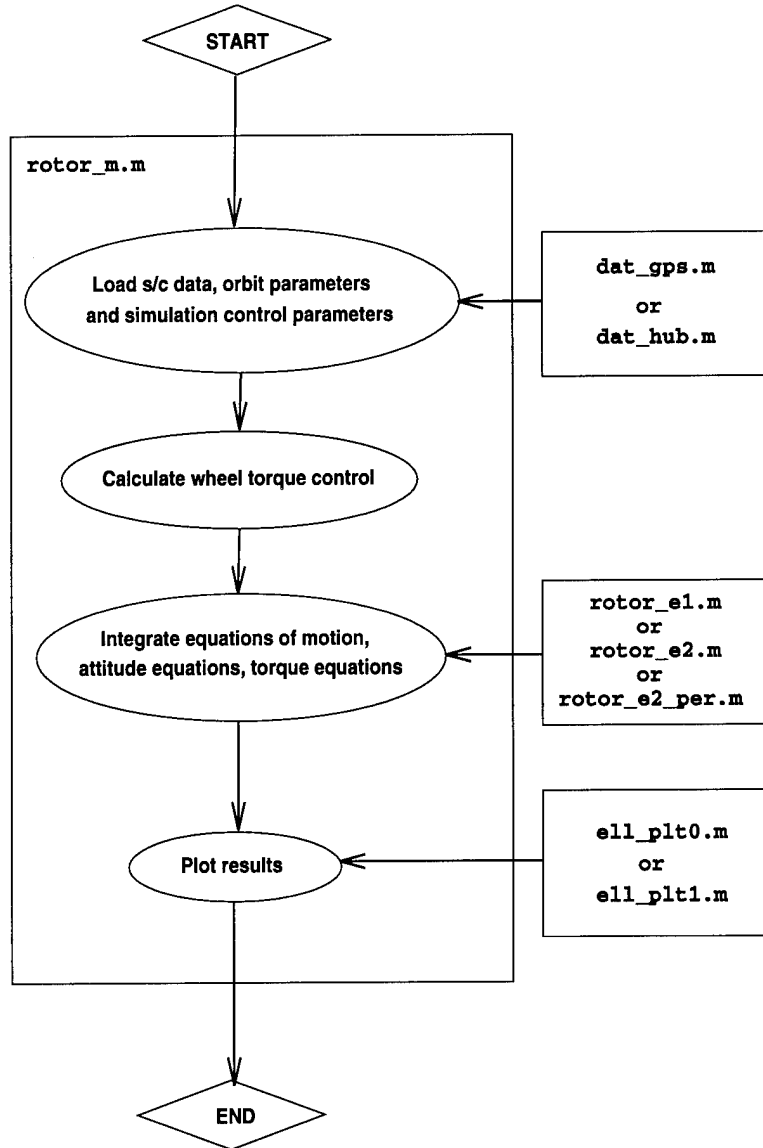


Figure D.1 Simulation Program Functional Flow Diagram

D.1 GPS Block IIR Data Definition File

```

1  %%%%%%%%%%%%%%%%%%%%%%%%%%%%%%%%%%%%%%%%%%%%%%%%%%%%%%%%%%%%%%%%%%%%%%%%%
2  %%%                                %%%
3  %%%                dat_gps.m        %%%
4  %%%                                %%%
5  %%%                Capt Greg Schultz, GA-95D    %%%
6  %%%                                %%%
7  %%%                revision          %%%
8  %%%                -----          %%%
9  %%%                11.03.95.0830      %%%
10 %%%                                %%%
11 %%%%%%%%%%%%%%%%%%%%%%%%%%%%%%%%%%%%%%%%%%%%%%%%%%%%%%%%%%%%%%%%%%%%%%%%%
12 %
13 %   This generates parameters for the
14 %   3 momentum wheel vehicle simulation
15 %   run in file rotor_m.m for the GPS
16 %   Block IIR spacecraft
17 %
18 %%%%%%%%%%%%%%%%%%%%%%%%%%%%%%%%%%%%%%%%%%%%%%%%%%%%%%%%%%%%%%%%%%%%%%%%%
19 %%%%   SIMULATION CONTROL PARAMETERS   %%%%
20 %%%%%%%%%%%%%%%%%%%%%%%%%%%%%%%%%%%%%%%%%%%%%%%%%%%%%%%%%%%%%%%%%%%%%%%%%
21 %
22 satmod=1;           % Satellite model to use for 3-D plots (1=GPS, 2=Hubble)
23 pltflg1=1;         % Turn momentum ellipsoid plots on/off (1/0)
24   ellflg=1;        % Select momentum ellipsoid plotting method and resolution
25   inc0=.01;        %   0=achievable regions of ellipsoid, point-by-point (slow)
26   inc1=3;          %   1=entire ellipsoid, parameterized method (fast)
27 pltflg2=1;         % Turn dimen. momenta, ang. veloc. plots on/off (1/0)
28 pltflg3=0;         % Turn non-dimen. momenta, ang. veloc. plots on/off (1/0)
29 pltflg4=1;         % Turn 3-D attitude plots on/off (1/0)
30 pertflg=0;         % Turn grav. grad. and solar press. torques on/off (1/0)
31                   %   0 =none  1 =sol. press. only  2 =sol. press. and grav.
32 small=0.1;         % Value of small parameter on torques. Should be (+)
33 r=1;               % Momentum wheels to use
34                   %   0 = (1/2/3), 1 = (1/2/4), 2 = (1/3/4), 3 = (2/3/4)
35 ph_o=0;            % Initial Euler angle phi   about e3 axis (deg)
36 th_o=0;            % Initial Euler angle theta about e1 axis (deg)
37 ps_o=0;            % Initial Euler angle psi   about e3 axis (deg)
38                   %
39 ph_f=45;           % Final Euler angle phi   about e3 axis (deg)
40 th_f=45;           % Final Euler angle theta about e1 axis (deg)
41 ps_f=0;            % Final Euler angle psi   about e3 axis (deg)
42                   %
43 h_o=5;             % Magnitude of vehicle ang. momentum (constant) [kg*m^2/s]
44                   %   used to dimensionalize results. Note that since vehicle

```

```

45          % ang. veloc. ~0, larger h_0 <--> higher rotor momenta;
46 mu_o=[1 0 0]; % Initial non-dimen. rotor momenta (stationary platform)
47          % format: mu_o=[mu1 mu2 mu3]
48          % use mu_o=-99 to generate random point
49 ths0=135;    % Initial sun vector angle from e1 (CCW, in degrees)
50 traj=2;     % Wheel torque trajectory
51          % (1=direct 2=suboptimal)
52 t0=0;       % Start time for integration (sec).
53 tf=-999;   % Stop time for integration (sec). Use -999 for autocalc.
54          % NOTE: non-dimen. values calculated below s/c properties
55 num=2;     % desired number of 3-D attitude plots for this time span
56 %
57 %
58 %%%%%%%%%%%%%%%%%%%%%%%%%%%%%%%%%%%%%%%%%%%%%%%%%%%%%%%%%%%%%%%
59 %%%%%% SPACECRAFT PHYSICAL PROPERTIES %%%%%%
60 %%%%%%%%%%%%%%%%%%%%%%%%%%%%%%%%%%%%%%%%%%%%%%%%%%%%%%%%%%%%%%%
61 %
62 % Inertia, Mass, and coordinate frame data obtained from Navstar GPS
63 % Block IIR Phase II Mass Properties Report, 9 Mar 95
64 %
65 a1=[sqrt(2)/2; 0; -sqrt(2)/2]; % wheel orientation w.r.t
66 a2=[0; -sqrt(2)/2; -sqrt(2)/2]; % body fixed frame b (and XYZ)
67 a3=[-sqrt(2)/2; 0; -sqrt(2)/2];
68 a4=[0; sqrt(2)/2; -sqrt(2)/2];
69 Is1=.00847; % Axial moments of inertia of the
70 Is2=.00847; % 4 momentum wheels (kg*m^2)
71 Is3=.00847;
72 Is4=.00847;
73 ws1max=9000*2*pi/60; % Maximum wheel angular speed magnitudes (rad/s)
74 ws2max=9000*2*pi/60;
75 ws3max=9000*2*pi/60;
76 ws4max=9000*2*pi/60;
77 %
78 I=[ 15267 -233 -4; % GPS Blk IIR on-orbit inertia tensor,
79 -233 6924 -46; % relative to mass center in XYZ frame
80 -4 -46 17875]; % units are in*lb*sec^2
81 %
82 I=(.0254)*(4.448)*I; % Convert from in*lb*sec^2 to kg*m^2
83 % (.0254 m/in)(4.448 N/lb)(in*lb*sec^2)=
84 % N*m*sec^2 = (kg*m/sec^2)*m*sec^2=kg*m^2
85 %
86 Ic=trace(I); % Charact. inertia for non-dimensionalizing
87 % (note: this is frame invariant)
88 I_d=I;
89 I=I_d./Ic; % Non dimensionalized inertia matrix

```

```

90 %
91 Is_d=eye(3); % Create diagonal matrix template;
92 Is_d(1,1)=Is1; % Default Configuration (r=0);
93 Is_d(2,2)=Is2;
94 Is_d(3,3)=Is3;
95 if r==1 % Fill remaining diagonal entries of Is
96 Is_d(3,3)=Is4; % Based on choice of wheel combination.
97 elseif r==2
98 Is_d(2,2)=Is3;
99 Is_d(3,3)=Is4;
100 elseif r==3
101 Is_d(1,1)=Is2;
102 Is_d(2,2)=Is3;
103 Is_d(3,3)=Is4;
104 end;
105 %
106 Is=Is_d./Ic; % Non dimensionalized inertia of wheels
107 %
108 % Now define vectors from vehicle c.m. to component centers
109 % of pressure for solar pressure modeling (m), the effective areas (m^2)
110 % and the surface normal vectors (all in Fb)
111 %
112 rs(1,:)= [1 0 0]; % +b1 face
113 rs(2,:)= [-1 0 0]; % -b1 face
114 rs(3,:)= [0 1 0]; % +b2 face
115 rs(4,:)= [0 -1 0]; % -b2 face
116 rs(5,:)= [0 0 -1]; % -b3 face
117 rs(6,:)= [0 0 1]; % +b3 face
118 rs(7,:)= [0 3.5 .37]; % +b2 solar array FRONT
119 rs(8,:)= [0 -3.5 .37]; % -b2 solar array FRONT
120 rs(9,:)= [0 3.5 .37]; % +b2 solar array BACK
121 rs(10,:)= [0, -3.5 .37]; % -b2 solar array BACK
122 As(1)=4.424;
123 As(2)=4.424;
124 As(3)=4.424;
125 As(4)=4.424;
126 As(5)=2.4964;
127 As(6)=2.4964;
128 As(7)=7.65;
129 As(8)=7.65;
130 As(9)=7.65;
131 As(10)=7.65;
132 ns(1,:)= [1 0 0];
133 ns(2,:)= [-1 0 0];
134 ns(3,:)= [0 1 0];

```

```

135 ns(4,:)= [0 -1 0];
136 ns(5,:)= [0 0 -1];
137 ns(6,:)= [0 0 1];
138 ns(7,:)= [1 0 0];
139 ns(8,:)= [1 0 0];
140 ns(9,:)= [-1 0 0];
141 ns(10,:)= [-1 0 0];
142 %
143 %%%%%%%%%%%%%%%%%%%%%%%%%%%%%%%%%%%%%%%%%%%%%%%%%%%%%%%%%%%%%%%%%%%%%%%%%%
144 %%%%%%          ORBITAL PARAMETERS          %%%%%%
145 %%%%%%%%%%%%%%%%%%%%%%%%%%%%%%%%%%%%%%%%%%%%%%%%%%%%%%%%%%%%%%%%%%%%%%%%%%
146 %
147 % Note: right ascension of the node is assumed to be 0,
148 %       and the argument of perigee is assumed to be pi/2
149 %
150 sma=26559.91;           % Semi-major axis (km)
151 ecc=0.0039;            % Eccentricity
152 incl=deg2rad(54.28);   % Inclination (degrees)
153 %
154 %%%%%%%%%%%%%%%%%%%%%%%%%%%%%%%%%%%%%%%%%%%%%%%%%%%%%%%%%%%%%%%%%%%%%%%%%%
155 %%%%%%          NON-DIMENSIONALIZE TIMES          %%%%%%
156 %%%%%%%%%%%%%%%%%%%%%%%%%%%%%%%%%%%%%%%%%%%%%%%%%%%%%%%%%%%%%%%%%%%%%%%%%%
157 %
158 % This is necessary for equation consistency for integration
159 % Must be done here since Ic needed from above
160 %
161 t0=h_o*t0/Ic;
162 if tf>0, tf=h_o*tf/Ic; end; % don't recalculate if tf=-999

```

D.2 Hubble Space Telescope Data Definition File

```

1  %%%%%%%%%%%%%%%%%%%%%%%%%%%%%%%%%%%%%%%%%%%%%%%%%%%%%%%%%%%%%%%%%%%%%%%%%%
2  %%%                                %%%
3  %%%                                dat_hub.m                                %%%
4  %%%                                %%%
5  %%%                                Capt Greg Schultz, GA-95D                %%%
6  %%%                                %%%
7  %%%                                revision                                %%%
8  %%%                                -----                                %%%
9  %%%                                11.02.95.1130                            %%%
10 %%%                                %%%
11 %%%%%%%%%%%%%%%%%%%%%%%%%%%%%%%%%%%%%%%%%%%%%%%%%%%%%%%%%%%%%%%%%%%%%%%%%%
12 %
13 %   This generates parameters for the
14 %   3 momentum wheel vehicle simulation
15 %   run in file rotor_m.m for the
16 %   Hubble Space Telescope spacecraft
17 %
18 %%%%%%%%%%%%%%%%%%%%%%%%%%%%%%%%%%%%%%%%%%%%%%%%%%%%%%%%%%%%%%%%%%%%%%%%%%
19 %%%%   SIMULATION CONTROL PARAMETERS   %%%%
20 %%%%%%%%%%%%%%%%%%%%%%%%%%%%%%%%%%%%%%%%%%%%%%%%%%%%%%%%%%%%%%%%%%%%%%%%%%
21 %
22 satmod=2;           % Satellite model to use for 3-D plots (1=GPS, 2=Hubble)
23 pltflg1=0;         % Turn momentum ellipsoid plots on/off (1/0)
24   ellflg=1;        % Select momentum ellipsoid plotting method and resolution
25   inc0=.05;        %   0=achievable regions of ellipsoid, point-by-point (slow)
26   inc1=3;          %   1=entire ellipsoid, parameterized method (fast)
27 pltflg2=0;         % Turn dimen. momenta, ang. veloc. plots on/off (1/0)
28 pltflg3=0;         % Turn non-dimen. momenta, ang. vel. plots on/off (1/0)
29 pltflg4=1;         % Turn 3-D attitude plots on/off (1/0)
30 pertflg=1;         % Turn grav. grad. and sol. press. torques on/off
31                   %   0 =none  1 =sol. press. only  2 =sol. press. and grav.
32 small=.5;         % Value of small parameter on torques. Should be (+)
33 r=0;               % Momentum wheel triads to use
34                   %   0 = (1/2/3), 1 = (1/2/4), 2 = (1/3/4), 3 = (2/3/4)
35 ph_o=0;            % Initial Euler angle phi   about e3 axis (deg)
36 th_o=0;            % Initial Euler angle theta about e1 axis (deg)
37 ps_o=0;            % Initial Euler angle psi   about e3 axis (deg)
38                   %
39 ph_f=0;            % Final Euler angle phi   about e3 axis (deg)
40 th_f=90;           % Final Euler angle theta about e1 axis (deg)
41 ps_f=0;            % Final Euler angle psi   about e3 axis (deg)
42                   %
43 h_o=200;           % Magnitude of vehicle ang. momentum (constant) [kg*m^2/s]
44                   %   used to dimensionalize results. Note that since vehicle

```



```

45          % ang. vel. are ~0, larger h_0 <--> higher rotor momenta;
46 mu_o=[1 0 0]; % Initial non-dimen. rotor momenta (stationary platform)
47          % format: mu_o=[mu1 mu2 mu3]
48          % use mu_o=-99 to generate random point
49 ths0=135;    % Initial sun vector angle from e1 (CCW, in degrees)
50 traj=2;     % Wheel torque trajectory
51          % (1=direct 2=suboptimal)
52 t0=0;       % Start time for integration (sec). Use -999 for autocalc.
53 tf=-999;   % Stop time for integration (sec). Use -999 for autocalc.
54          % NOTE: non-dimen. values calc. below s/c properties
55 num=20;    % desired number of 3-D attitude plots for this time span
56 %
57 %
58 %%%%%%%%%%%%%%%%%%%%%%%%%%%%%%%%%%%%%%%%%%%%%%%%%%%%%%%%%%%%%%%%%%%%%%%%%%
59 %%%SPACECRAFT PHYSICAL PROPERTIES%%
60 %%%%%%%%%%%%%%%%%%%%%%%%%%%%%%%%%%%%%%%%%%%%%%%%%%%%%%%%%%%%%%%%%%%%%%%%%%
61 %
62 % The Hubble Space Telescope is modeled as two right circular cylinders
63 % of uniform density, with two rectangular parallelepiped
64 % solar arrays at equal distances from s.c. c.m.
65 %
66 % there are four axisymmetric momentum wheels
67 %
68 a1=[sqrt(2)/2; 0; -sqrt(2)/2]; % wheel orientation w.r.t
69 a2=[0; -sqrt(2)/2; -sqrt(2)/2]; % body fixed frame b )
70 a3=[-sqrt(2)/2; 0; -sqrt(2)/2];
71 a4=[0; sqrt(2)/2; -sqrt(2)/2];
72 Is1=.84; % Axial moments of inertia of the
73 Is2=.84; % 4 momentum wheels (kg*m^2)
74 Is3=.84;
75 Is4=.84;
76 ws1max=3000*2*pi/60; % Max. wheel ang. speed magnitudes (rad/s)
77 ws2max=3000*2*pi/60;
78 ws3max=3000*2*pi/60;
79 ws4max=3000*2*pi/60;
80 m_tot=24000/2.204622622; % HST total mass (lb)
81 r_sm=1.5; % Radius of small cylinder (m)
82 h_sm=4; % Height of small cylinder (m)
83 r_lg=2; % Radius of large cylinder (m)
84 h_lg=5; % Height of large cylinder (m)
85 h_sa=8; % Height of each solar array (m)
86 w_sa=2; % Width of each solar array (m)
87 d_sa=.05; % Thickness of each solar array (m)
88 rho_d=.3; % Spacecraft surface diffuse reflectivity
89 rho_s=.4; % Spacecraft surface specular reflectivity

```

```

90 %
91 gps_sa_m2a=6.125; % GPS IIR solar array mass/area ratio
92 m_sa=h_sa*w_sa*gps_sa_m2a; % Mass of each HST solar array (kg)
93 m_sc=m_tot-2*m_sa; % Mass of HST without solar arrays (kg)
94 vol_sm=pi*r_sm^2*h_sm; % Volume of small cylinder (m^3)
95 vol_lg=pi*r_lg^2*h_lg; % Volume of large cylinder (m^3)
96 frac_sm=vol_sm/(vol_sm+vol_lg); % Fraction of total volume from small cyl.
97 m_sm=frac_sm*m_sc; % Mass of small cylinder (kg)
98 m_lg=m_sc-m_sm; % Mass of large cylinder (kg)
99 %
100 d=[m_sm m_lg 2*m_sa; 1 -1 0; 0 -1 1]\[0;(h_sm+h_lg)/2;h_lg/2];
101 R_sm=[0 0 d(1)]; % Vectors (in b frame) from system c.m.
102 R_lg=[0 0 d(2)]; % to small and large cylinder c.m. (m)
103 R_s1=[0 4 d(3)]; % and solar array c.m.
104 R_s2=[0 -4 d(3)];
105 %
106 I_sm=eye(3); % Inertia matrix for small cylinder about
107 I_sm(1,1)=(3*r_sm^2+h_sm^2)/12; % center of mass, expressed in b frame
108 I_sm(2,2)=I_sm(1,1); % (kg*m^2)
109 I_sm(3,3)=r_sm^2/2;
110 I_sm=m_sm*I_sm;
111 %
112 I_lg=eye(3); % Inertia matrix for large cylinder about
113 I_lg(1,1)=(3*r_lg^2+h_lg^2)/12; % center of mass, expressed in b frame
114 I_lg(2,2)=I_lg(1,1); % (kg*m^2)
115 I_lg(3,3)=r_lg^2/2;
116 I_lg=m_lg*I_lg;
117 %
118 I_sa=eye(3);
119 I_sa(1,1)=(h_sa^2+w_sa^2)/12; % Inertia matrix for solar array about
120 I_sa(2,2)=(h_sa^2+d_sa^2)/12; % center of mass, expressed in b frame
121 I_sa(3,3)=(d_sa^2+w_sa^2)/12; % (kg*m^2)
122 I_sa=m_sa*I_sa;
123 %
124 R_smx=[ 0 -R_sm(3) R_sm(2); % Skew symmetrix matrix for translating
125 R_sm(3) 0 -R_sm(1); % I_sm to system c.m.
126 -R_sm(2) R_sm(1) 0];
127 R_lgx=[ 0 -R_lg(3) R_lg(2); % Skew symmetrix matrix for translating
128 R_lg(3) 0 -R_lg(1); % I_lg to system c.m.
129 -R_lg(2) R_lg(1) 0];
130 R_s1x=[ 0 -R_s1(3) R_s1(2); % Skew symmetrix matrix for translating
131 R_s1(3) 0 -R_s1(1); % I_sa1 to system c.m.
132 -R_s1(2) R_s1(1) 0];
133 R_s2x=[ 0 -R_s2(3) R_s2(2); % Skew symmetrix matrix for translating
134 R_s2(3) 0 -R_s2(1); % I_sa2 to system c.m.

```

```

135     -R_s2(2) R_s2(1) 0];
136 I_sm_c=I_sm-m_sm*R_smx*R_smx; % Translate inertia matrix to system
137 I_lg_c=I_lg-m_lg*R_lgx*R_lgx; % center of mass, in b frame
138 I_sa1_c=I_sa-m_sa*R_s1x*R_s1x;
139 I_sa2_c=I_sa-m_sa*R_s2x*R_s2x;
140 I=I_sm_c+I_lg_c+I_sa1_c+I_sa2_c; % Construct total inertia matrix about
141 % c.m. in b frame
142 Ic=trace(I); % Charac. inertia for non-dimensionalizing
143 % (note: this is frame invariant)
144 I_d=I; % dimensional inertia matrix
145 I=I./Ic; % Non dimensionalized inertia matrix
146 %
147 Is_d=eye(3); % Create diagonal matrix template;
148 Is_d(1,1)=Is1; % Default Configuration (r=0);
149 Is_d(2,2)=Is2;
150 Is_d(3,3)=Is3;
151 if r==1 % Fill remaining diagonal entries of Is
152     Is_d(3,3)=Is4; % Based on choice of wheel combination.
153 elseif r==2
154     Is_d(2,2)=Is3;
155     Is_d(3,3)=Is4;
156 elseif r==3
157     Is_d(1,1)=Is2;
158     Is_d(2,2)=Is3;
159     Is_d(3,3)=Is4;
160 end;
161 %
162 Is=Is_d./Ic; % Non dimensionalized inertia of wheels
163 %
164 % Now define vectors from vehicle c.m. to component centers
165 % of pressure for solar pressure modeling (m), the effective areas (m^2)
166 % and the surface normal vectors (all in Fb)
167 %
168 rs(1,:)= [0 0 0]; % small cylinder. Dummy value, calc. during integr.
169 rs(2,:)= [0 0 0]; % large cylinder. Dummy value, calc. during integr.
170 rs(3,:)= R_sm+[0 0 h_sm/2]; % small cylinder top
171 rs(4,:)= R_lg+[0 0 -h_lg/2]; % large cylinder bottom
172 rs(5,:)= R_s1; % +b2 solar array FRONT
173 rs(6,:)= R_s2; % -b2 solar array FRONT
174 rs(7,:)= R_s1; % +b2 solar array BACK
175 rs(8,:)= R_s2; % -b2 solar array BACK
176 rs(9,:)= [0 0 0]; % dummy value, no 9th surface
177 rs(10,:)= [0 0 0]; % dummy value, no 10th surface
178 As(1)=2*r_sm*h_sm;
179 As(2)=2*r_lg*h_lg;

```

```

180 As(3)=pi*r_sm^2;
181 As(4)=pi*r_lg^2;
182 As(5)=h_sa*w_sa;
183 As(6)=h_sa*w_sa;
184 As(7)=h_sa*w_sa;
185 As(8)=h_sa*w_sa;
186 As(9)=0;
187 As(10)=0;
188 ns(1,:)= [0 0 0]; % small cylinder. Dummy value, calc. during integration
189 ns(2,:)= [0 0 0]; % large cylinder. Dummy value, calc. during integration
190 ns(3,:)= [0 0 1];
191 ns(4,:)= [0 0 -1];
192 ns(5,:)= [1 0 0];
193 ns(6,:)= [1 0 0];
194 ns(7,:)= [-1 0 0];
195 ns(8,:)= [-1 0 0];
196 ns(9,:)= [0 0 0];
197 ns(10,:)= [0 0 0];
198 %
199 %
200 %%%%%%%%%%%%%%%%%%%%%%%%%%%%%%%%%%%%%%%%%%%%%%%%%%%%%%%%%%%%%%%%%%%%%%%%%%
201 %%%%%%%%% ORBITAL PARAMETERS %%%%%%%%%
202 %%%%%%%%%%%%%%%%%%%%%%%%%%%%%%%%%%%%%%%%%%%%%%%%%%%%%%%%%%%%%%%%%%%%%%%%%%
203 %
204 % Note: right ascension of the node is assumed to be 0,
205 % and the argument of perigee is assumed to be pi/2
206 %
207 sma=6993.135; % Semi-major axis (km)
208 ecc=0.001; % Eccentricity
209 incl=deg2rad(45); % Inclination (degrees)
210 %
211 %
212 %%%%%%%%%%%%%%%%%%%%%%%%%%%%%%%%%%%%%%%%%%%%%%%%%%%%%%%%%%%%%%%%%%%%%%%%%%
213 %%%%%%%%% NON-DIMENSIONALIZE TIMES %%%%%%%%%
214 %%%%%%%%%%%%%%%%%%%%%%%%%%%%%%%%%%%%%%%%%%%%%%%%%%%%%%%%%%%%%%%%%%%%%%%%%%
215 %
216 % This is necessary for equation consistency for integration
217 % Must be done here since Ic needed from above
218 %
219 t0=h_o*t0/Ic;
220 if tf>0, tf=h_o*tf/Ic; end; % don't recalculate if tf=-999

```

D.3 Main Simulation Program

```
1  %%%%%%%%%%%%%%%%%%%%%%%%%%%%%%%%%%%%%%%%%%%%%%%%%%%%%%%%%%%%%%%%%%%%%%%%%%
2  %%%                                                                    %%%
3  %%%          rotor_m.m                                                %%%
4  %%%                                                                    %%%
5  %%%          Capt Greg Schultz, GA-95D                                %%%
6  %%%                                                                    %%%
7  %%%          revision                                                %%%
8  %%%          -----                                                %%%
9  %%%          11.02.95.1230                                           %%%
10 %%%                                                                    %%%
11 %%%%%%%%%%%%%%%%%%%%%%%%%%%%%%%%%%%%%%%%%%%%%%%%%%%%%%%%%%%%%%%%%%%%%%%%%%
12 %
13 clear;
14 format short e;                % display format
15 global I_d Ic Is_d h_o JI small; % Define global variables used
16 global A B a1a1 a1a2 a2a2;     % here and in subroutines
17 global mu_o mu_f Rgmu Rdmu;
18 global r direct wsmax ellflg GM;
19 global rho_d rho_s;
20 global rs ns As r_sm r_lg R_sm R_lg satmod pertflg;
21 %
22 File=input('Data file (in single quotes w/o .m extension, e.g. dat_def:');
23 %
24 eval(File);                    % Execute file to load data for simulation
25 %
26 %attpos=[0 25 1200 900];      % Use this for presentations
27 attpos=[0 100 700 700];      % [Xo Yo Xwidth Ywidth] pixels
28 %
29 if r==0                        % Calculate A and wsmax based on wheels
30     A=[a1 a2 a3];             % selected to use in simulation
31     wsmax=[ws1max ws2max ws3max];
32 elseif r==1
33     A=[a1 a2 a4];
34     wsmax=[ws1max ws2max ws4max];
35 elseif r==2
36     A=[a1 a3 a4];
37     wsmax=[ws1max ws3max ws4max];
38 elseif r==3
39     A=[a2 a3 a4];
40     wsmax=[ws2max ws3max ws4max];
41 end;
42 a1=A(:,1); a2=A(:,2); a3=A(:,3); % redefine a1..a3 for subsequent calcs.
43 %
44 if rank(A)<3
```

```

45   ' Wheel unit vectors do not form a basis - modify data input file'
46   break;
47   end;
48   %
49   %%%%%%%%%%%%%%%%%%%%%%%%%%%%%%%%%%%%%%%%%%%%%%%%%%%%%%%%%%%%%%%%%%%%%%%%%
50   %%%%%%   SPECIFY INITIAL AND FINAL CONDITIONS   %%%%%%
51   %%%%%%%%%%%%%%%%%%%%%%%%%%%%%%%%%%%%%%%%%%%%%%%%%%%%%%%%%%%%%%%%%%%%%%%%%
52   %
53   % Convert initial, final Euler angles to radians
54   %
55   ph_o=deg2rad(ph_o); th_o=deg2rad(th_o); ps_o=deg2rad(ps_o);
56   ph_f=deg2rad(ph_f); th_f=deg2rad(th_f); ps_f=deg2rad(ps_f);
57   %
58   % Obtain rotation matrices Ro, Rf relating initial, desired final
59   % position of body frame to inertial.
60   %
61   Ro=rot3(ps_o)*rot1(th_o)*rot3(ph_o); % xo|b=Ro*xo|i
62   Rf=rot3(ps_f)*rot1(th_f)*rot3(ph_f); % xf|b=Rf*xf|i
63   %
64   % calculate initial Euler axis (lambda) and rotation angle (m)
65   %
66   [eigvec,eigval]=eig(Ro);
67   if abs(1-eigval(1,1))<=.001
68     lambda=eigvec(:,1);
69     m=angle(eigval(2,2));
70   elseif abs(1-eigval(2,2))<=.001
71     lambda=eigvec(:,2);
72     m=angle(eigval(1,1));
73   elseif abs(1-eigval(3,3))<=.001
74     lambda=eigvec(:,3);
75     m=angle(eigval(1,1));
76   else
77     error('CANNOT FIND EULER AXIS - No eigenvalue close to 1')
78   end;
79   m=abs(m); % take pos. rotations about euler axis
80   %
81   q10=lambda(1)*sin(m/2); % calculate initial quaternions
82   q20=lambda(2)*sin(m/2);
83   q30=lambda(3)*sin(m/2);
84   q40=cos(m/2);
85   q0=[q10 q20 q30 q40];
86   %
87   if mu_o==--99 % generate random mu_o if desired
88     xx=rand(size(1:3));
89     x_o=xx/norm(xx);

```

```

90   mu_o=inv(A)*x_o';
91   end;
92   %
93   if size(mu_o,1)==1, mu_o=mu_o'; end;
94   %
95   mu_f=inv(A)*Rf*Ro'*A*mu_o;           % calc. mu_f based on init., desired
96                                       % final orientations
97   %
98   x_o=A*mu_o;
99   x_f=A*mu_f;
100  'Dimensionless s/c ang. mom. (stationary platform) boundary conditions are:'
101  x_o
102  x_f
103  'Dimensionless wheel ang. mom. (stationary platform) boundary conditions are:'
104  mu_o
105  mu_f
106  'Initial wheel angular velocities (rad/sec):'
107  wso=inv(Is*Ic)*h_o*mu_o
108  %
109  J=I-A*Is*A'; JI=inv(J);
110  %
111  % Calculate initial orbital position, velocity
112  % (assuming right ascension=0, arg per=pi/2)
113  %
114  if pertflg>0
115     GM=398601.2;                       % Gravitational parameter
116     rper=sma*(1-ecc);                   % Radius of perigee
117     enr=-GM/(2*sma);                    % Orbital energy
118     Rorb0=[0 rper*cos(incl) rper*sin(incl)]; % Initial orbital position
119     Vorb0=[-(2*(enr+GM/rper))^0.5 0 0]; % Initial orbital velocity
120     TP=2*pi*(sma^1.5)/(GM^.5);
121  end;
122  %
123  ths0=deg2rad(ths0);      % convert initial sun angle to rad
124  %
125  %%%%%%%%%%%%%%%%%%%%%%%%%%%%%%%%%%%%%%%%%%%%%%%%%%%%%%%%%%%%%%%%%%%%%%%%%%%
126  %%%%% CALCULATE DIRECT WHEEL TORQUE CONTROL %%%%%
127  %%%%%%%%%%%%%%%%%%%%%%%%%%%%%%%%%%%%%%%%%%%%%%%%%%%%%%%%%%%%%%%%%%%%%%%%%%%
128  %
129  if traj==1
130     direct=small*((mu_f-mu_o)/(norm(mu_f-mu_o)));
131     if tf==-999
132        tf=(norm(mu_f-mu_o))/small;      % auto-calculate final time for
133        end;                             % desired final condition mu_f
134  end;

```

```

135 %
136 %%%%%%%%%%%%%%%%%%%%%%%%%%%%%%%%%%%%%%%%%%%%%%%%%%%%%%%%%%%%%%%%%%%%%%%%%%
137 %%% CALCULATE SUBOPTIMAL WHEEL TORQUE CONTROL %%%
138 %%%%%%%%%%%%%%%%%%%%%%%%%%%%%%%%%%%%%%%%%%%%%%%%%%%%%%%%%%%%%%%%%%%%%%%%%%
139 %
140 % define new gi frame in which origin, mu_o, mu_f lie in g1-g2 plane
141 % this is a suboptimal trajectory NEAR to the "great circle"
142 % trajectory on a sphere. Approximation is best when ellipsoid is
143 % nearly spherical (rotors nearly orthogonal).
144 % Only limitation is must have non-zero cross prod. between mu_o and mu_f
145 %
146 if traj==2
147     g1=mu_o/norm(mu_o);
148     g3=cross(mu_o,mu_f)/(norm(cross(mu_o,mu_f)));
149     g2=cross(g3,g1)/norm(cross(g3,g1));
150     Rgmu=[g1 g2 g3]; % rot. matrix from g to "mu" frame
151     AG=A*Rgmu;
152     ag1=AG(:,1); ag2=AG(:,2); ag3=AG(:,3);
153     a1a1=ag1'*ag1; a2a2=ag2'*ag2; a1a2=ag1'*ag2;
154     B=[a1a2 a2a2 0;-a1a1 -a1a2 0;0 0 0]; % Wheel torque in "nu" frame
155     %
156     % auto-calculate final time for desired final condition mu_f
157     %
158     if tf== -999
159         B1=[a1a2 a2a2;-a1a1 -a1a2]; % Two rotor torque law in gi frame
160         nu_f=Rgmu'*mu_f; % rotor momenta in gi frame
161         nu_f=nu_f(1:2); % in gi frame, nu_f(3)=0 anyway
162         [v1,d1]=eig(B1);
163         Pb1=[real(v1(:,1)) imag(v1(:,1))];
164         w1=imag(d1(1,1));
165         ab1=Pb1\ [1;0];
166         aa1=ab1(1); b1=ab1(2);
167         vv1=Pb1\nu_f;
168         v11=vv1(1); v12=vv1(2);
169         tf=atan2(b1*v11-aa1*v12, aa1*v11+b1*v12)/(w1*small);
170         if tf<0, tf=-tf; end;
171     end;
172 end;
173 %
174 %%%%%%%%%%%%%%%%%%%%%%%%%%%%%%%%%%%%%%%%%%%%%%%%%%%%%%%%%%%%%%%%%%%%%%%%%%
175 %%% INTEGRATE EQUATIONS OF MOTION %%%
176 %%%%%%%%%%%%%%%%%%%%%%%%%%%%%%%%%%%%%%%%%%%%%%%%%%%%%%%%%%%%%%%%%%%%%%%%%%
177 %
178 t0_d=Ic*t0/h_o; % dimensionalize integration times
179 tf_d=Ic*tf/h_o;

```



```

180 'integration time (sec):'
181 t0_d
182 tf_d
183 %
184 if pertflg>0
185     'Number of orbital periods spanned by this maneuver : '
186     tf_d/TP
187 end;
188 %             unperturbed RHS file, tolerances, i.c.s
189 if pertflg==0
190     if traj==1,         File='rotor_e1';
191         elseif traj==2, File='rotor_e2';
192     end;
193     tol=1e-10
194     states0=[x_o' mu_o' q0];
195     [t,states]=ode45(File,t0,tf,states0,tol,0);
196 end;
197 %             perturbed RHS file, tolerances, i.c.s
198 if pertflg>0
199     if traj==1,         File='rotor_e1_per';
200         elseif traj==2, File='rotor_e2_per';
201     end;
202     tol=1e-10
203     states0=[x_o' mu_o' q0 ths0 Rorb0 Vorb0];
204     [t,states]=ode45(File,t0,tf,states0,tol,0);
205 end;
206 %
207 % integration is now done, so let's redefine returned
208 % state variables with more recognizable names
209 %
210 % These are returned for both perturbed and unperturbed system
211 %
212 x1 =states(:,1); x2=states(:,2); x3=states(:,3); x=[x1 x2 x3];
213 mu1=states(:,4); mu2=states(:,5); mu3=states(:,6); mu=[mu1 mu2 mu3];
214 q1 =states(:,7); q2=states(:,8); q3=states(:,9); q4=states(:,10);
215 %
216 % These only returned if perturbations turned on
217 %
218 if pertflg>0
219     ths=[states(:,11)]; % sun vector angle from e1 in Fi
220     Rorb=[states(:,12) states(:,13) states(:,14)]; % Orb position in Fi
221     Vorb=[states(:,15) states(:,16) states(:,17)]; % Orb velocity in Fi
222 end;
223 %
224 R11=q1.^2-q2.^2-q3.^2+q4.^2; % Calculate rotation matrix

```

```

225 R12=2*(q1.*q2+q3.*q4);           % relating body axes to inertial
226 R13=2*(q1.*q3-q2.*q4);           % for each time step
227 R21=2*(q1.*q2-q3.*q4);           % (x|b)=R(x|i)
228 R22=-q1.^2+q2.^2-q3.^2+q4.^2;    %      =R3(psi)R1(theta)R3(phi)(x|i)
229 R23=2*(q1.*q4+q2.*q3);
230 R31=2*(q1.*q3+q2.*q4);
231 R32=2*(-q1.*q4+q2.*q3);
232 R33=-q1.^2-q2.^2+q3.^2+q4.^2;
233 %
234 %
235 b1=[R11 R12 R13];                 % Now we can calculate body axis vectors
236 b2=[R21 R22 R23];                 % vs. time (expressd in Fi). These should
237 b3=[R31 R32 R33];                 % be orthogonal and of unit length
238 %
239 stln=size(R11,1);                  % Length of state vector
240 %
241 Rfin=[R11(stln) R12(stln) R13(stln); % final transf. matrix
242        R21(stln) R22(stln) R23(stln);
243        R31(stln) R32(stln) R33(stln)];
244 %
245 sun=[cos(th) sin(th) 0*th];        % sun vector in Fi
246 t_d=Ic*t/h_o;                       % time (sec)
247 h_d1=h_o*x1; h_d2=h_o*x2; h_d3=h_o*x3; % platform ang. mom. (N*m*s)
248 ha_d1=h_o*mu1; ha_d2=h_o*mu2; ha_d3=h_o*mu3; % wheel ang. mom. (N*m*s)
249 ws_d1=ha_d1/Is_d(1,1);               % wheel speed (rad/sec)
250 ws_d2=ha_d2/Is_d(2,2);
251 ws_d3=ha_d3/Is_d(3,3);
252 %
253 w=JI*(x'-A*mu'); % Calc. platform non-dim. angular velocities (body frame)
254 w_d=h_o*w/Ic; % Calc. dimensional platform ang. vel. (rad/sec) (body frame)
255 Hp=I*w; Hp=Hp'; % Calc. platform non-dim. momentum (body frame)
256 Hr=mu*A'; % Calc. rotor non-dim. momentum (body frame)
257 Htot=Hp+Hr; % Vehicle total non-dim. ang. momentum (body frame)
258 for ii=1:stln % Vehicle total non-dim. ang. momentum (inertial frame)
259 % x'|i=x'|b*R313
260 xi(ii,:)=x(ii,:)*[R11(ii) R12(ii) R13(ii);
261                  R21(ii) R22(ii) R23(ii);
262                  R31(ii) R32(ii) R33(ii)];
263 end;
264 %
265 for ii=1:stln % Mag. of total ang. momentum (should be const.)
266 Hmag(ii)=norm(Htot(ii,:));
267 end;
268 %
269 % check quaternions for errors noting that q1^2+q2^2+q3^2+q4^2=1

```

```

270 %
271 qq=q1.^2+q2.^2+q3.^2+q4.^2;
272 'Variation in quaternions ='
273 qvar=abs(max(qq)-min(qq))
274 %
275 'Variance of magnitude of total angular momentum ='
276 Hmag_var=max(Hmag)-min(Hmag)
277 %
278 'Maximum wheel angular velocities (rad/s) ='
279 ws_d1_max=max(abs(ws_d1))
280 ws_d2_max=max(abs(ws_d2))
281 ws_d3_max=max(abs(ws_d3))
282 %
283 'Maximum vehicle angular velocity (rad/sec) ='
284 w_max=max(max(abs(w_d)))
285 %
286 'Final spacecraft angular velocities (rad/sec) ='
287 w_d(:,stln)'
288 %
289 'Final Euler angles (deg) ='
290 %
291 phi_f=rad2deg(atan2(Rfin(3,1),-Rfin(3,2))) % Final Euler angles
292 theta_f=rad2deg(real(acos(Rfin(3,3))))
293 psi_f=rad2deg(atan2(Rfin(1,3),Rfin(2,3)))
294 %
295 %%%%%%%%%%%%%%%%%%%%%%%%%%%%%%%%%%%%%%%%%%%%%%%%%%%%%%%%%%%%%%%%%%%%%%%%%%
296 %%%%%%%%% PLOT RESULTS OF INTEGRATION %%%%%%%%%
297 %%%%%%%%%%%%%%%%%%%%%%%%%%%%%%%%%%%%%%%%%%%%%%%%%%%%%%%%%%%%%%%%%%%%%%%%%%
298 %
299 % plot momentum ellipsoid if desired
300 %
301 if pltflg==1
302     if ellflg==0
303         ell_plt0(a1,a2,a3,-2,2,-2,2,inc0);
304     elseif ellflg==1
305         ell_plt1(a1,a2,a3,inc1);
306     end;
307     figure(1);
308     hold on;
309     plot3(mu_o(1),mu_o(2),mu_o(3),'wo');
310     plot3(mu_f(1),mu_f(2),mu_f(3),'wx');
311     plot3(mu1,mu2,mu3,'w-');
312     hold off;
313     figure(2);
314     hold on;

```

```

315     plot3(x_o(1),x_o(2),x_o(3),'wo');
316     plot3(x_f(1),x_f(2),x_f(3),'wx');
317     plot3(x1,x2,x3,'w-');
318     hold off;
319 end;
320 %
321 % Plot dimensional momenta and angular velocities if desired
322 %
323 if pltflg2==1
324     figure;
325     plot(t_d,h_d1,'w-',t_d,h_d2,'w-.',t_d,h_d3,'w:');
326     legend('h1','h2','h3');
327     title('Spacecraft Angular Momentum vs. time');
328     xlabel('Time (seconds)'); ylabel('h (kg*m^2/s)');
329     figure;
330     plot(t_d,ha_d1,'w-',t_d,ha_d2,'w-.',t_d,ha_d3,'w:');
331     legend('ha1','ha2','ha3');
332     title('Wheel Angular Momentum vs. time');
333     xlabel('Time (seconds)'); ylabel('ha (kg*m^2/s)');
334     figure;
335     plot(t_d,h_o*Hmag);
336     title('Total Angular Momentum Magnitude vs. time');
337     xlabel('Time (seconds)'); ylabel('|h|');
338     figure;
339     plot(t_d,ws_d1,'w-',t_d,ws_d2,'w-.',t_d,ws_d3,'w:');
340     legend('ws1','ws2','ws3');
341     title('Wheel angular velocities vs. time');
342     xlabel('Time (seconds)'); ylabel('ws (rad/sec)');
343     figure;
344     plot(t_d,w_d(1,:), 'w-',t_d,w_d(2,:), 'b-.',t_d,w_d(3,:), 'r:');
345     legend('w1','w2','w3');
346     title('Spacecraft angular velocities vs. time');
347     xlabel('Time (seconds)'); ylabel('w (rad/sec)');
348 end;
349 %
350 % Plot non-dimensional momenta and angular velocities if desired
351 %
352 if pltflg3==1
353     figure;
354     plot(t,x1,'w-',t,x2,'w-.',t,x3,'w:');
355     legend('x1','x2','x3');
356     title('Dimensionless Total Angular Momentum vs. time (in Fb)');
357     xlabel('Time (non-dimensional)'); ylabel('x');
358     figure;
359     plot(t,mu1,'w-',t,mu2,'w-.',t,mu3,'w:');

```

```

360     legend('mu1','mu2','mu3');
361     title('Dimensionless Wheel Angular Momentum vs. time');
362     xlabel('Time'); ylabel('mu');
363     figure;
364     plot(t_d,xi(:,1),'w-',t_d,xi(:,2),'w-.',t_d,xi(:,3),'w:');
365     legend('xi1','xi2','xi3');
366     title('Dimensionless Total Ang. Mom. Components vs. Time (in Fi)');
367     xlabel('Time (seconds)'); ylabel('xi');
368     figure;
369     plot(t,Hmag);
370     title('Dimensionless Total Angular Momentum Magnitude vs. time');
371     xlabel('Time (seconds)'); ylabel('|x|');
372     figure;
373     plot(t,w(1,:), 'w-',t,w(2,:), 'b-',t,w(3,:), 'r-');
374     legend('w1','w2','w3');
375     title('Dimensionless Spacecraft angular velocities vs. time');
376     xlabel('Time'); ylabel('w');
377     end;
378     %
379     % Plot vehicle attitude during maneuver
380     %
381     if pltflg4==1
382         %
383         % now let's plot body axes relative to inertial axes vs. time
384         %
385         rows=stln;
386         for i=1:rows
387             if t(i)<=t0, imin=i; end;    % set starting index to correspond to t0
388             end;
389             for i=1:rows
390                 if t(i)<=tf, imax=i; end;    % set vector index to correspond to tf
391                 end;
392                 if imax<2, imin=1; imax=2; end;
393                 incr=round((imax-imin)/num); % increment for vector index during plot
394                 if incr<1, incr=1; end;
395                 plot_timestep=t(incr)    % display time step for reference
396                 %
397                 % create vectors defining the polygon representing the satellite
398                 %
399                 if satmod==1    % GPS Blk IIR model
400                     %
401                     % X component of vertices
402                     %
403                     XXv=[ 1 1 1 1 1;    % face +b1
404                         -1 -1 -1 -1 -1;    % face -b1

```

```

405 1 -1 -1 1 1;          % face +b2
406 1 -1 -1 1 1;          % face -b2
407 1 1 -1 -1 1;         % face +b3 Earth pointing
408 1 1 -1 -1 1];        % face -b3
409 %
410 XXs=[ 0 0 0 0 0;      % +b2 solar array
411 0 0 0 0 0];          % -b2 solar array
412 %
413 % Y component of vertices
414 %
415 YYv=[ -1 1 1 -1 -1;
416 -1 1 1 -1 -1;
417 1 1 1 1 1;
418 -1 -1 -1 -1 -1;
419 -1 1 1 -1 -1;
420 -1 1 1 -1 -1];
421 %
422 YYs=[ 2 5 5 2 2;
423 -2 -5 -5 -2 -2];
424 %
425 % Z component of vertices
426 %
427 ZZv=[ -1 -1 1 1 -1;
428 -1 -1 1 1 -1;
429 -1 -1 1 1 -1;
430 -1 -1 1 1 -1;
431 1 1 1 1 1;
432 -1 -1 -1 -1 -1];
433 %
434 ZZs=[ -.5 -.5 .5 .5 -.5;
435 -.5 -.5 .5 .5 -.5];
436 %
437 elseif satmod==2      % Hubble Telescope model
438 [XXv,YYv,ZZv]=cylinder([1*ones(1,10) .8*ones(1,8)],20);
439 ZZv=ZZv-.5;          % Move origin down b3 to c.m.
440 ZZv=6.*ZZv;          % Stretch along b3 axis
441 XXs=[ 0 0 0 0 0;      % +b2 solar array
442 0 0 0 0 0];          % -b2 solar array
443 YYs=[ 1.2 2.2 2.2 1.2 1.2;
444 -1.2 -2.2 -2.2 -1.2 -1.2];
445 ZZs=[ -3 -3 3 3 -3;
446 -3 -3 3 3 -3];
447 SS=[1 0 0];          % vector for Sun direction

448 end;

```

```

449 %
450 XXvrow=size(XXv,1); XXvcol=size(XXv,2);
451 XXsrow=size(XXs,1); XXscol=size(XXs,2);
452 %
453 i=imin;
454 loopflg1=0; % flag to break out of while loop when
455 while loopflg1==0 % imax plotted.
456     if i>imax % ensure attitude at tf is plotted
457         i=imax;
458         loopflg1=1;
459     end;
460 %
461 Rbi=[b1(i,:) b2(i,:) b3(i,:)]'; % rot. matrix relating Fb to Fi
462 % x|i=Rbi*x|b
463 %
464 % rotate vehicle model
465 %
466 for row=1:XXvrow
467     for col=1:XXvcol
468         y=Rbi*[XXv(row,col); YYv(row,col); ZZv(row,col)];
469         Xv(row,col)=y(1); Yv(row,col)=y(2); Zv(row,col)=y(3);
470     end;
471 end;
472 %
473 % rotate array model
474 %
475 for row=1:XXsrow
476     for col=1:XXscol
477         y=Rbi*[XXs(row,col); YYs(row,col); ZZs(row,col)];
478         Xs(row,col)=y(1); Ys(row,col)=y(2); Zs(row,col)=y(3);
479     end;
480 end;
481 CCv='m'; CCs='b'; % color s/c magenta, arrays blue
482 figure; % Open new figure for attitude plot
483 set(gcf,'Position',attpos);
484 hold on;
485 if satmod==1 % GPS IIR Model plot
486     fill3(Xv',Yv',Zv',CCv); % plot satellite model
487     fill3(Xs',Ys',Zs',CCs); % plot solar arrays
488 %
489 elseif satmod==2 % Hubble model plot
490     surf1(Xv,Yv,Zv,SS); % plot satellite model
491     colormap copper;
492     shading faceted;
493     brighten(.5);

```

```

494     fill3(Xs',Ys',Zs',CCs);           % plot solar arrays
495     end;
496     %
497     lineft([0 0 0],[0 8 0],1,'y');     % plot Fi axes
498     lineft([0 0 0],[0 0 8],1,'y');
499     lineft([0 0 0],[8 0 0],1,'y');
500     text([8.5;0;0],[0;8.5;0],[0;0;8.5],['I';'J';'K']); % label Fi axes
501     %
502     lineft([0 0 0],5*xi(i,:),2,'r');   % plot total angular momentum
503     text(6*xi(i,1),6*xi(i,2),6*xi(i,3),'h'); % Label h vector
504     %
505     if pertflg>0
506         lineft([7.8 0 2],[7.8 0 2]+2*sun(i,:),2,'w'); % plot sun vector
507         text(8.5,0,2,'Sun');          % label sun vector
508     end;
509     %
510     lineft(b1(i,:),5.4*b1(i,:),1,'g'); % plot Fb axes
511     lineft(b2(i,:),5.4*b2(i,:),1,'g');
512     if satmod==1                       % plot solar array booms
513         lineft(b2(i,:),2*b2(i,:),2,'g');
514         lineft(-b2(i,:),-2*b2(i,:),2,'g');
515     elseif satmod==2
516         lineft(b2(i,:),1.2*b2(i,:),2,'g');
517         lineft(-b2(i,:),-1.2*b2(i,:),2,'g');
518     end;
519     lineft(b3(i,:),5.4*b3(i,:),1,'g');
520     text(6*b1(i,1),6*b1(i,2),6*b1(i,3),'b1'); % label body axes
521     text(6*b2(i,1),6*b2(i,2),6*b2(i,3),'b2');
522     text(6*b3(i,1),6*b3(i,2),6*b3(i,3),'b3');
523     %
524     axis([-6 6 -6 6 -6 6]);
525     axis off;
526     view(130,20);
527     if satmod==1, title('GPS IIR Attitude Model');
528     elseif satmod==2, title('Hubble Space Telescope Attitude Model');
529     end;
530     tstring=num2str(t_d(i));           % convert current time to string
531     text(-5,0,5.95,'time (sec)'); text(-5,0,5.2,tstring);
532     i=i+incr;
533     end;
534     maxfig=gcf;                       % Get last figure handle
535     end;

```


D.4 Unperturbed Direct Control Law Equations

```

1 function statedot=rotor_e1(t,state)
2 %
3 %%%%%%%%%%%%%%%%%%%%%%%%%%%%%%%%%%%%%%%%%%%%%%%%%%%%%%%%%%%%%%%%%%%%%%%%%%
4 %%%                               %%%
5 %%%           rotor_e1.m          %%%
6 %%%                               %%%
7 %%%           Capt Greg Schultz, GA-95D %%%
8 %%%                               %%%
9 %%%           revision            %%%
10 %%%           -----            %%%
11 %%%           11.03.95.1530      %%%
12 %%%                               %%%
13 %%%%%%%%%%%%%%%%%%%%%%%%%%%%%%%%%%%%%%%%%%%%%%%%%%%%%%%%%%%%%%%%%%%%%%%%%%
14 %
15 % This file contains the equations of motion for a
16 % satellite with 3 embedded axisymmetric momentum
17 % wheels, without external perturbing torques.
18 %
19 % this includes direct trajectory for wheel spin-up
20 %
21 % calling program is rotor_m.m
22 %
23 global A;           % Allow usage of rotor direction unit vectors
24 global JI;         % Allow usage of pseudo inertia matrix inverse
25 global mu_o mu_f;  % Allow usage of initial and final rotor momenta
26 global direct;     % column vec. containing direct trajectory torques
27 %
28 x= [state(1); state(2); state(3)]; % vehicle momenta (in Fb)
29 mu=[state(4); state(5); state(6)]; % rotor momenta
30 q= [state(7); state(8); state(9); state(10)]; % Quaternions
31 %
32 % Now set up EOM for vehicle momenta (x),
33 % rotor momenta (mu), and quaternions (q)
34 %
35 xx=[ 0 -x(3) x(2);
36      x(3) 0 -x(1);
37      -x(2) x(1) 0];
38 %
39 w=JI*(x-A*mu);     % angular velocities
40 %

```

```

41 qx=[ 0    w(3) -w(2) w(1);
42     -w(3)  0    w(1) w(2);
43     w(2) -w(1)  0    w(3);
44     -w(1) -w(2) -w(3)  0];
45 %
46 xdot=xx*w;           % rotational Eq.
47 mudot=direct;       % wheel torque Eq.
48 qdot=.5*qx*q;
49 %
50 statedot=[xdot' mudot' qdot']; % return state

```

D.5 Unperturbed Sub-optimal Control Law Equations

```

1 function statedot=rotor_e2(t,state)
2 %
3 %%%%%%%%%%%%%%%%%%%%%%%%%%%%%%%%%%%%%%%%%%%%%%%%%%%%%%%%%%%%%%%%%%%%%%%%%%
4 %%%                               %%%
5 %%%           rotor_e2.m          %%%
6 %%%                               %%%
7 %%%           Capt Greg Schultz, GA-95D %%%
8 %%%                               %%%
9 %%%           revision            %%%
10 %%%           -----            %%%
11 %%%           11.02.95.1300      %%%
12 %%%                               %%%
13 %%%%%%%%%%%%%%%%%%%%%%%%%%%%%%%%%%%%%%%%%%%%%%%%%%%%%%%%%%%%%%%%%%%%%%%%%%
14 %
15 % This file contains the equations of motion for a
16 % satellite with 3 embedded axisymmetric momentum
17 % wheels, without external perturbing torques.
18 %
19 % this includes sub-optimal trajectory for wheel spin-up
20 %
21 % calling program is rotor_m.m
22 %
23 global A B JI Ic h_o Rgmu a1a1 a1a2 a2a2 small;
24 %
25 x= [state(1); state(2); state(3)]; % vehicle momenta (in Fb)
26 mu=[state(4); state(5); state(6)]; % rotor momenta
27 q= [state(7); state(8); state(9); state(10)]; % Quaternions
28 %

```

```

29 % Now set up EOM for vehicle momenta (x),
30 % rotor momenta (mu), and quaternions (q)
31 %
32 xx=[ 0 -x(3) x(2);
33      x(3) 0 -x(1);
34      -x(2) x(1) 0];
35 %
36 w=JI*(x-A*mu);          % angular velocities
37 %
38 qx=[ 0 w(3) -w(2) w(1);
39      -w(3) 0 w(1) w(2);
40      w(2) -w(1) 0 w(3);
41      -w(1) -w(2) -w(3) 0];
42 %
43 xdot=xx*w;              % rotational Eq (in Fb)
44 mudot=-small*Rgmu*B*Rgmu'*mu; % wheel torque Eq (in Fb)
45 qdot=.5*qx*q;          % attitude Eq (in Fb)
46 %
47 % output state vector after integration
48 %
49 statedot=[xdot' mudot' qdot'];

```

D.6 Perturbed Sub-optimal Control Law Equations

```

1 function statedot=rotor_e2_per(t,state)
2 %
3 %%%%%%%%%%%%%%%%%%%%%%%%%%%%%%%%%%%%%%%%%%%%%%%%%%%%%%%%%%%%%%%%%%%%%%%%%%
4 %%%                               %%%
5 %%%          rotor_e2_per.m        %%%
6 %%%                               %%%
7 %%%          Capt Greg Schultz, GA-95D %%%
8 %%%                               %%%
9 %%%          revision               %%%
10 %%%          -----              %%%
11 %%%          11.03.95.0830        %%%
12 %%%                               %%%
13 %%%%%%%%%%%%%%%%%%%%%%%%%%%%%%%%%%%%%%%%%%%%%%%%%%%%%%%%%%%%%%%%%%%%%%%%%%
14 %
15 % This file contains the equations of motion for a
16 % satellite with 3 embedded axisymmetric momentum
17 % wheels, WITH external perturbing torques.

```

```

18 %
19 % this includes sub-optimal wheel torque control
20 %
21 % calling program is rotor_m.m
22 %
23 global A B I_d JI Ic h_o rho_d rho_s
24 global Rgmu a1a1 a1a2 a2a2 small;
25 global rs ns As r_sm r_lg R_sm R_lg satmod pertflg;
26 %
27 GM=398601.2;           % Earth gravitational parameter = constant
28 Psun=4.644e-06;       % Solar pressure constant
29 wsun=1.99e-07;        % Sun vector angular velocity (rad/s) = constant
30 %
31 x= [state(1); state(2); state(3)];           % vehicle momenta (in Fb)
32 mu= [state(4); state(5); state(6)];         % rotor momenta
33 q= [state(7); state(8); state(9); state(10)]; % Quaternions
34 ths= [state(11)];                           % sun vector angle from e1
35 Ri= [state(12); state(13); state(14)];      % orb. pos. vector (in Fi)
36 Vi= [state(15); state(16); state(17)];      % orb. vel. vector (in Fi)
37 %
38 % Now set up EOM for vehicle momenta (x),
39 % rotor momenta (mu), and quaternions (q)
40 %
41 xx=[ 0 -x(3) x(2);
42      x(3) 0 -x(1);
43      -x(2) x(1) 0];
44 %
45 w=JI*(x-A*mu);                               % angular velocities
46 %
47 qx=[ 0 w(3) -w(2) w(1);
48      -w(3) 0 w(1) w(2);
49      w(2) -w(1) 0 w(3);
50      -w(1) -w(2) -w(3) 0];
51 %
52 Si=[sin(ths); cos(ths); 0];                 % sun vector (in Fi)
53 T=quat2rot(q);                             % rotation matrix y|b=T*R|i
54 Sb=T*Si;                                    % sun vector (in Fb)
55 b1i=[T(1,:)]';                             % spacecraft body axes (in Fi)
56 b2i=[T(2,:)]';
57 b3i=[T(3,:)]';
58 if pertflg==2                               % calc. gravity grad. torques (in Fb)
59   c3=[b1i'*Ri; b2i'*Ri; b3i'*Ri]/norm(Ri); % dir. cosines betw. Fb and Rorb
60   c3x=[ 0 -c3(3) c3(2);
61         c3(3) 0 -c3(1);
62         -c3(2) c3(1) 0];

```

```

63   Mg=c3x*I_d*c3*3*GM/(norm(Ri)^3);
64   else Mg=[0 0 0]';
65   end;
66   %
67   if pertflg>0                               % calc. solar pressure torques (in Fb)
68     for ii=1:10
69       rsx=[ 0      -rs(ii,3)  rs(ii,2);
70            rs(ii,3)  0      -rs(ii,1);
71            -rs(ii,2)  rs(ii,1)  0];
72       nsS=(ns(ii,:)*Sb);
73       if nsS>0, nsS=0; end;                    % don't count surfaces in shadow
74       Ms(ii,:)=(-nsS*rsx*((1-rho_s)*Sb+ ...
75                2*(rho_s+rho_d/3)*ns(ii,:)')*Psun*As(ii))';
76     end;
77     if satmod==2                               % account for cylinder surf. for Hub.
78       ns(1,:)=[-Si'*b1i -Si'*b2i 0]/norm([-Si'*b1i -Si'*b2i 0]);
79       ns(2,:)=ns(1,:);
80       rs(1,:)=R_sm+r_sm*ns(1,:);
81       rs(2,:)=R_lg+r_sm*ns(2,:);
82       rs1x=[ 0      -rs(1,3)  rs(1,2);
83             rs(1,3)  0      -rs(1,1);
84             -rs(1,2)  rs(1,1)  0];
85       rs2x=[ 0      -rs(2,3)  rs(2,2);
86             rs(2,3)  0      -rs(2,1);
87             -rs(2,2)  rs(2,1)  0];
88       Ms(1,:)=(-(ns(1,:)*Si)*rs1x*((1-rho_s)*Sb+ ...
89                2*(rho_s+rho_d/3)*ns(1,:)')*Psun*As(1))';
90       Ms(2,:)=(-(ns(2,:)*Si)*rs2x*((1-rho_s)*Sb+ ...
91                2*(rho_s+rho_d/3)*ns(2,:)')*Psun*As(2))';
92     end;
93     Ms=Ms(1,:)+Ms(2,:)+Ms(3,:)+Ms(4,:)+Ms(5,:)+Ms(6,:)+Ms(7,:)+Ms(8,:);
94     Ms=Ms';
95   else Ms=[0 0 0]';
96   end;
97   %
98   M=(Mg+Ms)*Ic/(h_o^2);                       % non-dimensional ext. torque (in Fb)
99   %
100  % Equations of motion
101  %
102  xdot=xx*w+M;                                  % rotational Eq (in Fb)
103  mudot=-small*Rgmu*B*Rgmu'*mu;              % wheel torque Eq (in Fb)
104  qdot=.5*qx*q;                                % attitude Eq (in Fb)
105  Rorbdot=Vi;                                  % orbital position Eq (in Fi)
106  Vorbdot=-GM*Ri/(norm(Ri)^3);               % orbital velocity Eq (in Fi)
107  thsdot=wsun;                                % sun vector Eq (in Fi)

```

```

108 %
109 % output state vector after integration
110 %
111 statedot=[xdot' mudot' qdot' thsdot' Rorbdot' Vorbdot'];

```

D.7 Wheel Momenta Ellipsoid Plotting Function (point by point)

```

1 function e=ell_plt0(a1,a2,a3,min1,max1,min3,max3,inc);
2 %
3 %%%%%%%%%%%%%%%%%%%%%%%%%%%%%%%%%%%%%%%%%%%%%%%%%%%%%%%%%%%%%%%%%%%%%%%%%%
4 %%%                               %%%
5 %%%               ell_plt0.m       %%%
6 %%%                               %%%
7 %%%       Capt Greg Schultz, GA-95D %%%
8 %%%                               %%%
9 %%%               revision         %%%
10 %%%       -----                 %%%
11 %%%       10.30.95.1200           %%%
12 %%%                               %%%
13 %%%%%%%%%%%%%%%%%%%%%%%%%%%%%%%%%%%%%%%%%%%%%%%%%%%%%%%%%%%%%%%%%%%%%%%%%%
14 %
15 %       e=ell_plt0(a1,a2,a3,min1,max1,min3,max3,inc)
16 %
17 % This routine plots the stationary platform wheel momenta
18 % solution "ellipsoid" in the wheel momenta "mu frame".
19 % a1,a2,a3 are 3 element column vectors representing
20 % wheel orientation w.r.t. body fixed frame.
21 %
22 % min1,max1,min3,max3 are min and max values for
23 % mu1 and mu3 respectively, to search over to calc mu2.
24 %
25 global Is_d h_o wsmax;
26 %
27 hsmax=(Is_d*wsmax)';           % vector of maximum allowable wheel momenta
28 A=[a1 a2 a3];
29 if rank(A)<3
30     ' Wheel unit vectors do not form a basis - ill-posed problem'
31     break;
32 end;
33 %
34 a1_a2=a1'*a2; a1_a3=a1'*a3; a2_a3=a2'*a3;           % these should all<1

```

```

35 a1_a1=a1'*a1; a2_a2=a2'*a2; a3_a3=a3'*a3;          % these should all=1
36 %
37 % Generate plot points for wheel momentum ellipsoid
38 %
39 na=0; nb=0;
40 for m3=min3:inc:max3
41     for m1=min1:inc:max1
42         na=na+1;
43         nb=nb+1;
44         m2=roots([a2_a2 2*m1*a1_a2+2*m3*a2_a3* ...
45                 a1_a1*m1^2+a3_a3*m3^2+2*m1*m3*a1_a3-1]);
46         %
47         if abs(imag(m2(1)))<1e-06          % only store real roots for plotting
48             m2(1)=real(m2(1));           % discard numerical imaginary "residue"
49             m2(2)=real(m2(2));
50             ma(na,:)= [m1 m2(1) m3];
51             mb(nb,:)= [m1 m2(2) m3];
52             hsa=(h_o*[m1 m2(1) m3]')';
53             hsb=(h_o*[m1 m2(2) m3]')';
54             if min(hsmax-abs(hsa))<0, na=na-1; end; % Don't plot if wheel momenta
55             if min(hsmax-abs(hsb))<0, nb=nb-1; end; % larger than max. allow.
56         else                               % don't store complex roots for plotting
57             na=na-1;
58             nb=nb-1;
59         end;
60     end;
61 end;
62 %
63 figure(1);                               % plot wheel momenta ellipsoid
64 axis([-1.5 1.5 -1.5 1.5 -1.5 1.5]);
65 view(120,30);
66 hold on;
67 plot3(ma(:,1),ma(:,2),ma(:,3),'r. ');
68 plot3(mb(:,1),mb(:,2),mb(:,3),'r. ');
69 lineft([0 0 0],[2 0 0],1,'y');text(2.1,0,0,'mu1');
70 lineft([0 0 0],[0 2 0],1,'y');text(0,2.1,0,'mu2');
71 lineft([0 0 0],[0 0 2],1,'y');text(0,0,2.1,'mu3');
72 lineft([0 0 0],[-2 0 0],1,'y');
73 lineft([0 0 0],[0 -2 0],1,'y');
74 lineft([0 0 0],[0 0 -2],1,'y');
75 title('wheel torque traj. w.r.t. stat. platform relative momenta surface');
76 xlabel('mu 1'); ylabel('mu 2'); zlabel('mu 3');
77 hold off;
78 %
79 figure(2);                               % now plot s/c total momentum sphere

```

```

80 axis([-1.5 1.5 -1.5 1.5 -1.5 1.5]);
81 view(120,30);
82 hold on;
83 sinc=deg2rad(5);
84 for v=-pi/2:sinc:pi/2
85     id=1;
86     for u=0:sinc:2*pi
87         rp=[cos(v)*cos(u); cos(v)*sin(u); sin(v)];
88         rx(id,:)=rp';
89         id=id+1;
90     end;
91     plot3(rx(:,1),rx(:,2),rx(:,3),'b:');
92 end;
93 lineft([0 0 0],[2 0 0],1,'y');text(2.1,0,0,'x1');
94 lineft([0 0 0],[0 2 0],1,'y');text(0,2.1,0,'x2');
95 lineft([0 0 0],[0 0 2],1,'y');text(0,0,2.1,'x3');
96 lineft([0 0 0],[-2 0 0],1,'y');
97 lineft([0 0 0],[0 -2 0],1,'y');
98 lineft([0 0 0],[0 0 -2],1,'y');
99 title('spacecraft momenta traj. during stationary platform maneuver');
100 xlabel('x1'); ylabel('x2'); zlabel('x3');
101 hold off;

```

D.8 Wheel Momenta Ellipsoid Plotting Function (parameterized)

```

1 function e=ell_plt1(a1,a2,a3,inc)
2 %
3 %%%%%%%%%%%%%%%%%%%%%%%%%%%%%%%%%%%%%%%%%%%%%%%%%%%%%%%%%%%%%%%%%%%%%%%%%%%
4 %%%                               %%%
5 %%%          ell_plt1.m           %%%
6 %%%                               %%%
7 %%%          Capt Greg Schultz, GA-95D %%%
8 %%%                               %%%
9 %%%          revision              %%%
10 %%%          -----              %%%
11 %%%          10.09.95.1130        %%%
12 %%%                               %%%
13 %%%%%%%%%%%%%%%%%%%%%%%%%%%%%%%%%%%%%%%%%%%%%%%%%%%%%%%%%%%%%%%%%%%%%%%%%%%
14 %
15 % e=ell_plt1(a1,a2,a3,inc);
16 %
17 % This function plots the ellipsoid which is the

```



```

18 % solution to the stationary platform condition
19 % (mu')(A')(A)(mu)=0, given the columns of A=[a1 a2 a3]
20 % The plotting resolution is determined by inc (in degrees)
21 %
22 % basically, this routine parameterizes the ellipsoid in the
23 % ellipsoid principal frame, then rotates the points back
24 % to the "mu" frame for plotting
25 %
26 % Also plots the related spacecraft momentum sphere
27 % arising from condition that x'x=1
28 %
29 inc=deg2rad(inc);          % convert inc to radians
30 A=[a1 a2 a3];
31 [R,abc]=eig(A'*A);        % calculate e-vectors, e-values
32 a=1/sqrt(abc(1,1));       % lengths of ellipsoid axes
33 b=1/sqrt(abc(2,2));       % are the eigenvalues of A'A
34 c=1/sqrt(abc(3,3));
35 %
36 figure(1);                % plot wheel momenta ellipsoid
37 axis([-1.5 1.5 -1.5 1.5 -1.5 1.5]);
38 view(120,30);
39 hold on;
40 %
41 for v=-pi/2:inc:pi/2      % parameterize with angles u,v
42     id=1;
43     for u=0:inc:2*pi
44         rp=[a*cos(v)*cos(u); b*cos(v)*sin(u); c*sin(v)];
45         rmu(id,:)=(R*rp)';
46         rx(id,:)=(A*rmu(id,:))';
47         id=id+1;
48     end;
49     plot3(rmu(:,1),rmu(:,2),rmu(:,3),'r:'); % plot ellipses
50 end;
51 %
52 lineft([0 0 0],[2 0 0],1,'y');text(2.1,0,0,'mu1');
53 lineft([0 0 0],[0 2 0],1,'y');text(0,2.1,0,'mu2');
54 lineft([0 0 0],[0 0 2],1,'y');text(0,0,2.1,'mu3');
55 lineft([0 0 0],[-2 0 0],1,'y');
56 lineft([0 0 0],[0 -2 0],1,'y');
57 lineft([0 0 0],[0 0 -2],1,'y');
58 title('rotor torque traj. w.r.t. stat. platform relative momenta surface');
59 xlabel('mu 1'); ylabel('mu 2'); zlabel('mu 3');
60 hold off;
61 %
62 figure(2);                % now plot s/c total momentum sphere

```

```

63 axis([-1.5 1.5 -1.5 1.5 -1.5 1.5]);
64 view(120,30);
65 hold on;
66 for v=-pi/2:inc:pi/2
67     id=1;
68     for u=0:inc:2*pi
69         rp=[cos(v)*cos(u); cos(v)*sin(u); sin(v)];
70         rx(id,:)=rp';
71         id=id+1;
72     end;
73     plot3(rx(:,1),rx(:,2),rx(:,3),'b:');
74 end;
75 lineft([0 0 0],[2 0 0],1,'y');text(2.1,0,0,'x1');
76 lineft([0 0 0],[0 2 0],1,'y');text(0,2.1,0,'x2');
77 lineft([0 0 0],[0 0 2],1,'y');text(0,0,2.1,'x3');
78 lineft([0 0 0],[-2 0 0],1,'y');
79 lineft([0 0 0],[0 -2 0],1,'y');
80 lineft([0 0 0],[0 0 -2],1,'y');
81 title('spacecraft momenta traj. during stat. platform maneuver');
82 xlabel('x1'); ylabel('x2'); zlabel('x3');
83 hold off;

```

D.9 "1" Axis Rotation Matrix Function

```

1 function R1=rot1(a)
2 %
3 % R1=rot1(a)
4 %
5 % Frame ijk is rotated by angle a (radians) about
6 % axis i in a positive sense (right hand rule) relative
7 % to fixed frame IJK.
8 %
9 % R1' is the rotation matrix that transforms a vector x
10 % expressed in frame ijk to a vector X expressed in frame IJK.
11 %
12 % e.g. if a=pi/4 and x=[1 1 0]', then X = R1'*x = [1 .7071 .7071]'
13 %
14 R1=[ 1      0      0;
15      0      cos(a) sin(a);
16      0     -sin(a) cos(a)];

```

D.10 "3" Axis Rotation Matrix Function

```
1 function R3=rot3(a)
2 %
3 % R3=rot3(a)
4 %
5 % Frame ijk is rotated by angle a (radians) about
6 % axis k in a positive sense (right hand rule) relative
7 % to fixed frame IJK.
8 %
9 % R3' is the rotation matrix that transforms a vector x expressed
10 % in frame ijk to a vector X expressed in frame IJK.
11 %
12 % e.g. if a=pi/4 and x=[1 0 1]', then X = R3'*x = [.7071 .7071 1]'
13 %
14 R3=[ cos(a) sin(a) 0;
15      -sin(a) cos(a) 0;
16      0 0 1];
```

D.11 Quaternion to Rotation Matrix Conversion Function

```
1 function Rq=quat2rot(q)
2 %
3 % Rq=quat2rot(q)
4 %
5 % This function produces a transformation matrix Rq
6 % based on quaternions specified by the 4 element row vector
7 % q. This rotation matrix can be used to transform a
8 % vector from a rotated frame to a non-rotated frame
9 %
10 Rq(1,1)=q(1)^2-q(2)^2-q(3)^2+q(4)^2;
11 Rq(1,2)=2*(q(1)*q(2)+q(3)*q(4));
12 Rq(1,3)=2*(q(1)*q(3)-q(2)*q(4));
13 Rq(2,1)=2*(q(1)*q(2)-q(3)*q(4));
14 Rq(2,2)=-q(1)^2+q(2)^2-q(3)^2+q(4)^2;
15 Rq(2,3)=2*(q(1)*q(4)+q(2)*q(3));
16 Rq(3,1)=2*(q(1)*q(3)+q(2)*q(4));
17 Rq(3,2)=2*(-q(1)*q(4)+q(2)*q(3));
18 Rq(3,3)=-q(1)^2-q(2)^2+q(3)^2+q(4)^2;
```

D.12 Vector Cross Product Function

```
1 function c = cross(a,b)
2 % CROSS Cross product of two vectors c = a x b
3 % a and b must have 3 components
4 %
5 % c = cross(a,b)
6 c=[a(2)*b(3)-a(3)*b(2) a(3)*b(1)-a(1)*b(3) a(1)*b(2)-a(2)*b(1)];
```

D.13 Degrees to Radians Conversion Function

```
1 function x = deg2rad(a)
2 %DEG2RAD converts angle from degrees to radians
3 %      syntax x = deg2rad(a)
4 %
5 %
6 x = (a/360)*2*pi;
```

D.14 Radians to Degrees Conversion Function

```
1 function x = rad2deg(a)
2 %RAD2DEG converts angle from radians to degrees
3 % Syntax x = rad2deg(a)
4 %
5 %
6 x = (a/pi)*180;
```

D.15 3-D Line Plotting Function

```
1 function H=lineft(r1,r2,thickness,color)
2 %
3 % H = lineft(r1,r2,thickness,color)
4 %
5 % Draws a line of thickness from r1 to r2
6 % in cartesian coordinates.
7 % color is a 1 or 2 char string.
8 %
9 if nargin==2, thickness=1; end;
10     X=[r1(1) r2(1)]';
11     Y=[r1(2) r2(2)]';
12     Z=[r1(3) r2(3)]';
13     H=line(X,Y,Z);
14 set(H,'LineWidth',thickness,'Color',color);
```

Bibliography

1. Agrawal, Brij N. *Design of Geosynchronous Spacecraft*. New York: Prentice-Hall, Inc., 1986.
2. Andersen, G.C., D.A. Quinn, G.A. Beals, J.D. Nelson, and G.S. Nurre. An Overview of the Hubble Space Telescope Pointing Control System Design and Operation. AIAA paper 92-4616. August 1992.
3. Bate, Roger R., Donald B. Mueller, and Jerry E. White. *Fundamentals of Astrodynamics*. New York: Dover, 1971.
4. Beyer, William H. (Editor) *CRC Standard Mathematical Tables and Formulae*. 29th Edition. Boca Raton, Florida: CRC Press, 1991.
5. Chobotov, Vladimir A. *Spacecraft Attitude Dynamics and Control*. Malibar, Florida: Krieger Publishing Company, 1991.
6. Geiger, Cindy. Mechanical Reaction Wheel Assembly Tachometer Processing Logic for the GPS IIR Telemetry Wavetrain Simulation. Interoffice Memorandum ACS95-024. Martin Marietta Corporation, Astro Space Division. 4 May 1995.
7. Gido, J. Reaction Wheel Assembly Model for GPS IIR Telemetry Wavetrain Simulator. Interoffice Memorandum ACS95-074. Martin Marietta Corporation, Astro Space Division. 30 June 1995.
8. Hall, Christopher D. Spinup Dynamics of Gyrostats. *Journal of Guidance, Control, and Dynamics*. Vol. 18, No. 5, pp. 1177-1183, 1995.
9. Hall, Christopher D. Spinup Dynamics of Gyrostats with Two Rotors. Presented at the AAS/AIAA Spaceflight Mechanics Meeting. AAS paper 95-205, 13 February 1995.
10. Hall, Christopher D. and R.H. Rand. Spinup Dynamics of Axial Dual-spin Spacecraft. *Journal of Guidance, Control, and Dynamics*. Vol. 17, No. 1, pp. 30-37, 1994.
11. Hughes, Peter C. *Spacecraft Attitude Dynamics*. New York: John Wiley and Sons, 1986.
12. Junkins, John L. and James D. Turner. *Optimal Spacecraft Rotational Maneuvers*. Amsterdam, The Netherlands: Elsevier, 1986.
13. Kaplan, Marshall H. *Modern Spacecraft Dynamics and Control*. New York: John Wiley and Sons, 1976.
14. Kinney, David L. *An Approximate Solution for the Linearized Spinup Dynamics of a Dual-spin Spacecraft*. MS Thesis, AFIT/GA/ENY/92D-11. School of Engineering, Air Force Institute of Technology (AU), Wright-Patterson AFB, OH, December 1992.
15. Kowall, Stewart J. *An Approximate Solution for the Spinup Dynamics of Near Axisymmetric Axial Gyrostats Using the Method of Multiple Scales*. MS Thesis, AFIT/GA/ENY/93D-5. School of Engineering, Air Force Institute of Technology (AU), Wright-Patterson AFB, OH, December 1993.
16. Likins, Peter W. *Elements of Engineering Mechanics*. New York: McGraw-Hill Inc., 1973.

17. Navstar Global Positioning System (GPS) Replenishment Satellites (Block IIR) Phase II Mass Properties Report - Subnumber 1.0. Martin Marietta Corporation, Astro Space Division, 9 March 1995.
18. Navstar Global Positioning System (GPS) Block IIA orbital ephemeris data. Air Force Satellite Control Network (AFSCN) Command And Control Segment (CCS) screen capture (UNCLASSIFIED), August 1995.
19. Navstar Global Positioning System (GPS) Replenishment Satellites (Block IIR) Orbital Operations Handbook, Volume I (UNCLASSIFIED). Martin Marietta Corporation, Astro Space Division. 16 December 1994.
20. Sharkey, J.P., G.S. Nurre, G.A. Beals, and J.D. Nelson. A Chronology of the On-orbit Pointing Control System Changes on the Hubble Space Telescope and Associated Pointing Improvements. AIAA paper 92-4618-CP. 1992.
21. Strang, Gilbert. *Linear Algebra and Its Applications*. Second Edition. New York: Academic Press, 1980.
22. Tsui, Raymond. *Resonance Capture in Unbalanced Dual-spin Spacecraft*. MS Thesis, AFIT/GA/ENY/94M-3. School of Engineering, Air Force Institute of Technology (AU), Wright-Patterson AFB, OH, March 1994.

Vita

Greg Schultz [REDACTED] Don and Lorilla Schultz. His father, now happily "retired" in southern California, was a manager in the Federal Aviation Administration, and as is the case with many federal jobs, the family moved several times throughout the Midwest and Northeast during Greg's childhood.

His parents' love of flying and aircraft was passed down to Greg, who, growing up in the exciting era of the space shuttle and the Voyager interplanetary probes, developed a fascination with spacecraft and space exploration. Greg also had a keen interest in science and math since early childhood, so when it came time to choose a field of study for college, he chose aerospace engineering.

Greg attended the Pennsylvania State University (go Lions!!) on an Air Force ROTC scholarship. He focused his Aerospace Engineering studies on space systems by taking electives in spacecraft propulsion, orbital dynamics, spacecraft design, and feedback control systems theory. While in school, he still pursued his first (and lifelong) infatuation - ice hockey, and was an active member of Triangle fraternity. Through a series of fateful coincidences, Greg also met his beautiful, caring, and supportive wife to be, Ruthe. After four years of classes and fun, he graduated in August 1989. He was also blessed with his first son, [REDACTED], in the same year.

While waiting for his first assignment, Greg worked as a temporary GS-7 engineer at Rome Laboratories, Griffiss AFB, NY, where he developed a thermal model of a space-based phased array radar in orbit. In November 1989 he and his family moved to Los Angeles, where he began work as an Astronautical Engineer in the Satellite and Launch Control Systems program office at HQ Space and Missile Systems Center (SMC). The climate and job in L.A. proved to be excellent. Greg managed development of state of the art satellite and ground control segment simulation systems and network resource scheduling systems, both high profile (and somewhat controversial) developments which earned him the trust and accolades of his superiors. While in L.A., Greg completed his M.B.A at Chapman University and was also blessed with two more sons, [REDACTED] (good work, Ruthe!).

In 1994, After four and a half years, it was time to move on, so Greg applied and was accepted by the AFIT School of Engineering to pursue an M.S. in Astronautical Engineering.

After Graduation, the Schultz family packed up and moved to Hanscom AFB, MA, where Greg was assigned to Phillips Laboratory.

Permanent address: [REDACTED]

December 1995

Master's Thesis

SUB-OPTIMAL CONTROL OF RIGID SPACECRAFT
REORIENTATION USING THREE MOMENTUM WHEELS

Gregory W. Schultz, Capt, USAF

Air Force Institute of Technology
2750 P Street
WPAFB OH 45433-6583

AFIT/GA/ENY/95D-04

Gregory Barentine, Major, USAF
HQ SMC/CWD
Los Angeles AFB, CA 90009-2960

Distribution Unlimited

This study investigated the applicability and limitations of a sub-optimal control law for stationary platform maneuvers of rigid three-axis stabilized spacecraft using three momentum wheels. Computer simulations using this control law were conducted for existing operational spacecraft (GPS Block IIR and Hubble Space Telescope) in both a torque free environment and an environment with gravity gradient and solar pressure torques, to characterize the utility of such control laws for vehicles using momentum wheels for primary attitude control vs. those using them only to augment the primary system. Results indicate that while the control law is useful in real applications, there is a significant trade-off between maneuvering time and final state errors.

Astronautics; Spacecraft; Dynamics; Attitude Control; Momentum Wheels

158

Unclassified

Unclassified

Unclassified

UL